

INVESTIGATION OF SHOCK FRONT TOPOGRAPHY
IN SHOCK TUBES

Thesis by
Robert Marcus Bowman

In Partial Fulfillment of the Requirements

For the Degree of
Doctor of Philosophy

California Institute of Technology
Pasadena, California

1966

(Submitted May 6, 1966)

ACKNOWLEDGEMENTS

To Dr. H. W. Liepmann I am deeply indebted for his inspiration, his patient assistance, and his wise counsel. It gives me great pleasure to acknowledge his part in this work.

To Drs. Roshko, Coles, and Sturtevant I am indebted for their having been instrumental in bringing into being the marvelous GALCIT 17" shock tube, the use of which I was privileged to enjoy.

I would also like to thank Capt. D. S. Johnson, who first aroused my interest in shock tube research and taught me to operate the GALCIT tube. A special thanks must also go to the technical staff of the GALCIT fluid dynamics laboratory for their assistance with the experimental apparatus.

The figures were prepared by the Graphic Arts department of Cal Tech and the typescript was accomplished by Mrs. John E. Hoffer of Dayton, Ohio. Their patient cooperation and excellent accomplishments are sincerely appreciated.

I wish to express my appreciation to the United States Air Force for granting me the opportunity to pursue these studies and to NASA for their sponsorship of the experiments through NASA Grant NsG-40-60.

Finally I want to thank my wife Margaret for her interest and encouragement, but most of all for her love and for the six children to whom I dedicate my work.

ABSTRACT

An experimental investigation of the shape of shock waves in a circular shock tube is conducted. It is found that there are three distinct regimes governed, in a given tube, by the initial pressure in the test section.

At very low pressures, where the shock thickness is greater than about half the tube radius, the axial extent (deviation from a plane) of the shock is roughly constant and dominated by the viscous interaction between the "shock", the boundary layer, and the driving piston of gas. This range of pressures is called the viscosity-dominated regime.

At intermediate pressures, the shape of the shock is very nearly that predicted by the theory of de Boer, the shock curvature being produced by the boundary layer and the axial extent being roughly inversely proportional to the square root of the initial pressure. This is the boundary layer regime. de Boer's work is extended and the shock shapes for both the two-dimensional and axisymmetric cases are computed and plotted.

At high pressures, the shape of the shock is complex and varies periodically down the tube. This shape is determined by transverse waves produced at the diaphragm (or other upstream disturbance) and reflecting back and forth across the tube, decaying with the square root of the distance down the tube. In this transverse wave regime,

the axial extent of the shock is essentially independent of initial pressure and is much greater than had been expected.

The square root decay of the transverse wave disturbances is in contrast to the $3/2$ power decay predicted by Freeman and apparently verified by Lapworth. The experimental data of Lapworth is re-plotted and it is shown that if this data is analyzed in a slightly different manner it appears to exhibit square root decay.

It is shown that the shock perturbations which exist in the transverse wave regime are absent at lower pressures. The transition region where these disturbances suddenly disappear seems to correspond approximately to the initial pressure at which the boundary layer (appropriately defined) at the disturbance fills the tube.

A rule of thumb is developed from which it should be possible to predict the transition initial pressure (which separates the transverse wave and boundary layer regimes) in any given shock tube. This pressure occurs when the quantity $L/p_1 R^2$ is of order one, the tube dimensions being in millimeters and the initial pressure in millimeters of mercury. This rule of thumb is used to analyze the results of several shock tube experiments published by other researchers.

Using this rule of thumb as an important constraint, a low-pressure shock tube design chart is developed, from which, given the type of experiments contemplated and the nature of the instrumentation available, the proper shock tube dimensions and operating pressures may be determined.

Finally, avenues of future research are suggested, wherein it may be possible to design a new type of "hi-fi" shock tube, capable of producing more nearly plane shock fronts for use in shock structure and relaxation time studies, especially where methods such as integrated schlieren, optical reflectivity, or electron beam scattering are to be used.

CONTENTS

	PAGE
ACKNOWLEDGEMENTS	ii
ABSTRACT	iii
LIST OF FIGURES	x
LIST OF SYMBOLS	xiii
CHAPTER	
I. INTRODUCTION	1
I.1 Historical Development of Shock Shape Research	1
I.1.1 The Plane, One-Dimensional Shock . . .	1
I.1.2 Lin & Fyfe 1961	2
I.1.3 Duff & Young 1961	4
I.1.4 Hartunian 1961	6
I.1.5 Johnson 1962	7
I.1.6 Daen & de Boer 1962	9
I.1.7 de Boer 1963	11
I.1.8 Liepmann & Bowman 1964	13
I.2 Possible Sources of Non-Planarity	14
I.3 Shock Shape Regimes	15
I.3.1 The Viscosity-Dominated Regime	15
I.3.2 The Boundary Layer Regime	17
I.3.3 The Transverse Wave Regime	18
I.4 Application of Shock Shape Knowledge	20
I.5 General Experimental Procedure	22
I.6 Preliminary Comment on Curve-Tracing Technique .	24
II. BOUNDARY LAYER REGIME: THEORY	26
II.1 Formulation of the Problem	26
II.2 Results of the Potential Solution	29
II.3 Determination of A^* , Final Results	31

CHAPTER	PAGE
III. BOUNDARY LAYER REGIME: EXPERIMENTS AND RESULTS	36
III.1 Shock Shapes, Comparison With Theory	36
III.2 Variation of "Axial Extent" With R_e	40
III.3 Effect of Mach Number	43
III.4 Miscellaneous Geometrical Effects	46
IV. VISCOSITY-DOMINATED REGIME	50
V. TRANSVERSE WAVE REGIME: EXPLORATORY EXPERIMENTS	57
V.1 Departure from Boundary Layer Theory	57
V.2 Partial Diaphragm Experiments	63
V.3 Effect of Blade Shape	69
V.4 Effect of Driver/Test Section Area Ratio	72
V.5 Superposition of Viscous and Non-Viscous Effects	76
V.6 Effect of Mach Number: Phase Shift	78
VI. TRANSVERSE WAVE REGIME: "ROOFTOP" EXPERIMENTS	83
VI.1 The Riddle of Pressure-Dependent Disturbances	83
VI.2 Possible Causes of the Pressure Dependence	85
VI.3 The Axisymmetric Rooftop Disturbance Experiment	88
VI.4 Results of the "Rooftop" Experiment	92
VI.5 Discussion of "Rooftop" Results	102
VI.6 Re-Evaluation of Lapworth's Experiment	110

CHAPTER	PAGE
VII. TRANSITION BETWEEN THE TRANSVERSE WAVE AND BOUNDARY LAYER REGIMES	118
VII.1 The Rooftop Experiment at $p_1 = 100\mu$ Hg	118
VII.2 Physical Explanation of the Transition Region	120
VII.3 Rule of Thumb Transition Condition	121
VIII. IMPLICATIONS FOR DATA INTERPRETATION	124
VIII.1 General Considerations	124
VIII.2 Example Applications	126
VIII.2.1 Duff & Young	126
VIII.2.2 Lin & Fyfe	127
VIII.2.3 Linzer & Hornig	128
VIII.2.4 Wray	129
VIII.2.5 Daen & de Boer	130
VIII.2.6 de Boer	131
IX. IMPLICATIONS FOR SHOCK TUBE DESIGN	132
IX.1 The Conventional Shock Tube	132
IX.2 The "Hi-Fi" Shock Tube	139
REFERENCES	144
APPENDIX	
A. SHOCK TUBE DESCRIPTION	147
A.1 Description of the GALCIT 17" Shock Tube	147
B. FILM GAGE DESCRIPTION	148
B.1 Film Gage Response Theory	148
B.2 Non-ideal Gage Performance	152
B.3 Prevention of Gage Burnout	155
B.4 The Multiple-film Gage	156

APPENDIX	PAGE
C. RE-FORMULATION AND EXTENSION OF DE BOER'S TWO-DIMENSIONAL SHOCK SHAPE THEORY	158
C.1 Formulation of the Problem	158
C.2 Solution of the Problem	162
C.3 Evaluation of the Shape	166
D. RE-FORMULATION AND EXTENSION OF DE BOER'S AXISYMMETRIC SHOCK SHAPE THEORY	168
D.1 Formulation of the Problem	168
D.2 Solution of the Problem	172
D.3 Evaluation of the Shape	175
D.4 Central Radius of Curvature	177
D.5 Numerical Evaluation of $P \equiv \int_0^{\infty} \frac{\sqrt{\tau} d\tau}{I_1(\tau)}$	179
E. NUMERICAL EVALUATION OF $Q \equiv \int_0^{\infty} \frac{I_0(\tau\eta) - 1}{I_1(\tau) \tau^{3/2}} d\tau$	181
E.1 Expansion for Small τ	181
E.2 Computation of Q_2	183
E.3 Expansion for Large $\tau\eta$	184
F. DISCUSSION OF ACCURACY	191
F.1 General Considerations	191
F.2 Discussion of Signal Errors	192
F.3 Discussion of Post-Signal Errors	193
F.4 Sample Adjusted Shock Shape Determination	194

LIST OF FIGURES

FIGURE		PAGE
I.1	Typical Shock Shapes (Schematic)	19
I.2	General Experimental Procedure	23
II.1	Coordinate System	27
II.2	Implication of Small-Angle Approximation	27
III.1	Normalized Shock Shape in Boundary Layer Regime (Argon)	38
III.2	True Scale Experimental Shock Shape at $p_1 = 10\mu$ Hg (Argon)	39
III.3	Definition of $\Delta x(.8)$	41
III.4	Variation of Shock Extent with Initial Pressure in Boundary Layer Regime	42
III.5	Effect of Mach Number on Shock Shape in Boundary Layer Regime ($p_1 = 10\mu$ Hg, Argon)	45
III.6	Miscellaneous Geometric Effects on Shock Shape in Boundary Layer Regime ($p_1 = 100\mu$ Hg, Argon)	49
IV.1	Normalized Shock Shapes (Viscosity-Dominated Regime)	53
IV.2	Variation of Shock Extent with Initial Pressure in Viscosity-Dominated Regime	54
IV.3	Shock Profile at Extremely Low Pressure ($p_1 = .5\mu$ Hg)	55
IV.4	Typical Heat Transfer Thin-Film Gage Responses at Extremely Low Pressure ($p_1 = .5\mu$ Hg, $M = 11.2$)	56
V.1	Variation of Shock Extent with Initial Pressure in Transverse Wave Regime	59
V.2	"Tilt" or Slope of Shock at Center of Tube vs. Initial Pressure	60

LIST OF FIGURES (Cont'd)

FIGURE		PAGE
V.3	Typical Shock Shape at $p_1 = 1$ mm Hg	61
V.4	Typical Shock Shape at $p_1 = 3$ mm Hg	62
V.5	Partial Diaphragm Experiment: Blocking Technique	65
V.6	Partial Diaphragm Experiment: Ruptured Diaphragm	66
V.7	Effect of Partial Diaphragm at $p_1 = 3$ mm Hg	67
V.8	Effect of Partial Diaphragm at $p_1 = 10$ mm Hg	68
V.9	Effect of Knife Blade Shape at $p_1 = 1$ mm Hg	71
V.10	Effect of Driver/Test Section Area Ratio at $p_1 = 1$ mm Hg	75
V.11	Effect of Mach Number at $p_1 = 1$ mm Hg	81
V.12	Adjusted Shock Shapes vs. M at $p_1 = 1$ mm Hg	82
VI.1	Cutaway View of Axisymmetric Rooftop Disturbance	90
VI.2	Experiment Schematic	91
VI.3	True Scale Shock Shapes Immediately Downstream of Axisymmetric Rooftop Disturbance	97
VI.4	Transverse Wave Geometry for Derivation of Equations 6.2 - 6.4 ($M_2' > M_W \geq 1$)	98
VI.5	Transverse Wave Geometry for Axisymmetric Rooftop Experiment and All Cases of Large Wedge Angle ($M_W = M_2' > 1$)	99
VI.6	Transverse Wave Geometry After Reflection ($M_W = M_2' > 1$)	100
VI.7	Shock Perturbation @ $r/R = .896$ vs. Distance Travelled Due to Axisymmetric Rooftop Disturbance ($p_1 = 3$ mm Hg)	101
VI.8	Shock Shapes (Actual vs. Freeman's Theory)	108

LIST OF FIGURES (Cont'd)

FIGURE		PAGE
VI.9	Approximate Graph of the Function $W(\vartheta)$	109
VI.10	Re-Plot of Lapworth's Data: Total Perturbation vs. Distance Travelled	116
VI.11	Transverse Wave Geometry for Subsonic Disturbance ($M_w \geq 1 > M_2'$)	117
VII.1	Shock Perturbation at $r/R = .896$ vs. Distance Travelled Due to Axisymmetric Rooftop Disturbance ($p_1 = 100\mu$ Hg)	119
VIII.1	Data Interpretation Summary	131A
IX.1	Low Density Shock Tube Design Chart	137
IX.2	Summary of Shock Deviation from Planarity for GALCIT 17" Shock Tube	138
IX.3	Transition Section for a "Hi-Fi" Shock Tube	143
B.1	Basic Film Gage Circuit	150
B.2	Theoretical End Wall Film Gage Response (for Air at $T_1 = 300^\circ$)	151
B.3	Effective vs. Applied Current	154
B.4	Multiple-Film Gages	157
C.1	Wavy Wall Geometry (Two-Dimensional)	161
C.2	Theoretical Shock Shape: Two-Dimensional Case (Two Parallel Walls)	167
D.1	Axisymmetric Geometry	171
D.2	Theoretical Shock Shape: Axisymmetric Case	176
E.1	General Equation for Q_{3a}	189
E.2	Results of Numerical Evaluation of Q	190
F.1	Data from Run 1401	195
F.2	True Scale Adjusted Shock Shape, Run 1401	196

LIST OF SYMBOLS

Latin Alphabet

A^*	boundary layer thickness amplitude function
A, A', A''	arbitrary constants
A_λ, A_k, A_p	Fourier coefficients
a	speed of sound
a	empirical constant locating origin of decay
B, B', B''	arbitrary constants
C	defined in equation 3.11c
C'	arbitrary constant
D	diameter
D'	arbitrary constant
d	differential
E	voltage drop across film gage
E_0	power supply voltage
E_i	an exponential integral function (see Ref. 32)
e	arbitrary constant (less than one)
F	radial function as defined in equation D.3
f	function expressing shape of wall
ζ	as defined below equation C.25
G	perturbation amplitude function defined by equations 6.5 and 6.6
G	axial function as defined in equation D.3
g	as defined below equation C.25

LIST OF SYMBOLS (Cont'd)

Latin Alphabet

h	channel half-height as defined in figure C.1
h	enthalpy
I	current
I_{eff}	effective current
I_0	modified Bessel function of first kind of order 0
I_1	modified Bessel function of first kind of order 1
I_2	modified Bessel function of first kind of order 2
j	limited range index
K_1	modified Bessel function of second kind of order 1
$k = \frac{2\pi}{\lambda_m}$	adjusted wall frequency (becomes dummy of integration)
L	tube length from diaphragm to test station
ℓ_m	testing length (maximum separation between shock and contact surface)
M	Mach number
$m = (1 - M_2^2)^{1/2}$	except that in chapter VI, m is a dimensionless transverse wave frequency
ma	milliamps (current)
mm	millimeters (length)
$mm \text{ Hg}$	millimeters of mercury (pressure)
n	index of summation
n	decay constant
P, P_1, P_2, P_3	definite integrals defined in equation D.32

LIST OF SYMBOLS (Cont'd)

Latin Alphabet

p	pressure
psia	pounds per square inch absolute (pressure)
p	wall frequency (becomes dummy of integration)
Q, Q_1, Q_2, Q_3	definite integrals defined in equation E.1
Q_{3a}, Q_{3b}	definite integrals defined by equations E.11 and E.12
R	radius of tube (film gage resistance in appendix B)
Re	Reynolds number
R_0	radius of curvature at $r = 0$
R_0	ballast resistance
R_0^*	optimum ballast resistance (ideal theory)
R_n	ratio of successive terms in a series, as defined in equation E.26
r	radial position from center
S	ratio of negative to positive peak heights in function $W(\vartheta)$
S'	same as S , but for function $W'(\vartheta)$
$\delta = x/m$	adjusted axial distance variable
T	temperature
T_n	the "n"th term of a series
t	time
τ	adjusted wall frequency (becomes dummy of integration)
U	local flow axial velocity component relative to shock front

LIST OF SYMBOLS (Cont'd)

Latin Alphabet

u	(without subscript) argument of the incomplete gamma function, defined by equation E.19
V	volts (voltage)
v	local flow vertical velocity component
W	empirical periodic function explained in section VI.5 and sketched in figure VI.9 (applies to shock perturbation in axisymmetric case)
W'	empirical function similar to W, but for Lapworth's two-dimensional geometry
x	axial distance from origin (measured toward diaphragm)
x _{sh}	shock shape function (axial shock position measured from position of center of shock)
$\Delta x(.8)$	shock deviation from planarity as defined in figure III.4
x	general variable used in identities
Y	defined in figure VI.4
y	distance from lower wall in two-dimensional case
z	axial distance down tube from trailing edge of disturbance

LIST OF SYMBOLS (Cont'd)

Greek Alphabet

α	defined in equation 3.11a
β	angle made by shock-shock and tube wall
Γ	gamma function
$\Gamma(\nu, \mu)$	the general incomplete gamma function
γ	ratio of specific heats
Δe	signal voltage
$\Delta x(.8)$	shock deviation from planarity as defined in figure III.4
∂	shock thickness
δ	boundary layer thickness as defined in equation 3.11d
δ'	boundary layer thickness as defined by equation 7.1
δ^*	boundary layer displacement thickness
ϵ	defined in equation 3.11b
ζ	axial distance down tube from origin of decay
$\eta \equiv$	r/R (axisymmetric case) $1 - y/h$ (two-dimensional case)
$\bar{\eta} \equiv y/h$	
θ	axial extent
ϑ	transverse wave and shock shape periodicity angle defined in figure VI.8
λ	wavelength of wavy wall
μ	(without subscript) argument of the incomplete gamma function, defined by equation E.19
μ	(with subscript) viscosity

LIST OF SYMBOLS (Cont'd)

Greek Alphabet

μ Hg	microns of mercury (pressure)
μ_m	Mach angle
μsec	microsecond = 10^{-6} sec
ν	(without subscript) argument of the incomplete gamma function, defined by equation E.19
ν	(with subscript) kinematic viscosity
ξ	shock perturbation amplitude
π	3.14159...
ρ	density
\sum	summation
σ	local shock slope
τ	defined in figure VI.4
ϕ	velocity potential
ψ	defined in figure VI.4
ψ	transverse wave and shock shape phase angle, defined by equations 6.5 and 6.6
Ω	ohms (resistance)
ω	temperature coefficient of viscosity

LIST OF SYMBOLS (Cont'd)

Subscripts

flow conditions:

- | | |
|----------|--------------------------------------|
| 1 | ahead of shock |
| 2 | behind shock |
| w | at wall behind shock |
| 4 | driver section |
| ∞ | free stream (outside boundary layer) |

other:

- | | |
|---|---|
| t | transmitted (downstream of disturbance) |
| w | referring to transverse wave |
| x | } denotes partial derivative with respect
to the particular independent variable |
| y | |
| s | |
| r | |

Miscellaneous

- | | |
|---|---------------|
| " | inch (length) |
|---|---------------|

I. INTRODUCTION

I.1 Historical Development of Shock Shape Research

I.1.1 The Plane, One-Dimensional Shock

The ideal shock tube is completely one-dimensional, the plane shock wave being formed instantaneously by an ideal diaphragm removal and propagating down the tube at constant speed ahead of a sharp, planar contact discontinuity. In the early years of shock tube technology it was considered obvious that the shock waves were indeed plane and one-dimensional, any effect of the finite opening time of the diaphragm being felt at most a few diameters downstream, and viscous effects at the walls being completely ignored. Indeed the early experiments of Bleakney, Weimer, & Fletcher in 1949 (Ref. 1) seemed to confirm this view. They found that shock waves deviated from a plane by less than 1/10 of a degree. This result was often quoted without any mention of the particular experimental conditions involved. The measurements were made with a shadowgraph technique at high initial pressures in a fairly rough rectangular tube. That the results might not be valid for all tubes under all conditions was not immediately suspected.

I.1.2 Lin & Fyfe 1961 (Ref. 2)

While early shock tube researchers had been primarily interested in producing a slug of high-speed, high-temperature gas between the shock and contact surface for aerodynamic testing, toward the end of the 1950's interest began to shift to the shock front itself. This shift in emphasis was caused by increased interest in the problems of high speed, high altitude flight and the study of chemical kinetics, including reaction rates and relaxation times. Since the characteristic times involved are proportional to the mean free path, it became necessary to work with highly rarefied gases in order to obtain times sufficiently large in comparison with the response time of available instrumentation. It has already been noted that the length of the test gas slug was less than ideal and that this effect increased greatly at low pressures due to increased leakage of the test gas past the contact surface through the boundary layer. Thus it was recognized that in order to maintain a definite separation between the shock front and the contact region it would be necessary to use shock tubes of much larger diameter if initial pressures were to be less than about 1 mm Hg. This reasoning led to the construction of several large diameter, low pressure shock tubes. In one of these, the Avco 24" diameter shock tube, Lin & Fyfe attempted to measure the translational/rotational shock thickness in air at Mach numbers between 12 and 22 and at initial pressures ranging from .02 to .5 mm Hg. They found that the apparent shock thicknesses were much greater than theoretically

expected, that there was little correlation with Mach number, and that the apparent thicknesses were inversely proportional (approximately) to the square root of the initial pressure. Since their technique consisted of passing an ultraviolet beam across the full diameter of the shock tube and monitoring its intensity, they recognized that most of the apparent thickness they measured was in fact due to curvature of the shock caused by the boundary layer and was proportional to the boundary layer thickness.

I.1.3 Duff & Young 1961 (Ref. 3)

Following Lin & Fyfe's "discovery" of shock curvature, serious research into this phenomenon and its causes quickly took place. On the experimental side, the first investigation designed specifically to analyze shock shape was conducted by Duff & Young in, surprisingly, a shock tube only 28.6 mm in diameter (about 1 1/8"). Despite the difficulties inherent in attempting to measure shock shape in a tube whose radius (over which the variation takes place) is only about 5 times the diameter of the sensing probes, Duff & Young obtained several significant results. No variation of shock curvature with Mach number was noted over a range of Mach numbers from 1.84 to 6.33. As did Lin & Fyfe, they noted the inverse dependence of shock curvature on the square root of the initial pressure. More importantly, however, they also noted a deviation from this dependence at the lowest pressure and correctly predicted the existence of a regime of extremely low pressures where the flat plate boundary layer approximation does not hold. This regime, in fact, does exist and is discussed in more detail below.

Duff & Young came close to making an even more important discovery when, in explaining the scatter in their data, they commented that the shock shape seemed to be oscillating about its equilibrium shape as if it still remembered some of the details of its birth at the bursting diaphragm. It was apparently not suspected that this effect, if real, might have more than academic importance. Most researchers, in fact, seemed to pass it off as fancy. It will be

shown in this paper, however, not only that this effect is real but that there exists a broad regime of conditions in which it completely dominates the shock shape and possesses a magnitude many times that which might be expected.

Because of the scatter in their data and the unfavorable geometry of the experiment, all Duff & Young were able to determine about the shock shape itself (vs. radial position) was that it could be approximated by a spherical section. They also introduced the logical argument that in an extrapolation of the shock shape to the wall, the shock must approach the wall at a finite angle such that the normal component into the wave (outside the boundary layer) is supersonic.

I.1.4 Hartunian 1961 (Ref. 4)

The theory relating the growth of the boundary layer behind the shock to the shock curvature is very straightforward and will be outlined in the next chapter. The first theoretical solution of this problem was accomplished by Hartunian as a masters thesis at Cornell in 1954 but was not published until 1961 when the experiments of Lin & Fyfe and Duff & Young gave increased significance to the work. The case solved by Hartunian is that of a shock in a semi-infinite medium passing over a flat wall. The equations are solved for this geometrically simple "one-wall" case with only slightly more ease than in the subsequently solved two-wall and axisymmetric cases. The great simplification of this case lies in the ease with which the resulting analytic expression for the shock shape may be converted into numerical or graphical form. The more complex geometries result in infinite series and integrals which converge only slowly and were thus unavailable in graphical form for comparison with experiment until their evaluation in the present paper (see appendices C, D, and E). The parabolic profile of Hartunian's one-wall case is appropriate for comparison with experiments in the shock tube only in a limited zone not too near either the wall or the center of the tube.

Nevertheless, Hartunian's paper is extremely significant since the more useful geometrical cases have been solved using the same general method.

I.1.5 Johnson 1962 (Ref. 5)

At this stage in the development of shock shape knowledge what was needed was clearly a set of experiments combining the advantages of the large diameter shock tube (e.g. Lin & Fyfe) and the determination of shock shape by the measurement of arrival times at various end wall stations (e.g. Duff & Young). This need was recognized by Liepmann (see acknowledgment, Ref. 5), and under his supervision the first shock shape experiments in the GALCIT 17" shock tube were carried out by Johnson using specially constructed piezoceramic pressure transducers (similar to those used by Duff & Young) in the end wall. Unfortunately, the range of initial pressures covered in Johnson's experiments was limited by the same instrumentation problems which plagued Duff & Young. Initial pressures ranged from .03 to .1 mm Hg, practically the same range covered by Lin & Fyfe and comparable to the range of .1 to 20 mm Hg covered by Duff & Young in their smaller tube. Because of the favorable geometry of his experiments, however, Johnson was able to determine the shape of the shock wave in this regime with greater precision than were his predecessors. Thus it happened that all the shock shape experiments up to 1962 were conducted in the fairly narrow pressure regime in which the boundary layer theory of curvature production is valid and in which the gross curvature or apparent thickness varies with the inverse square root of the initial pressure. There was some evidence that this variation might not hold at extremely low pressures, but there was evidently no suspicion

that there might be a regime of higher pressures where the boundary layer theory fails completely to describe the shock shape. It was confidently felt that at higher pressures all deviations from planarity would be immeasurably small.

I.1.6 Daen & de Boer 1962 (Ref. 6)

In the course of an experimental investigation of relaxation processes in an integrated-schlieren-equipped shock tube, Daen & de Boer encountered unexpectedly large apparent zone thicknesses, much as had Lin & Fyfe in their similar experiments. Daen & de Boer were, however, aware of Hartunian's theory and were operating at higher initial pressures where the predicted curvatures were small. Their experiments, though, indicated the probable existence of curvatures 2 to 10 times those predicted by theory and which did not seem to follow the inverse square root pressure rule. Because they had no direct knowledge of the shock shapes, but could only infer their gross extent from density measurements integrated across the tube, they did not recognize that other, non-viscous, sources of shock non-planarity were present, but pointed out possible reasons for the discrepancy between their results and the predictions of Hartunian's theory. In particular, they presented a qualitative description of the flow at the foot of the shock. Considering the good agreement between Hartunian's theory and all the earlier experiments, it is not surprising that Daen & de Boer apparently did not realize that they were operating in a regime to which Hartunian's theory did not apply, but for which a new theory, based on upstream disturbances of the shock wave, would have to be developed.

At about the same time, other shock tube relaxation rate studies were being performed by Wray (Ref. 7). In these experiments, instead

of integrating across the entire tube diameter, Wray reduced the optical path length in recognition of the experiences of Lin & Fyfe. This technique improved the data at low initial pressures, but the data at high pressures had to be discarded because of tremendous scatter. The results of this paper indicate that this scatter was probably caused by the same type of upstream disturbances that troubled Daen & de Boer.

I.1.7 de Boer 1963 (Ref. 8 and 9)

Probably motivated by the difficulties which he and his associates encountered with their integrating-schlieren experiments, de Boer undertook a detailed and comprehensive study of the theory of shock curvature produced by a boundary layer. In this theory, he extends the analysis of Hartunian to the two-wall and axisymmetric cases and includes analyses of the effects of the flow at the foot of the shock, boundary layer transition, and the position of the contact surface. The main contribution of the analyses of the latter effects is that they are shown to be negligibly small. The correction for the flow at the foot of the shock is a qualitative step in the right direction and helps explain the deviation from inverse square root pressure dependence at very low initial pressures. The value of the correction for the partially turbulent boundary layer is yet to be demonstrated, since this correction is only of importance at extremely high pressures (above 100 mm Hg) and so far no shock shapes have been observed at these pressures which were not completely dominated by non-viscous transverse disturbances from upstream.

In his doctoral thesis (Ref. 8), de Boer also reports the results of a series of experiments with the integrating-schlieren apparatus similar to those of Daen & de Boer (Ref. 6). The zone thickness results of these experiments agreed quite well with the theory at initial pressures below 30 mm Hg. At higher pressures the apparent zone thicknesses were all much greater than predicted

by the theory. de Boer concluded that the deviations from theory were caused by irregularities in the shock tube surface. While irregularities such as windows and ports can definitely cause perturbations in the shock shape, it is more likely that the greater part of the deviation was caused by disturbances originating at the diaphragm. This is clearly indicated by the fact that de Boer was able to reduce the deviations from theory only very slightly (from say 6 times the theoretical value to about 4 times theoretical) by inserting a precision glass inner tube within the shock tube. That he blamed the remaining deviation on entrance effects at the beginning of the glass tube is an excellent example of the belief of most shock tube researchers that disturbances from the diaphragm could persist no more than a few diameters downstream.

I.1.8 Liepmann & Bowman 1964 (Ref. 12)

The research reported in the present paper is a continuation of the research on which a preliminary report was given in reference 12. In that publication it was indicated that there was a regime of high pressures in which upstream disturbances were dominant. It was also reported that definite evidence of shock shape dependence on diaphragm configuration in this regime had been obtained and graphs of typical shock shapes in the different regimes were presented. This paper will present the results of subsequent experiments which make it possible to analyze these regimes in detail. A chapter will also be included on the regime of extremely low pressures, which was not covered in the preliminary report of reference 12.

I.2 Possible Sources of Non-Planarity

The sources of non-planarity of the shock waves in a shock tube fall into two general categories--stationary and non-stationary effects. The stationary effects are steady in shock-fixed coordinates and include the influence of the boundary layer and through it surface roughness. At moderate pressures the boundary layer is thin compared to the tube radius and straightforward flat plate theory is applicable. At lower pressures the shock shape is complicated by the viscous interaction region at the foot of the shock and by the transverse curvature of the wall (in a circular tube; in a rectangular tube, corner effects become important).

The non-stationary effects produce shock shapes which vary with time and distance down the tube and include disturbances of protuberances and area changes, effects of non-plane contact surfaces, and disturbances originating from the non-ideal opening of the diaphragm. All these non-stationary effects take the form of transverse waves which originate at the disturbance and reflect back and forth across the tube, thus intersecting the main shock at different positions as the shock moves down the tube.

I.3 Shock Shape Regimes*

I.3.1 The Viscosity-Dominated Regime

The experiments reported herein show that the two general types of sources of non-planarity cause the shock shape theory to be divided into three regimes, two of them dominated by the stationary effects and one dominated by the non-stationary effects. Like any description of physical phenomena, this division is somewhat arbitrary and the regimes are not separated by perfectly sharp divisions, but by somewhat hazy zones. Nevertheless three quite distinctly different theoretical treatments must be given for the three regimes and the regimes of applicability of these theories are much broader than the transition zones between them.

The viscosity-dominated regime covers the very low initial pressures from the free molecule limit up to the pressure where the shock thickness has decreased to about $1/2$ the tube radius. The shock thickness and boundary layer thickness (these really cannot be defined in this region and the use of the terms "shock" and "boundary layer" is extremely loose) in this regime are both too large to be assumed "small" in comparison with the tube diameter. Moreover, the shock curvature is too great to be treated

*Here and throughout, the word "regime" is used to denote a set of conditions under which a particular phenomenon governs the shock shape with a particular set of physical laws. The word "region", on the other hand, is used to denote physical location, such as the "region behind the shock".

by a "small angle" analysis, and the irrotational testing region has disappeared, the contact surface (or turbulent mixing zone) being very close to, or even overlapping with, the shock. As can be seen from the results of chapter IV, the viscous interaction region where the shock and boundary layer join extends well into the tube and cannot be ignored. The shock thickness and shock strength varies considerably from the center of the tube to the walls and there are large variations in the properties of the flow behind the shock, these variations being both radial and axial. Although the shock shape is stationary in this regime and can be determined experimentally (see chapter IV) it would seem that a complete theory for this regime will be a long time in coming.

Because this regime is best understood as one in which there is a progressive departure from the predictions of boundary layer theory, the chapter devoted to the viscosity-dominated regime is deferred until after those in which the theory of the boundary layer regime is developed.

I.3.2 The Boundary Layer Regime

The boundary layer regime encompasses a fairly narrow band of pressures immediately above the viscosity-dominated regime. It is in this regime that the shock shape is closely predicted by the theory of Hartunian and de Boer, the axial extent or apparent thickness* varying as the inverse square root of the initial pressure. This regime is characterized by the boundary layer being thin enough that there exists a reasonable testing region of nearly irrotational flow behind the shock, and yet thick enough that transverse waves produced at the diaphragm or by protrusions in the tube are "choked off" and dissipated before the shock wave reaches the test section. The shock thickness will normally vary from about 30% of the tube radius at the low pressure end of the regime to about 3% of the radius at the high pressure end. The latter figure will depend on the length of the tube for the boundary layer regime extends to higher pressures in tubes of greater length/radius ratio.

*These are not identical in general, for the apparent thickness is the sum of the axial extent and the actual shock thickness. It is, of course, only the axial extent which should follow the $p_1^{-1/2}$ law.

I.3.3 The Transverse Wave Regime

The transverse wave regime takes in all initial pressures above the boundary layer regime. The shock shape in this regime is unsteady and describable by a weakly damped periodic function for geometrically symmetric disturbances (and hardly describable at all for asymmetric disturbances), the shape at any time or distance down the tube being dependent mainly on the magnitude and phase position of transverse waves created at the diaphragm or other disturbance. These waves reflect back and forth across the tube, decaying only slowly (like $t^{-1/2}$), the boundary layer being too thin to cause a noticeable speed-up of this decay.

The transition zone between this and the boundary layer regime is quite narrow and seems to occur at the initial pressure for which the boundary layer is just thick enough to cause closure at the disturbance when the shock is arriving at the test section. No upper limit on this regime has been discovered.

Figure I.1 gives a qualitative comparison of the shock shape regimes.

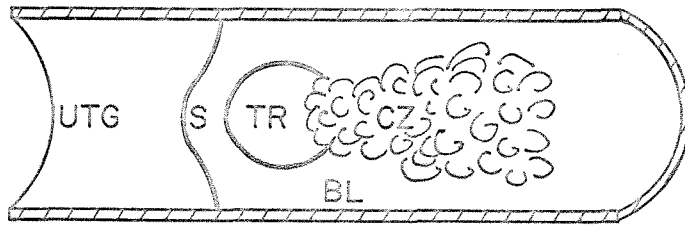


FIG. I.1a VISCOSITY-DOMINATED REGIME

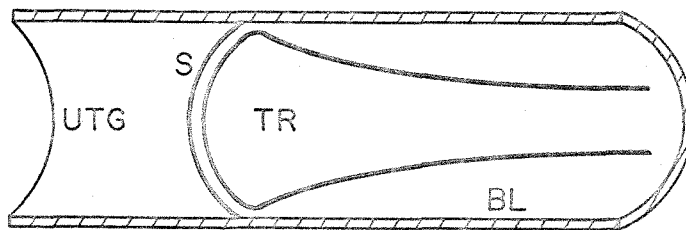


FIG. I.1b BOUNDARY-LAYER REGIME

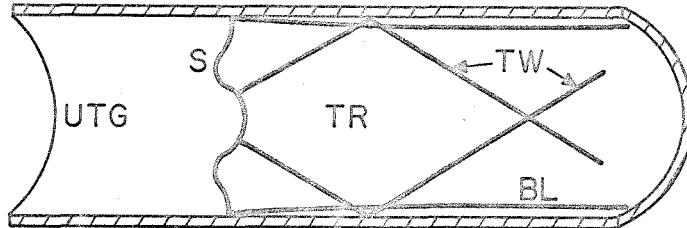


FIG. I.1c TRANSVERSE WAVE REGIME

- UTG = UNDISTURBED TEST GAS
- S = SHOCK
- TR = TESTING REGION
- CZ = CONTACT ZONE
- BL = BOUNDARY LAYER
- TW = TRANSVERSE WAVE

FIG. I.1
TYPICAL SHOCK SHAPES (SCHEMATIC)

I.4 Application of Shock Shape Knowledge

It has already been noted that shock tube experiments in which the shock wave itself is investigated using instrumentation which integrates across the tube may not be performed without due regard for shock shape. At the same time it is not sufficient to merely recognize that deviations from planarity* exist and introduce correction factors blindly, forcing the data to assume the expected form. In order to get meaningful results from experiments using schlieren, optical reflectivity, electron beam, or other such methods, it is necessary to know the precise shock shape for each experimental condition and correct the data accordingly. This procedure becomes easier and more successful if the experiments are conducted under conditions such that the deviations from planarity are as small as possible. It will be shown that this suggests operation in the upper part of the boundary layer regime. Thus a knowledge of the initial pressure corresponding to the transition from one regime to another becomes imperative. This pressure will vary from one shock tube to another. Its estimation in the important case of the transition between boundary layer and transverse wave regimes is discussed in chapter VII.

* In the past the word "curvature" has been used indiscriminately to describe all deviations from planarity other than tilt. Shock shapes under the influence of transverse waves, however, are so far from being spherical (see Fig. I.1) that its use in this regime seems ill advised. Statements to the effect that protrusions "increase the curvature" of the shock miss the point completely.

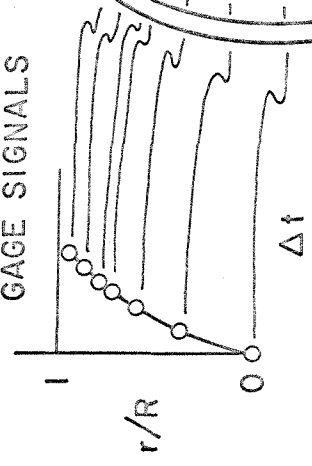
These same considerations are important when a new shock tube design is being considered. Not only may the length, radius, and operating range of a shock tube be matched with more intelligence, but it is possible that new concepts in shock tube design can lead to tubes capable of producing shock waves of much greater planarity than is presently attainable. These considerations are discussed in chapter IX.

I.5 General Experimental Procedure

All the shock shape measurements were made using the same basic technique: recording arrival times of the shock wave at various positions on the end wall on a set of carefully synchronized oscilloscopes and converting the arrival time differences into displacements by multiplying by the shock speed. The sensing gages were specially constructed thin-film heat transfer gages (see appendix B) providing up to 18 radial data points along a single radius and additional points on other radii, including a set of points extremely close to the wall for use in the viscosity-dominated regime. There were also symmetrically located gages for the detection of tilt. In addition the entire end plate could be rotated to check on angular variation of shock shape. In the transverse wave regime, for example, a quadrantal warp shows up which is related to the petaling of the diaphragm. In the boundary layer regime, however, the shock shapes were almost perfectly axisymmetric. See figure I.2 for a schematic diagram of the experimental procedure.

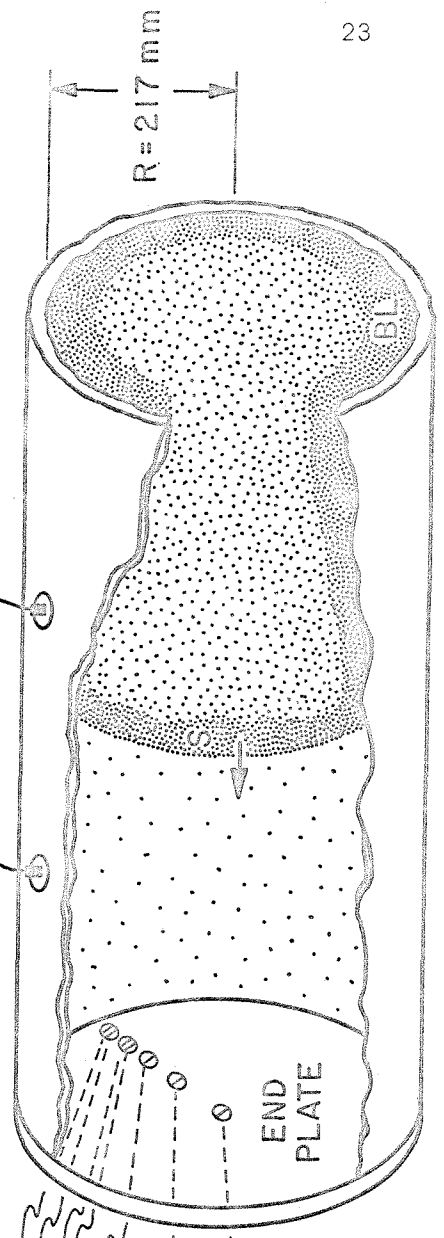
SHOCK SPEED MEASUREMENT

THIN-FILM
HEAT TRANSFER
GAGE SIGNALS



STOP
TIMER

START
TIMER



SYNCHRONIZED
OSCILLOSCOPES
FOR

ARRIVAL TIME
MEASUREMENT



SHOCK SHAPE

FIG. I. 2 GENERAL EXPERIMENTAL PROCEDURE

I.6 Preliminary Comment on Curve-Tracing Technique

The standard technique used in tracing curves through experimental data points involves drawing the smoothest, simplest curve possible through the vicinities of the data points or using a least squares fit to a known function. Often neglected is the fact that the size of the "vicinity" of a data point is determined by the accuracy and certainty of the measurement and that the least squares fit should always involve a weighting function expressing the relative accuracies of the various data points. Often the weighting function varies linearly over the range of the measurements. Many times it is quite complex, especially when (as in the present case) the data points are not independent. Only under special circumstances is the weighting function a constant (which therefore can be ignored).

A distinction must be made between two different types of plots. In a plot such as figure III.6 the data points from a great number of shocks are superimposed. If one were to draw a "mean" shock shape through this data it would not necessarily go through the center of all the points. On the other hand, in a plot such as figure V.4 or V.8 the data points for each case were obtained simultaneously and pertain to one particular shock wave. The curves drawn through them attempt, as closely as possible, to represent the actual shape of that particular shock. The next shock under identical conditions might have a very slightly different shape, but that one shock has only one true shape. The curve must therefore pass within the limit

of error of each data point. In these experiments that limit of error is a $\Delta(x/R)$ less than 10^{-4} . The limit of relative error between two adjacent gages located on the same glass plug and recorded on the same oscilloscope is even less. Thus shock slope measurements from two adjacent gages are very reliable.

A feel for the general shape of even the complex shock shapes was gained by observing optical studies of shocks produced under similar conditions and by imposing certain boundary and symmetry conditions, where applicable.

Since the shock shapes in the transverse wave regime could become quite complex, each has been drawn as the most likely shape, in the light of the above considerations, passing through each data point.

For a further discussion of data reduction technique, see appendix F.

II. BOUNDARY LAYER REGIME: THEORY

II.1 Formulation of the Problem

Consider a shock moving in a tube. Let the coordinate system be attached to the shock and move with it and be as shown in figure II.1. Then a detail sketch of a small segment of the shock with slope $dx_{sh}/dr = \sigma$ will be as shown in figure II.2. From the latter it is evident that if σ is small, then to order σ the induced vertical velocity behind the shock will be given by

$$v(x_{sh}, r) \approx v(o, r) \approx (U_1 - U_2)\sigma = (U_1 - U_2) \left. \frac{dx}{dr} \right|_{sh} \quad (\text{Eqn. 2.1})$$

Here we have made the above small angle assumption and, consistent with it, have applied the condition at $x = 0$ instead of at the actual shock position. Once $v(o, r)$ is known, then $x_{sh}(r)$ may be determined by integration of equation 2.1. The determination of $v(o, r)$ is made by assuming irrotational potential flow (valid for small σ) in the region behind the shock and calculating $v(x, r)$ throughout the field bounded by the centerline of the tube and the fictitious wall located at the displacement thickness of the laminar wall boundary layer.

In order to complete the problem, we need the boundary conditions on v at the other edges of the region--along the centerline of the tube and at the wall. The first of these is, by symmetry,

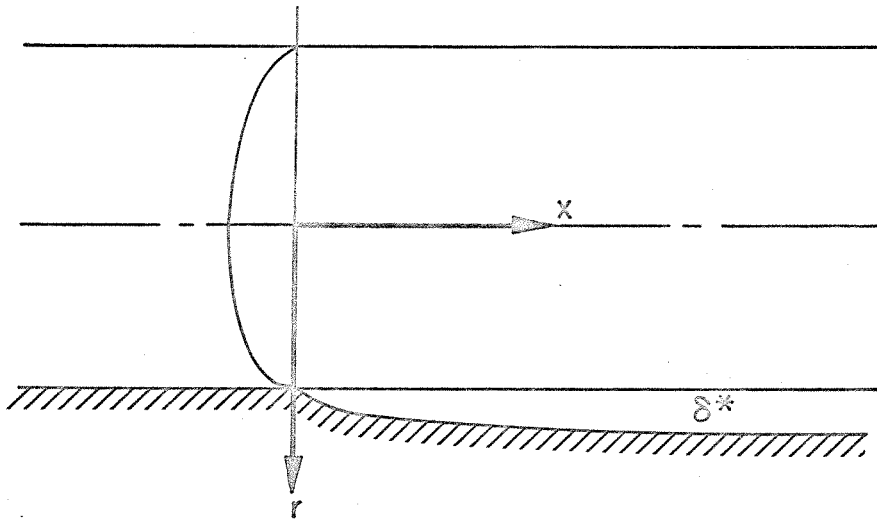


FIG. II.1
COORDINATE SYSTEM

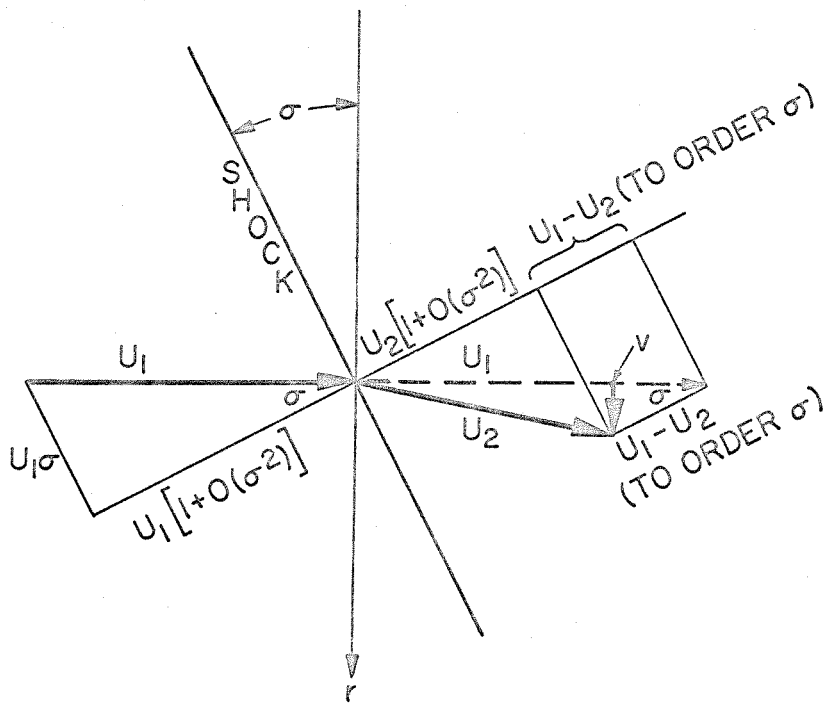


FIG. II.2
IMPLICATION OF SMALL-ANGLE APPROXIMATION

simply

$$v(x,0) = 0 \quad (\text{Eqn. 2.2})$$

We assume that the equivalent inviscid flow is parallel to the fictitious "displacement thickness" wall and thus using the usual slender body approach the last boundary condition becomes

$$v(x,R) = U_2 \frac{d\delta^*}{dx} \quad (\text{Eqn. 2.3})$$

where, in the laminar case,

$$\delta^* = A^* x^{1/2} \quad (\text{Eqn. 2.4})$$

Though the analysis can be carried out for a more general dependence of δ^* on x , so as to apply also to turbulent boundary layers, it turns out that only the beginning of the boundary layer significantly affects the shock shape and throughout the entire regime in which the theory has any validity, this part of the boundary layer is entirely laminar. Thus the analysis here will be for the laminar case.

II.2 Results of the Potential Solution

In appendix D it will be shown that the preceding boundary conditions applied to a region of potential flow behind the shock lead to the following solution for the vertical velocity in the region:

$$v(x,r) = \frac{U_2 A^*}{\sqrt{2\pi}} \int_0^{\infty} \frac{I_1(m\rho r)}{I_1(m\rho R)} \frac{\cos \rho x}{\sqrt{\rho}} d\rho \quad (\text{Eqn. 2.5})$$

This in turn leads to the following shock shape:

$$x_{sh} = \left(\frac{R}{2\pi m}\right)^{1/2} \frac{A^* U_2}{U_1 - U_2} \int_0^{\infty} \frac{I_0(t\eta) - 1}{I_1(t) t^{3/2}} dt \quad (\text{Eqn. 2.6})$$

where $\eta = r/R$ and $m = (1 - M_2^2)^{1/2}$.

Thus we see that the shock shapes are similar for all flow conditions within the regime, for the integral which contains the variation with r does not contain any flow variables. Thus in order to analyze the theoretical effect of the flow variables, it is sufficient to explore their influence on the axial extent θ which is just x_{sh} for $\eta = 1$.

In appendix E the shock shape integral is evaluated and its value vs. η leads to the shape marked "boundary layer theory" which appears in many of the figures. At $\eta = 1$ this integral has the value 2.78. Thus the axial extent (non-dimensionalized with respect to the tube radius) is given by

$$\frac{\theta}{R} = \frac{2.78 A^* U_2}{(2\pi m R)^{1/2} (U_1 - U_2)} \quad (\text{Eqn. 2.7})$$

In appendix D it will also be shown that the radius of curvature of the shock at its center can be calculated (this quantity is very important in optical reflectivity measurements, for example). Its reciprocal, the curvature at the centerline, is given by the following expression:

$$\left. \frac{d^2 x_{sh}}{dr^2} \right|_{r=0} = \frac{U_2 A^*}{2(2\pi m)^{1/2} (U_1 - U_2) R^{3/2}} \int_0^{\infty} \frac{\sqrt{x} dt}{I_1(x)} \quad (\text{Eqn. 2.8})$$

The integral in this expression is evaluated in appendix D and has the value 6.38. Thus the ratio of the tube radius to the shock radius of curvature at its center is given by

$$\frac{R}{R_0} = R \left. \frac{d^2 x_{sh}}{dr^2} \right|_{r=0} = \frac{6.38 U_2 A^*}{2(2\pi m R)^{1/2} (U_1 - U_2)} = 1.15 \frac{\theta}{R} \quad (\text{Eqn. 2.9})$$

Thus the determination of the theoretical axial extent and the theoretical radius of curvature at the centerline are dependent on the calculation of the same function of the flow variables. The problem then reduces basically to the determination of the displacement thickness coefficient A^* .

II.3 Determination of A^* , Final Results

If the boundary layer equations for the compressible flow behind a shock wave on a flat plate (we ignore the transverse curvature) are transformed using Stewartson (Ref. 14) variables and properly renormalized to eliminate Mach number dependence (approximately, of course), then the Blasius equations are obtained with non-Blasius boundary conditions. Since the flow is compressible, any solution must involve the energy equation. The Crocco integral relation is used and the particular boundary condition chosen (for the first iteration) that $h_w = h_1$. It can be shown that the velocity profile solution obtained from this analysis is exact only in the weak shock limit. Nevertheless, this analysis due to Hartunian (Ref. 34) is widely used. The resulting expression for the displacement thickness is

$$\delta^* = A^* \sqrt{x} = - \frac{\epsilon \alpha \delta}{\sqrt{\pi} C} \quad (\text{Eqn. 2.10})$$

where

$$\alpha = \frac{\frac{\gamma+1}{\gamma-1} + \frac{u_2}{u_1} [1 + \epsilon(2-\sqrt{2})]}{\frac{\gamma+1}{\gamma-1} - \frac{u_2}{u_1}}, \quad \epsilon = \frac{u_1 - u_2}{u_2} \quad (\text{Eqn. 2.11 a,b})$$

and

$$C = \sqrt{\frac{\rho_2 \mu_2}{\rho_w \mu_w} [1 + \epsilon(2-\sqrt{2})]}, \quad \delta = 2 \sqrt{\frac{v_2 x}{u_2}} \quad (\text{Eqn. 2.11 c,d})$$

Now the above is a fairly complicated function of Mach number. If, however, we concern ourselves primarily with Mach numbers greater than three, then we may make strong shock approximations, in particular that

$$\frac{u_1}{u_2} \rightarrow \frac{\gamma+1}{\gamma-1} = 4 \quad \text{for } \gamma = 5/3 \quad (\text{Eqn. 2.12})$$

e.g. Argon

and the equation for A^* simplifies to

$$A^* = .475 \left(\frac{u_1 - u_2}{u_2} \right) \sqrt{\frac{RM}{R_e}} \sqrt{\frac{T_1 \mu_w}{T_w \mu_1}} \quad (\text{Eqn. 2.13})$$

where we have introduced the undisturbed Reynolds number which is defined as

$$R_e = \frac{\rho_1 a_1 R}{\mu_1} \quad (\text{Eqn. 2.14})$$

The one term involving the velocities which we have not evaluated has been left in order to cancel a reciprocal term in the equation for $\frac{\theta}{R}$. It is at this point that the assumptions made can greatly affect the Mach number dependence appearing in the solution. If one assumes that $T_w = T_1$, then the square root Mach number dependence will remain. If, on the other hand, one assumes that some mean value of the temperature within the boundary layer should better represent T_w in this equation, then

$$\frac{T_w}{T_1} - 1 = e \frac{T_2}{T_1} - 1 \quad (\text{Eqn. 2.15})$$

and if we arbitrarily choose $\epsilon = 1/2$, (the result is not very sensitive to this choice) and linearize for high Mach numbers where $T_2 \gg T_1$, then $T_w \approx \frac{1}{2} T_2$ and

$$\sqrt{\frac{T_1 \mu_w}{T_w \mu_1}} = \frac{T_1}{T_w} \frac{1-\omega}{2} = \frac{6.4}{M_1^2} \frac{1-\omega}{2} \approx 1.32 M^{\omega-1} \quad (\text{Eqn. 2.16})$$

Then the equation for A^* becomes

$$A^* = - .628 \frac{u_1 - u_2}{u_2} \sqrt{\frac{R}{R_e}} M^{\omega-1/2} \quad (\text{Eqn. 2.17})$$

and the Mach number dependence has been weakened. A physical picture of how this takes place can be gained by considering the displacement thickness to be the sum of two separate thicknesses-- one due to the velocity profile (and for the shock tube problem this part is always negative) and one due to the temperature profile. If it is assumed that $T_w = T_1$, then the cold wall induces a flow toward itself, thereby increasing the negative displacement thickness. If, on the other hand, one assumes $T_w > T_1$, then this thermal contribution is reduced. As the Mach number (and thus T_2) goes up, the wall temperature deviates more and more from T_1 , therefore the negative displacement thickness does not grow as quickly with increasing Mach number.

When this result is substituted in equation 2.7 and M_2 is computed from the strong shock limit, the final expression for the axial extent becomes

$$\frac{\theta}{R} = - .737 \frac{M^{\omega-1/2}}{\sqrt{Re}} \quad (\text{Eqn. 2.18})$$

This is the strong shock limit for argon (or any other monotomic gas) based on a rather simpleminded approach. In actuality the coefficient is not .737 but a function of Mach number and has been plotted by de Boer based on Mirels' (Refs. 15,16,17) boundary layer work. Using this plot (Fig. 9, Ref. 8), we find that over the entire Mach number range of these experiments (about $3 < M < 11$) the variation in the coefficient just about cancels out the $\omega^{-1/2}$ power variation and the axial extent is independent of Mach number. This result will be adopted and the following expression for the axial extent will be consistently used to represent the theory for the boundary layer regime:

$$\frac{\theta}{R} = \frac{1.13}{\sqrt{Re}} \quad [\gamma=5/3] \quad (\text{Eqn. 2.19})$$

The minus sign has been dropped. Its significance was that the deviation of the shock from a plane was in the negative x direction. In comparing the experimental data with theory, the origin will be placed always at the center of the shock and x_{sh} and θ will be positive in the positive x or "up the tube" (toward the diaphragm) direction.

Using equation 2.9 and equation 2.19, one can determine the theoretical radius of curvature of the shock at its center to be:

$$\frac{R_0}{R} = .77 \sqrt{Re} \quad [\gamma=5/3] \quad (\text{Eqn. 2.20})$$

If the boundary layer for $\gamma = 7/5$ (e.g. nitrogen) is calculated, an equation comparable to equation 2.18 is obtained:

$$\frac{\theta}{R} = - .467 \frac{M^{\omega-1/2}}{\sqrt{R_e}} \quad (\text{Eqn. 2.21})$$

It will be assumed that the coefficients of equations 2.18 and 2.21 are in the same ratio as the axial extents in argon and nitrogen at all Mach numbers, and therefore that an equation for nitrogen comparable to equation 2.19 for argon exists, in which case:

$$\frac{\theta}{R} = \frac{.715}{\sqrt{R_e}} \quad [\gamma=7/5] \quad (\text{Eqn. 2.22})$$

Then for the central radius of curvature of the nitrogen shock, the relation is:

$$\frac{R_0}{R} = 1.22 \sqrt{R_e} \quad [\gamma=7/5] \quad (\text{Eqn. 2.23})$$

Note that the γ dependence implied in the above equations is very close to the $(\gamma-1)$ dependence predicted by Johnson on the basis of a spherical shape. In fact, equations 2.19 and 2.22 can be combined into one equation which should approximately represent the boundary layer theory for all gases:

$$\frac{\theta}{R} = \frac{1.62 (\gamma-1)^{.89}}{\sqrt{R_e}} \quad (\text{Eqn. 2.24})$$

III. BOUNDARY LAYER REGIME: EXPERIMENTS AND RESULTS

III.1 Shock Shapes: Comparison With Theory

The data from 22 shock tube runs is plotted in figure III.1 along with the theoretical curve. Considering all the assumptions in the theory, the agreement is as good as can be expected.

The theoretical shape reaches a physically impossible point of tangency with the wall at

$$(x/R)R_e^{1/2} = 1.13 \quad (\text{from Eqn. 2.19})$$

while the actual shape approaches the wall at a finite angle. This angle of intersection with the wall is, of course, distorted by the stretching of the x/R coordinate in the normalization. The shock shape for $p_1 = 10\mu$ Hg is replotted to true scale in figure III.2 along with the corresponding theoretical shape. The shock thickness as determined from the rise-time of the heat transfer signal is also shown on this plot.

Up to $p_1 = 170\mu$ Hg, there is a consistent approach to the theoretical curve as p_1 is increased. At higher pressures, however, the shocks are not completely axisymmetric and the shape can deviate either above or below the theoretical curve depending on the angular location of the radius along which the measurements are taken. The deviations also depend on other factors, such as the Mach numbers, the diaphragm configuration, and the tube length. These deviations,

which are just noticeable at 300μ Hg are quite pronounced at 500μ Hg and are huge above a pressure of 1 mm Hg. This is the transition region to the transverse wave regime and thus data for runs above $p_1 = 170\mu$ Hg will not be further discussed in this chapter.

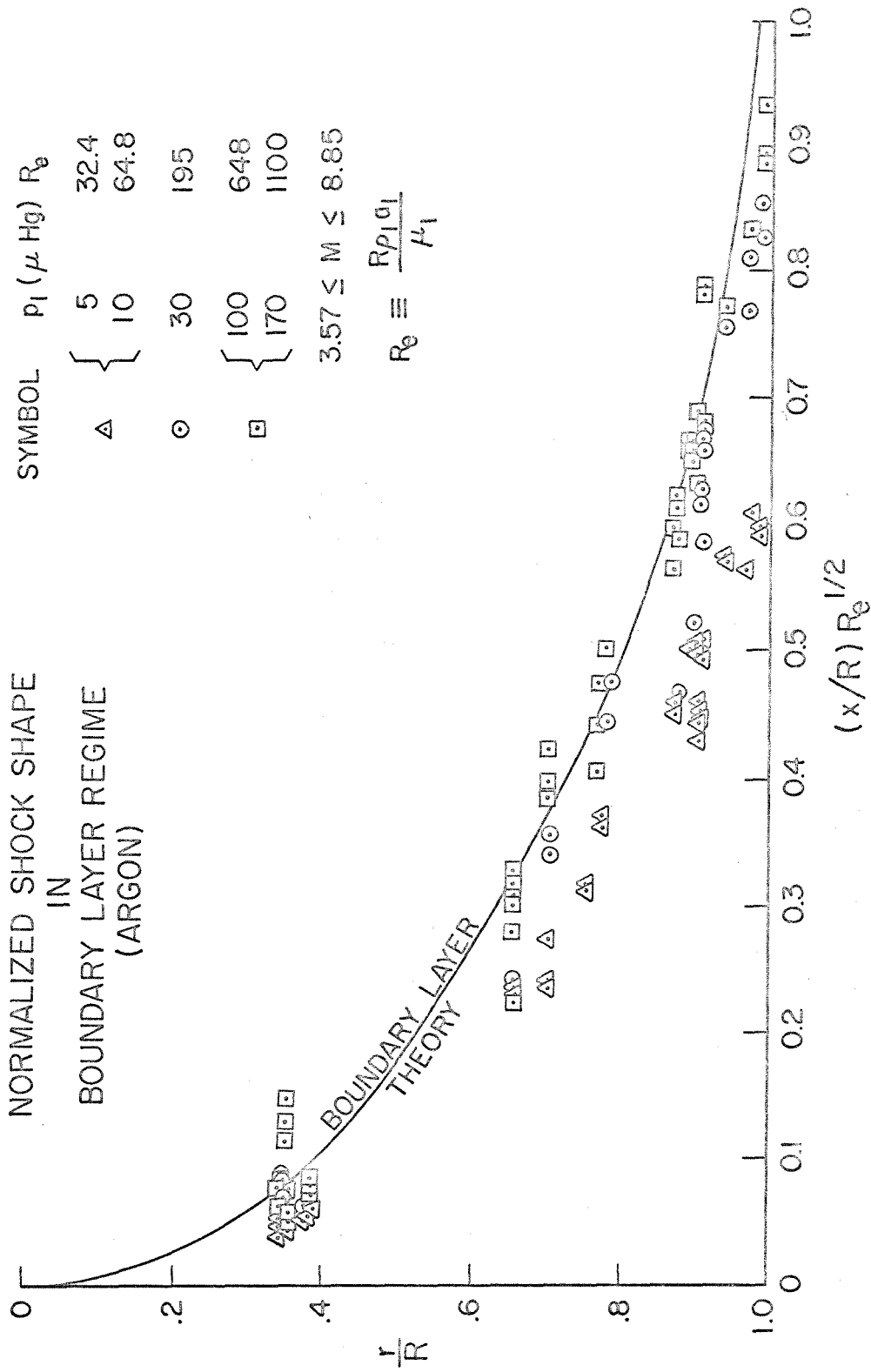


FIG. III.1

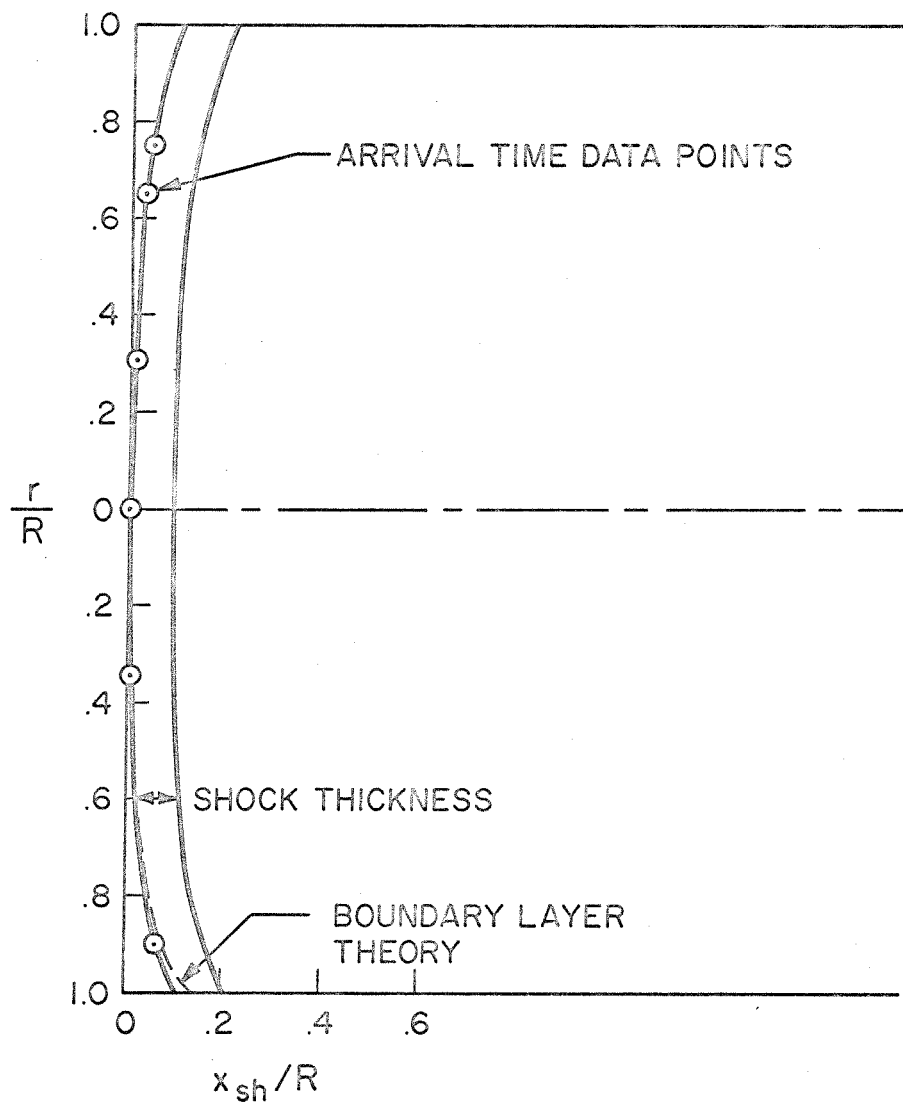


FIG. III. 2
 TRUE SCALE EXPERIMENTAL
 SHOCK SHAPE AT $P_1 = 10 \mu \text{ Hg}$ (ARGON)
 ($M = 8.0$)

III.2 Variation of "Axial Extent" With Re

Using thin-film heat transfer gages flush with the end wall of the shock tube, it is possible to measure shock shapes out to within about 1 mm of the side wall (depending on how small one can make the film and how accurately it can be located), but since the film must be insulated from the walls, it is impossible to measure the shape all the way to the wall. Therefore in order to avoid the necessity for extrapolation and the consequent introduction of error, the axial extent out to some arbitrary percentage of the radius will actually be used for comparison with the theory. This has the additional advantage that at some point away from the wall the theory is less affected by its "incorrect boundary condition" at the wall. For this purpose 80% of the radius has been arbitrarily selected and a quantity $\Delta x(.8)$ is defined in figure III.3. In the boundary layer and viscosity-dominated regimes this quantity is simply equal to $x_{sh}(r/R=.8)$, but it has been defined in such a way as to have a more general meaning which will be important in the transverse wave regime where the shock shapes are complex. In figure III.4 this quantity is plotted vs. initial pressure.

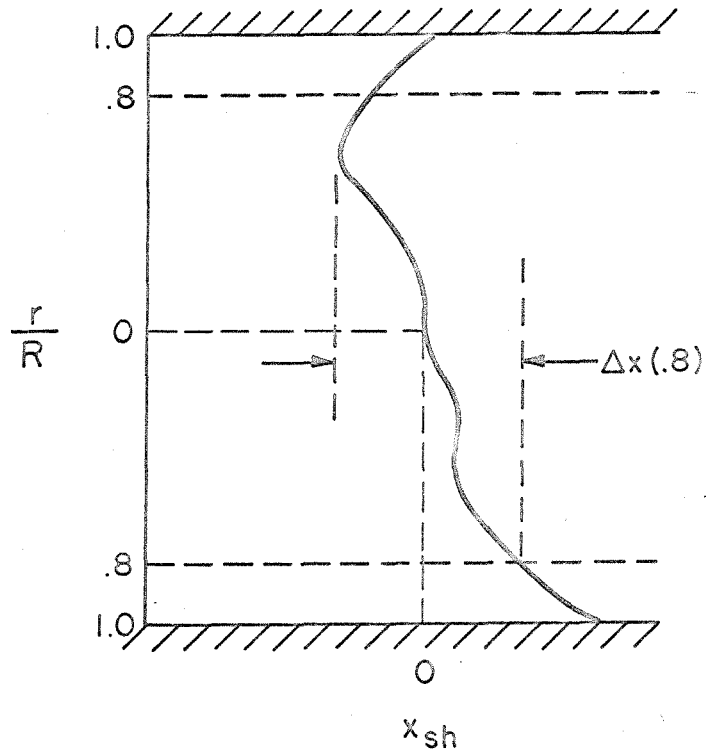


FIG. III. 3
DEFINITION OF $\Delta x(.8)$

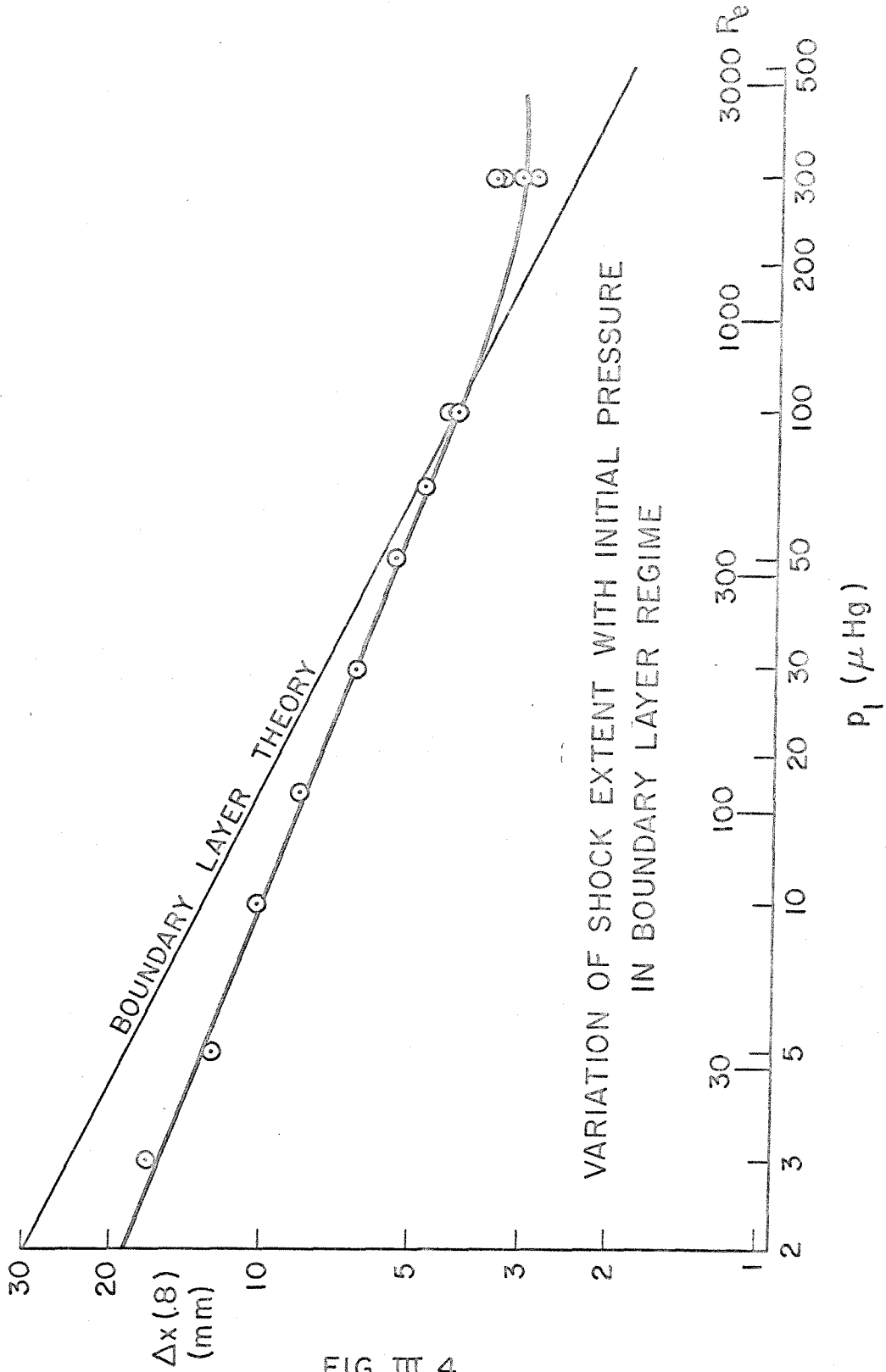


FIG. III.4

III.3 Effect of Mach Number

The analysis of chapter II predicts that the normalized shock shape will be independent of all flow variables and that the axial extent will be independent of Mach number within the range $3 < M < 11$. Then shots at different Mach numbers but otherwise identical conditions should produce identical shock shapes. In order to test this independence of Mach number a series of shots were made in argon at 10μ Hg with identical diaphragm configurations, but with half the shots using helium as the driver gas resulting in $M = 9.1$ and half the shots using nitrogen in the driver, yielding $M = 6.4$. The results are plotted in figure III.5, each data point shown being the average over all the shots at that Mach number at the indicated radial position. The use of more than one shot at each Mach number was necessitated by the random fluctuation in shock shape noted by Duff and later by Johnson. Though such fluctuation is very small at 10μ Hg (which is why that pressure was chosen for the test) it is still larger than the variation due to Mach number.

The results of the test show the shock at the lower Mach number to have a curvature apparently very slightly larger than at the higher Mach number. The difference is so slight, however, that it is easily within the expected statistical variation. If 100 shots were made at each Mach number and such a difference remained, then it could safely be attributed to the Mach number. As it is, the only

conclusion that can be drawn is that if there is an effect due to Mach number, it is extremely small. The theoretically predicted independence of Mach number is therefore, for all practical purposes, confirmed.

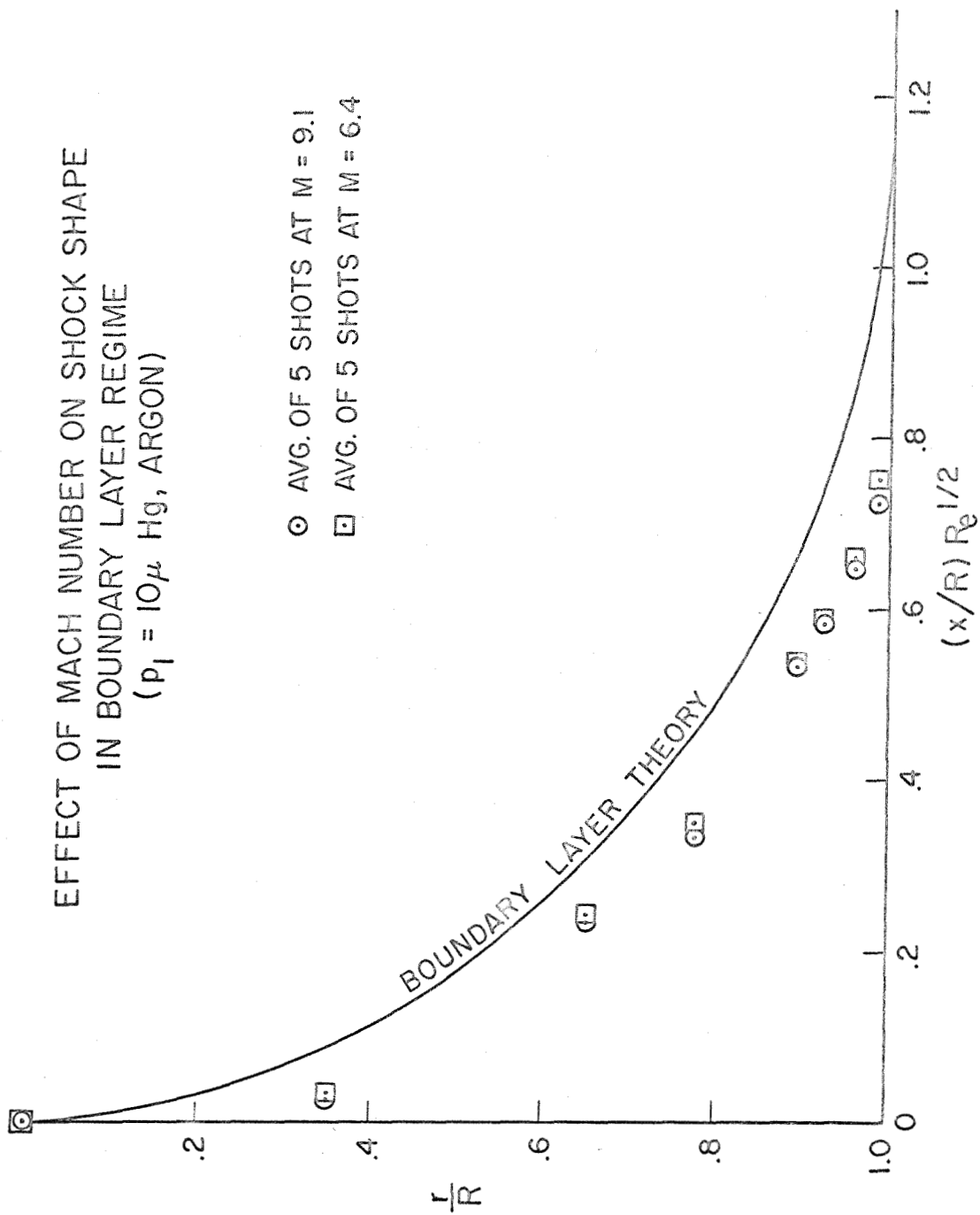


FIG. III.5

III.4 Miscellaneous Geometrical Effects

In the preceding sections, the effects of R_e and M have been covered, both theoretically and experimentally. The influence of ω has only been partially taken into account. The effect of γ as given in equation 2.24 has not been verified. Since the theory involves only that curvature caused by the vertical velocity induced by the boundary layer, the shock shape predicted is independent of the diaphragm configuration, the blades used to rupture the diaphragm, the length of the tube, etc. In order to evaluate the actual effect of these details, a series of shots at an initial pressure of 100μ Hg was made, using various combinations of the above mentioned geometric details. The results of this test are plotted in figure III.6. Enclosed in the rectangular markings are all the data points for tests using the full length of the shock tube, the ratio of tube length to radius being 96. These tests included the following variations:

- (1) Diaphragm material. Thickness varied between .006 and .020 inches of aluminum.
- (2) Blade shape. Two sets of knife edges were used to rupture the diaphragms. One curves deeply away from the diaphragm in the center in order to allow the diaphragm to bulge out considerably under the pressure difference before contacting the blades and bursting. The other set of blades is flat and, for the same diaphragm material, causes rupture at a smaller pressure difference.

- (3) Diaphragm aperture. For several of the shots part of the diaphragm section was blocked off, creating an area discontinuity at the diaphragm. For part of these shots the top half of the tube was blocked and for others the lower half was blocked. Thus for the same area ratio there were different asymmetrical configurations. The remainder of the shots were made with the entire tube unblocked. The partial diaphragm configuration and technique will be treated more fully in the next chapter.
- (4) Driver pressure and Mach number. As a consequence of the above variations in geometry, driver pressure and Mach number varied. Since their theoretical effect is also nil, no attempt was made to prevent this variation.

As can be seen from figure III.6, all the shock shapes throughout these tests at $L/R = 96$ were identical. There did not even seem to be any increase in the random variation present in shots produced under identical conditions. The data points which deviated the most were those nearest the wall when the diaphragm was blocked asymmetrically, and the maximum displacement of these data points from the other points was only $2/10$ of a mm.

The data points in the circles and triangles are for shots made with the tube shortened to allow less time for damping of disturbances from the diaphragm. For $L/R = 42.8$ we see that a slight tilt has been introduced, the data points being displaced as much as 1 mm from the normal points. As the tube is shortened further, it is

evident that a complex "wiggly" shape is superimposed on the normal equilibrium shock shape. These results indicate that it is possible to pass into the transverse wave regime by shortening the tube as well as by increasing the initial pressure. How these are connected will be discussed in detail in chapters VII and VIII.

It is concluded that as long as the shock tube is operated within the boundary layer regime, upstream geometry and diaphragm configurations have no significant effect on the shock shape. Moreover it appears likely that the small random variation in shock shape which does exist, since it is not increased appreciably by artificially varying the diaphragm rupture shape, is due to some statistical process such as the turbulent mixing in the contact region. If this is the case, then even if a shock tube were infinitely long, assuring the damping of all waves originating at the diaphragm, the random variation in shock shape at low pressures (admittedly very small) would still persist.

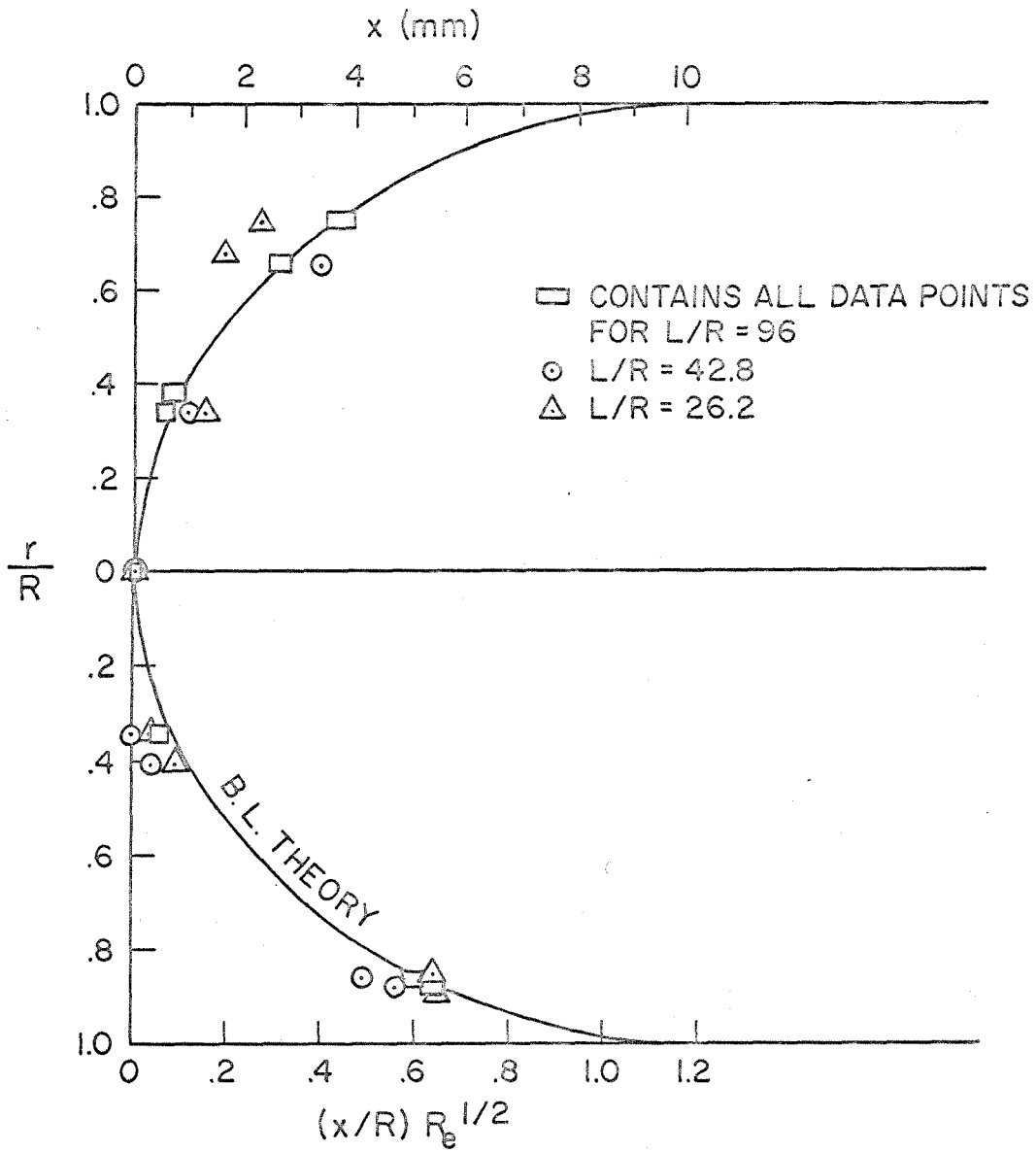


FIG. III.6

MISCELLANEOUS GEOMETRIC EFFECTS ON SHOCK SHAPE IN BOUNDARY LAYER REGIME (ARGON, $P_1 = 100 \mu$ Hg)

IV. VISCOSITY-DOMINATED REGIME

A description of some of the difficulties which must be faced by a general theory of shock shape in the low pressure viscosity-dominated regime has been given in section I.3.1. Only one of those difficulties has been faced theoretically thus far--that of the interaction between the shock and the boundary layer which it induces. This problem was considered as an order of magnitude correction to the axial extent by de Boer. His approximate analysis was undertaken to explain small deviations from the theory at the lower end of the boundary layer regime. A more ambitious analysis of this interaction region was performed by Sichel (Ref. 13), in which he gets an approximate solution by linearizing both the boundary layer equations and the transonic equations and matching the solutions in the viscous shear layer and in the non-Hugoniot shock. His linearization limits the applicability of the results to Mach numbers below about 1.2 and his geometry (two-dimensional) and other restricting assumptions do not well represent conditions in the shock tube. Nonetheless, his work is an invaluable first step toward the solution of this difficult problem. Perhaps the few experimental results presented here will spur further work, both theoretical and experimental, in this area.

These experiments are definitely exploratory in nature. The instrumentation was pushed to its limit in many respects and measured quantities cannot be determined with the accuracy possible in the

experiments in the other regimes. For example, measurements of initial pressures of .001 mm Hg (1μ Hg) and .0005 mm Hg ($1/2 \mu$ Hg) are probably accurate only to within 10% to 20%, whereas measurements of much higher pressures have about the same absolute uncertainty, making the relative or percentage errors much less. At these extreme low pressures there is probably significant contamination of the test gas (argon) with water vapor, oil vapor, and traces of air (leak rate of the tube was about 5×10^{-6} mm Hg/min). Thus while the shock shapes were measured with considerable accuracy, the pressure and gas to which these shapes correspond is not known with great precision.

It has been shown that if the shock shape is normalized with respect to the tube radius and a properly defined Reynolds number (which is proportional to the initial pressure) the shock shapes for all conditions in the boundary layer regime fall on a single theoretical curve. Figure IV.1 is a plot of the shock shapes in the viscosity-dominated regime. It shows that as the initial pressure is lowered, the shock shape departs further from the theoretical curve. The axial extent vs. initial pressure is plotted in figure IV.2 without having been normalized with respect to the Reynolds number. This plot shows that down to about 3μ Hg the inverse square root pressure law is followed fairly well, the shock extent being less than predicted by boundary layer theory, but still increasing as the pressure is lowered. Then as the pressure is reduced beyond 1μ Hg we see that the shock curvature has apparently

reached a maximum. Thus in the GALCIT 17" shock tube (and, we would expect, in any other tube of similar radius) the upper limit of the "fully developed" viscosity-dominated regime is about 1μ Hg. Above this pressure there is a very gradual transition to the boundary layer regime.

Figure IV.3 is a plot of the shock* profile at $.5\mu$ Hg, showing both the shape and thickness of the shock. On the same plot is a graph reflecting the shock strength variation between the tube centerline and the wall. It is seen that the shock strength drops off to well below its central value well out in the tube, then decreases rapidly toward zero in a sub-layer of the boundary layer at the wall. Note that in this experiment the shock thickness at its center is of the order of the radius of the tube.

The shape of the response of the thin-film heat transfer gage is markedly different at these extreme low pressures also. Instead of the smooth response resembling the ideal Navier-Stokes profile which is obtained at all higher pressures, the gage at these pressures produces a response with an almost discontinuous increase in slope about halfway to its peak. This response is shown in figure IV.4 and may be an indication that the contact surface is partially overlapping the shock.

*As noted on page 15, the words "shock" and "boundary layer" are used loosely in this regime. This is particularly true at the lowest pressures where such terms are really inappropriate for describing the complex non-equilibrium zones encountered.

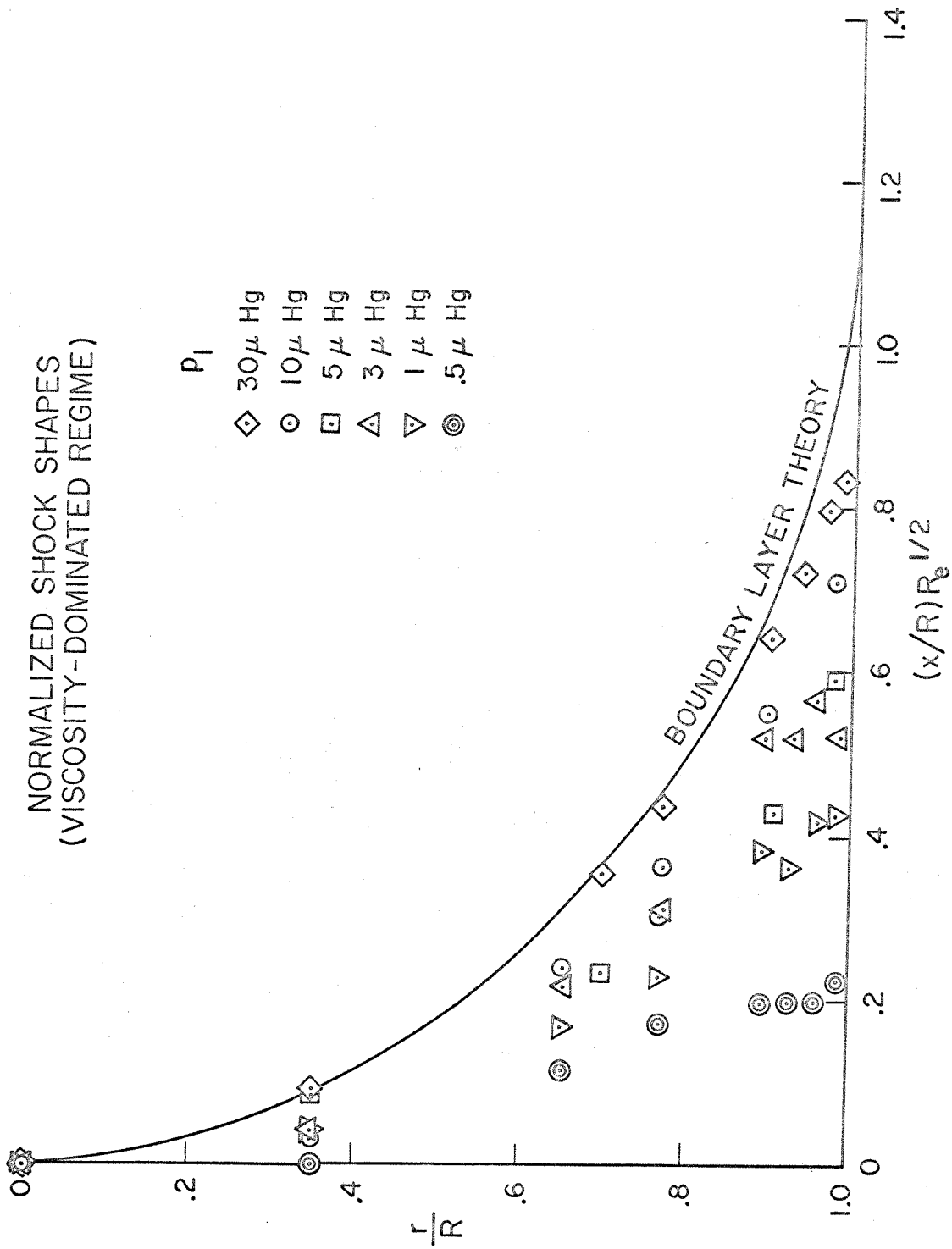
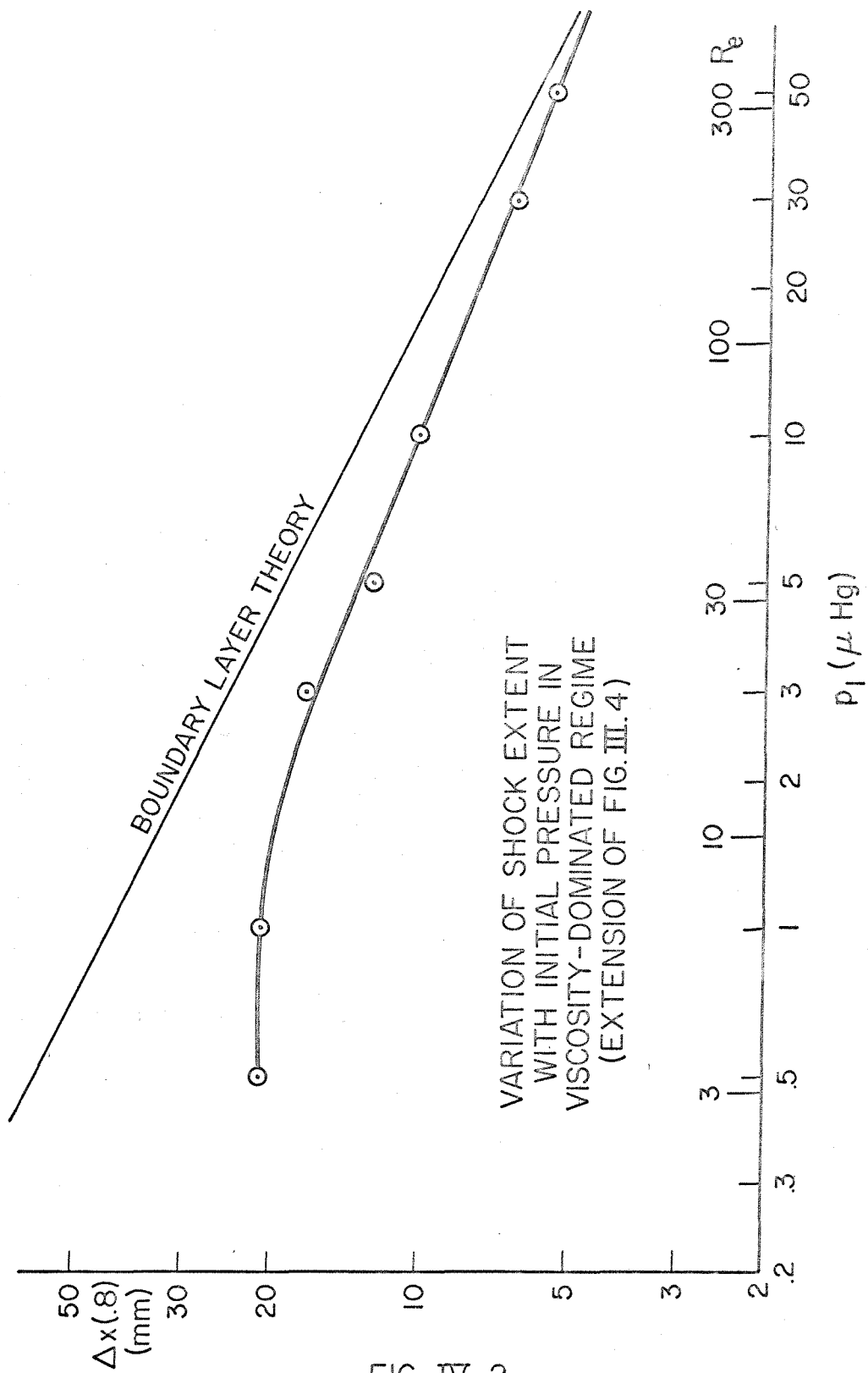
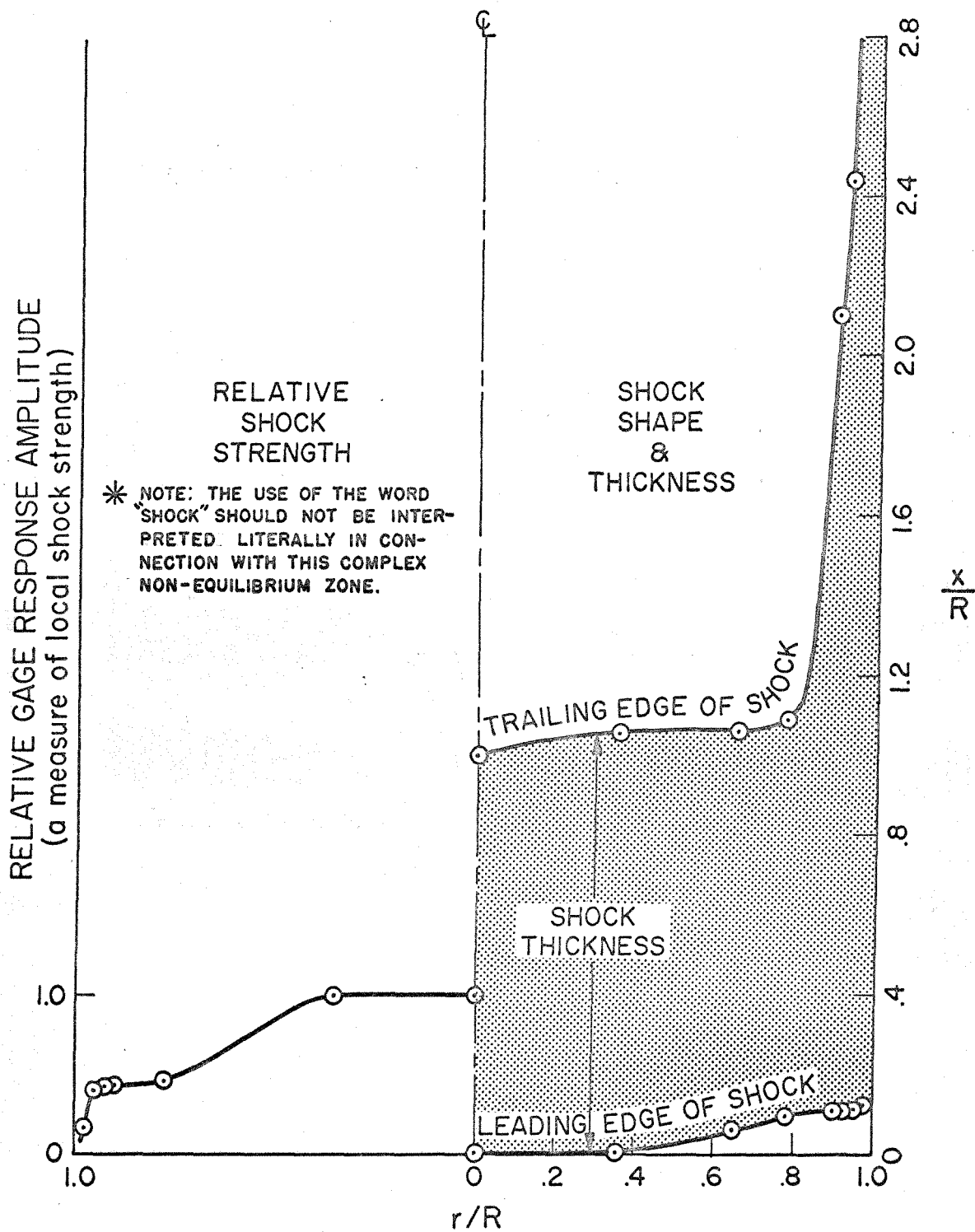


FIG. IV.1



VARIATION OF SHOCK EXTENT WITH INITIAL PRESSURE IN VISCOSITY-DOMINATED REGIME (EXTENSION OF FIG. III. 4)

FIG. IV. 2



* FIG. IV.3
SHOCK PROFILE AT EXTREMELY
LOW PRESSURE ($p_1 = .5 \mu \text{ Hg}$)

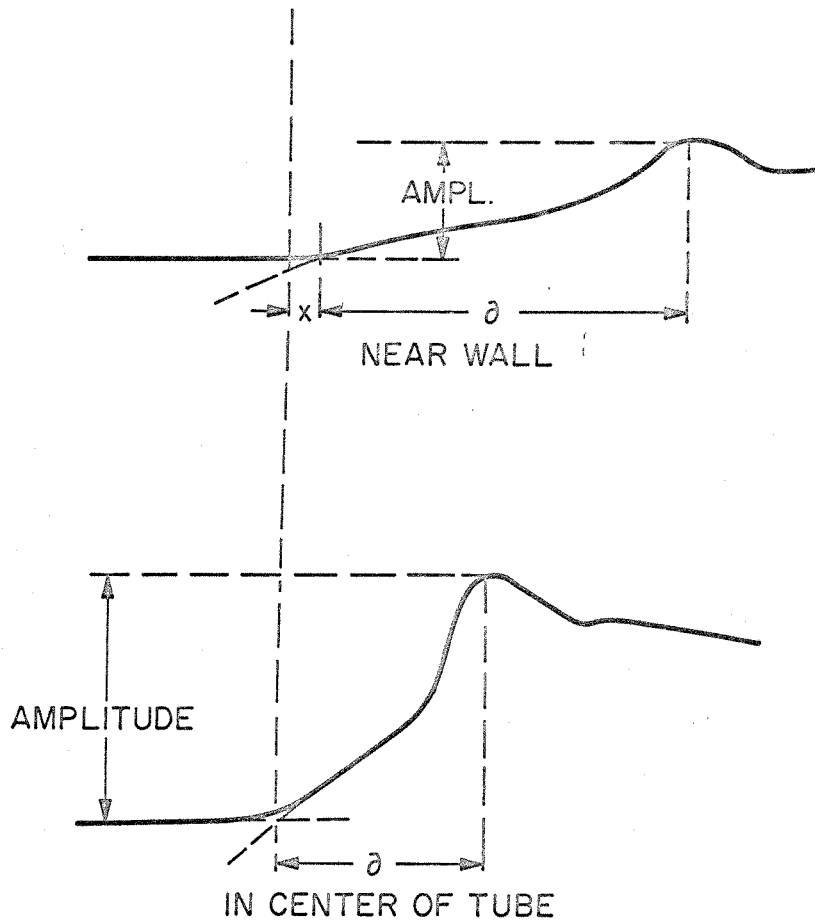


FIG. IV. 4
 TYPICAL HEAT TRANSFER
 THIN-FILM GAGE RESPONSES AT
 EXTREMELY LOW PRESSURE
 ($p_1 = .5 \mu \text{ Hg}$, $M = 11.2$)

V. TRANSVERSE WAVE REGIME: EXPLORATORY EXPERIMENTS

V.1 Departure From Boundary Layer Theory

In chapter III it was noted that the shock shape begins to deviate from theory as either (1) the initial pressure is raised or (2) the tube is shortened. All the experiments reported in this chapter took place over the full length of the tube, and in argon. Thus there is a one-to-one correspondence between the initial pressure and the Reynolds number. In the text and in the titles of graphs the term "pressure" or "initial pressure" is generally used so that a physical "feel" for the conditions is retained as much as possible. The independent variable on the graphs, however, is given both ways so that the data may be used as a guide to shots in other tubes. Even though the Reynolds number is the proper independent variable for the boundary layer theory, it should not be expected that departures from the theory will also be universal functions of this same Reynolds number. The proper universal functions will be developed in later chapters on the basis of the experimental results.

Figure V.1 shows the variation of shock extent [$\Delta x(.8)$ to be specific] with initial pressure. Figure V.2 shows the tilt of the shock at the centerline of the tube which arises in the transverse wave regime as the axial symmetry is lost. This loss of axial symmetry and resultant tilt is due to asymmetrical disturbances at the diaphragm, either natural or induced.

The succeeding two figures, V.3 and V.4, show typical natural shock shapes at representative initial pressures within the transverse wave regime.

VARIATION OF SHOCK EXTENT WITH INITIAL PRESSURE
 IN TRANSVERSE WAVE REGIME (ARGON)
 (CONTINUATION OF FIGS. IV.2 & III.4)

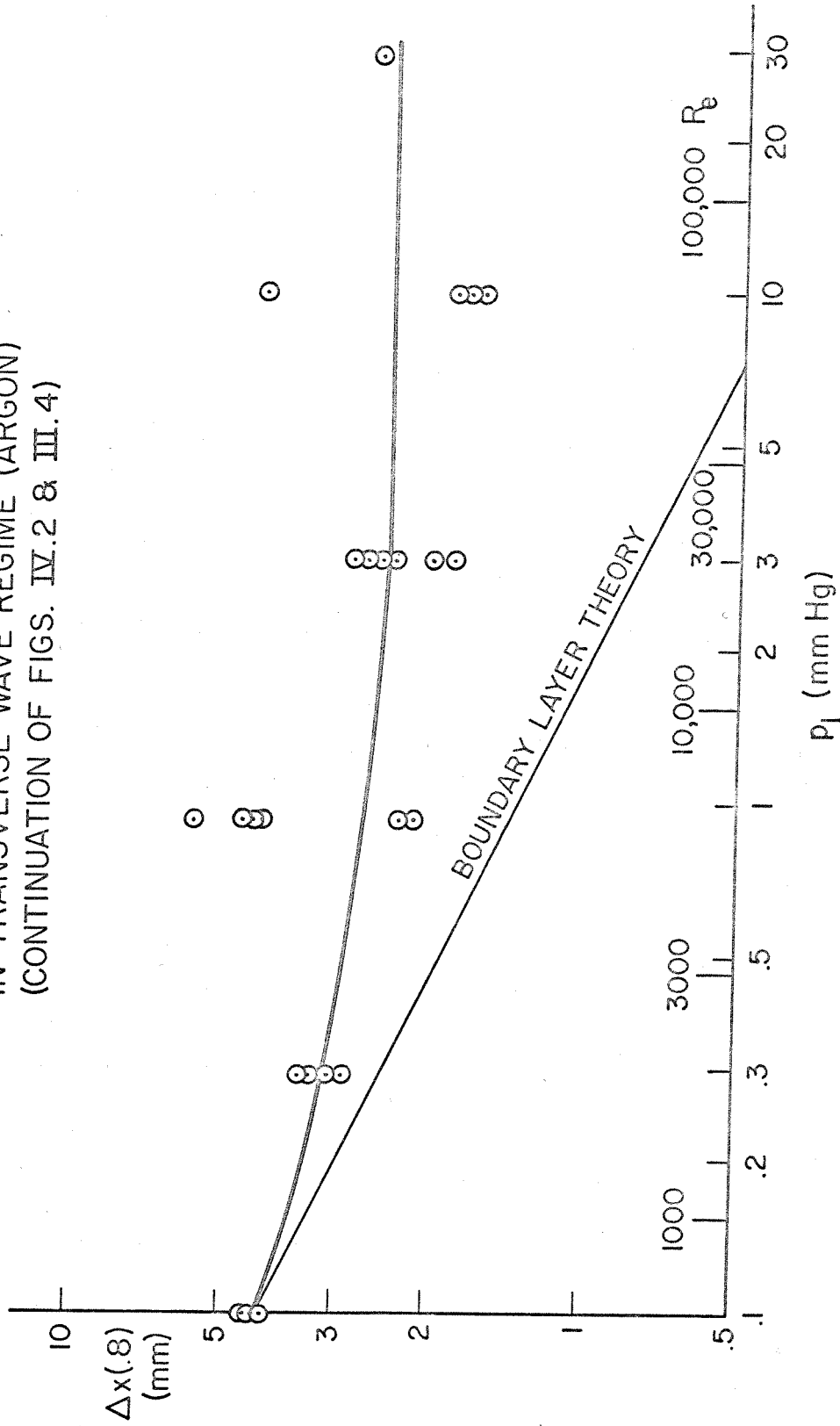


FIG. V.1

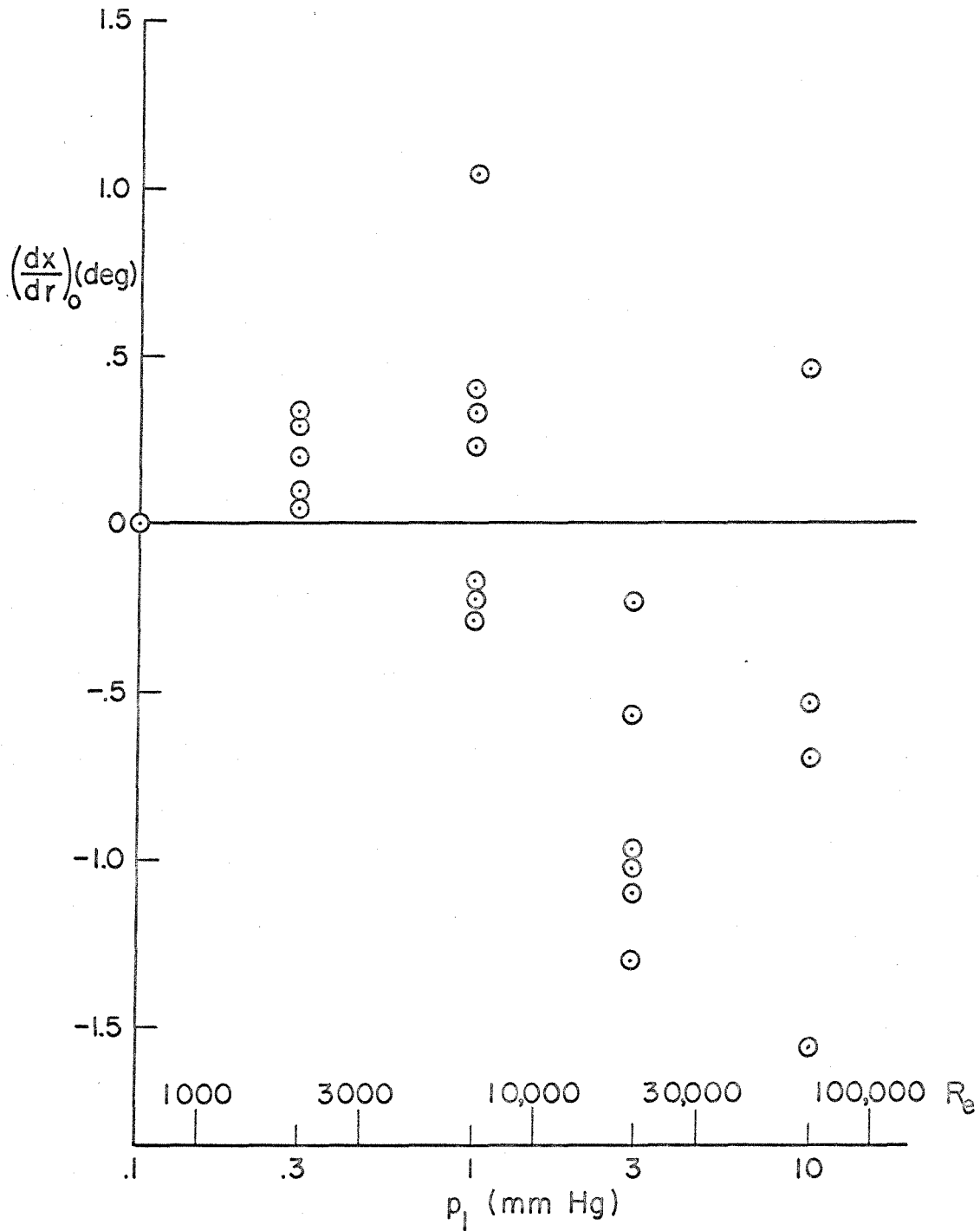


FIG. V.2

"TILT" OR SLOPE OF SHOCK AT CENTER
OF TUBE vs INITIAL PRESSURE

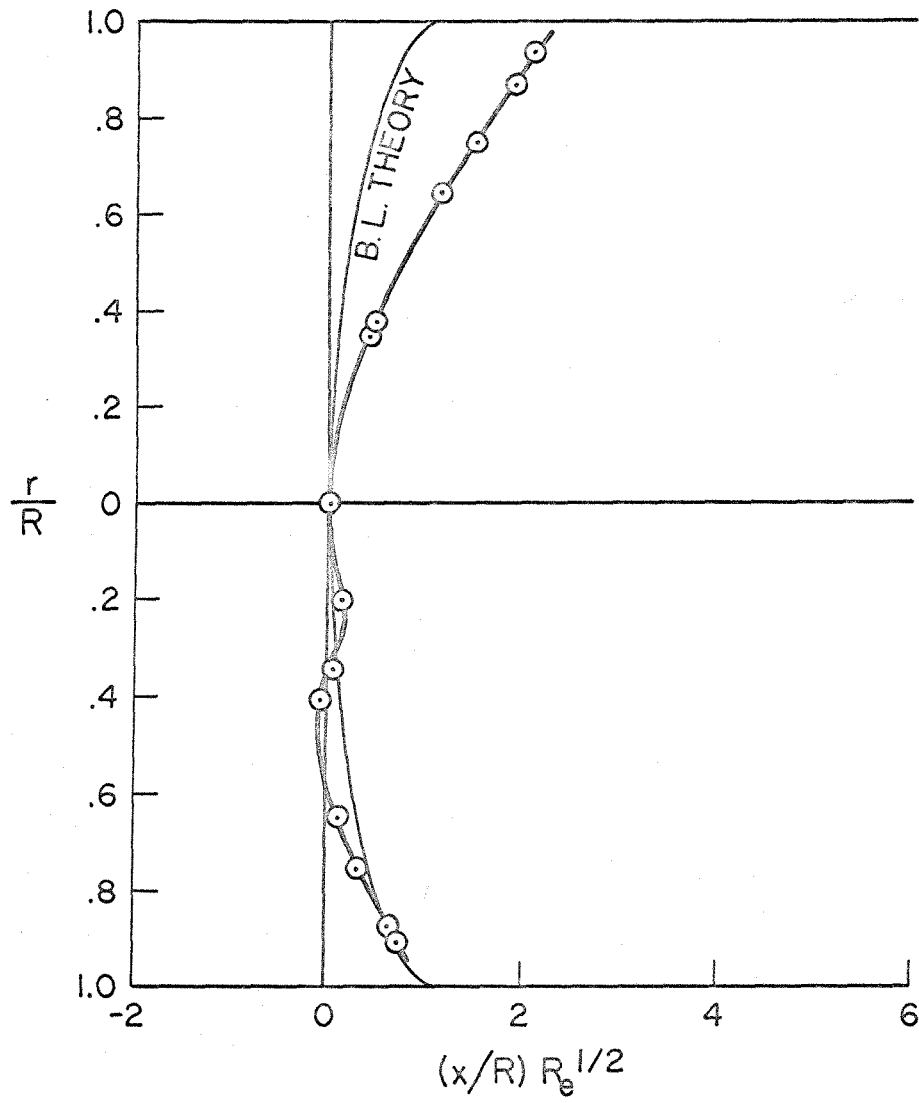


FIG. V.3
 TYPICAL SHOCK SHAPE AT $P_1 = 1$ mm Hg
 (ARGON, $R_e = 6480$)

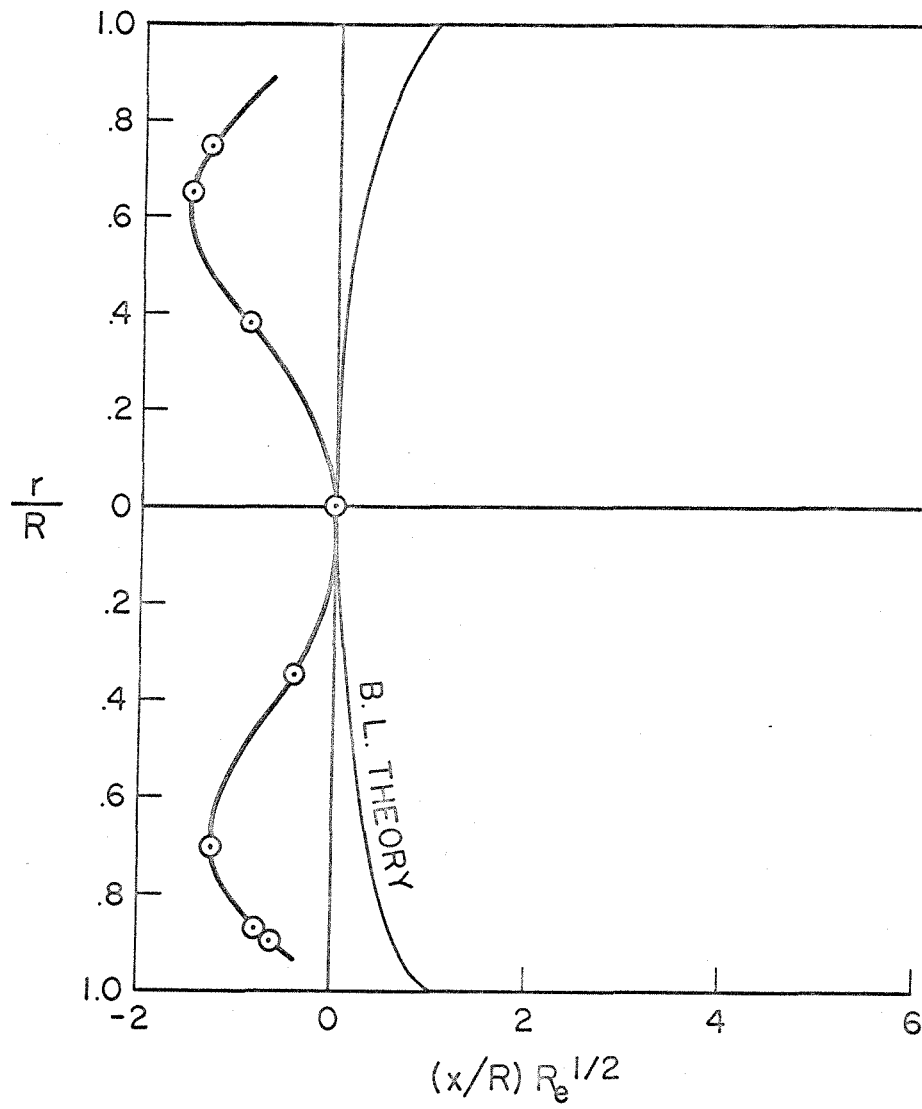


FIG. V. 4

TYPICAL SHOCK SHAPE AT $P_1 = 3$ mm Hg
(ARGON, $Re = 19,450$)

V.2 Partial Diaphragm Experiments

The shock shapes recorded in the experiments reported in the last section were unexplainable in terms of the boundary layer. Since there were no windows, protrusions, or irregularities in the shock tube, the search for a source of disturbance narrowed to the contact surface and the diaphragm. It seemed reasonable that if the diaphragm opening time was responsible for the deviation from boundary layer theory and if the small asymmetry in this opening process caused the asymmetry of the shock, then it should be possible to produce shocks with much greater asymmetry by artificially inducing greater asymmetry in the diaphragm opening and thus in the shock formation process.

This artificial asymmetry was achieved by blocking off part of the diaphragm section by stretching sheet metal, many times thicker than the diaphragm, between the knife blades, as shown in figure V.5. The ruptured diaphragm which results from this technique is shown in figure V.6. The decreased cross-sectional area of the diaphragm section and the increased bursting pressure resulting from the technique offset one another to produce the same Mach number (within a few percent) shock as is produced with the normal full diaphragm. The resultant shock shape is shown in figures V.7 and V.8. A marked and repeatable effect was achieved. The scatter in the shock shapes using the partial diaphragm technique was, in fact, no larger than that for the full diaphragm shots. This seems to be the first experimental proof that disturbances caused by the diaphragm

bursting configuration continue downstream for many diameters (48 in this case), far past the classical "shock formation distance". It can also be noted that a steady state explanation of the shock shapes based on a non-planar contact surface being the driving piston is not in agreement with observation. In the partial diaphragm shot of figure V.7, for example, since the top part of the diaphragm section was blocked, one would expect the contact surface and initial shock shape to bulge forward more at the bottom of the tube than at the top. If this were a steady (in shock-fixed coordinates) effect, this shape should persist, qualitatively at least, down the tube. The actual shape, however, is just the opposite, bulging forward more at the top part of the tube, suggesting that the shape is due to non-steady disturbances which reflect across the tube causing the shock shape to oscillate.

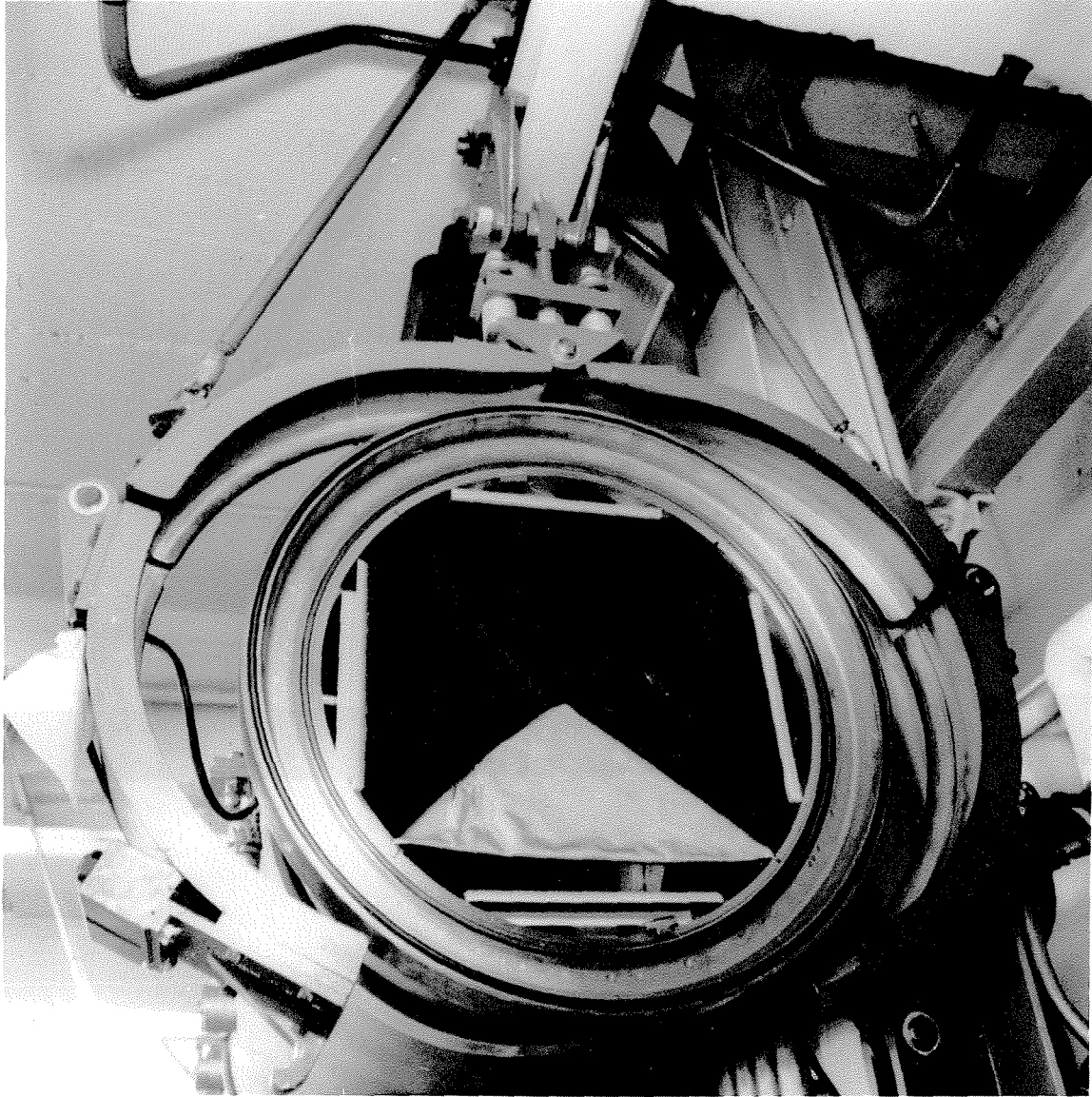


FIG. V.5

PARTIAL DIAPHRAGM EXPERIMENT: BLOCKING TECHNIQUE



FIG. V.6

PARTIAL DIAPHRAGM EXPERIMENT: RUPTURED DIAPHRAGM

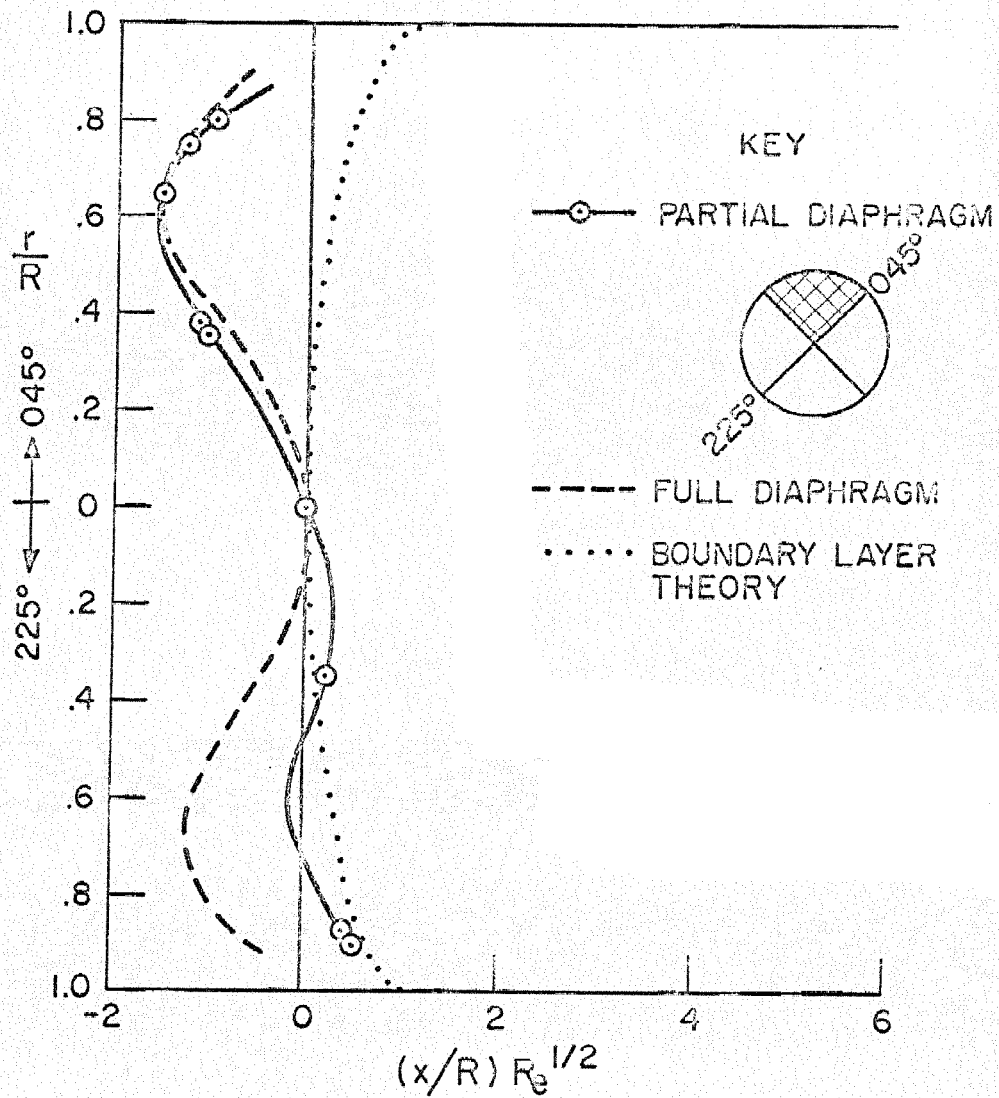


FIG. V. 7

EFFECT OF PARTIAL DIAPHRAGM AT $p_1 = 3$ mmHg,
 (ARGON, $M = 4.71$ $Re = 19,450$)

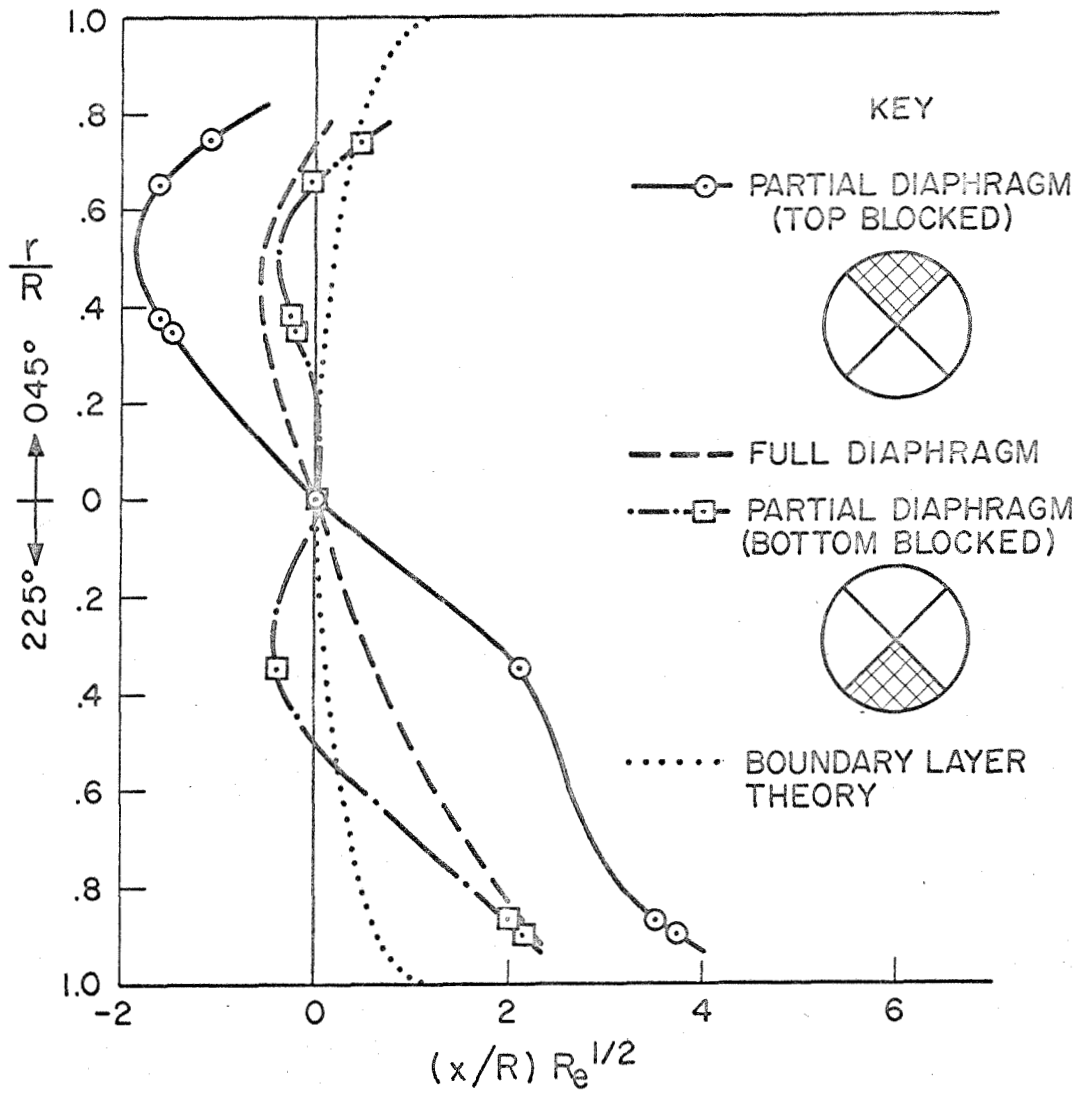


FIG. V.8

EFFECT OF PARTIAL DIAPHRAGM AT
 $p_1 = 10 \text{ mmHg}$, (ARGON, $M = 3.5$ $Re = 64,800$)

V.3 Effect of Blade Shape

In the GALCIT 17" shock tube, the diaphragm is ruptured automatically when the pressure difference across the diaphragm forces it against a set of crossed knife blades. This arrangement, first reported by Roshko & Baganoff (Ref. 18) and later by Liepmann, Roshko, Coles, and Sturtevant (Ref. 19), has been modified and improved since the above descriptions were published. One of these modifications involved providing a set of interchangeable knife blades of various shapes. These blades were designed so that the diaphragm would be in contact with the full length of the cutting edges at the time of burst, rather than just with the center of the blades. With the same diaphragm material and thickness, then, the more deeply curved blades will cause diaphragm rupture at a higher differential pressure.

Since diaphragm disturbances affect the shock shape, it becomes of interest to know if the bursting configuration can be optimized for minimum disturbance. For example, the same driver pressure and hence Mach number can be obtained (other things being identical) by using a flat knife blade and a thick diaphragm or by using a deeply curved knife blade and a thin diaphragm. Since the thicker diaphragm will have the greater opening time, the advantage of the flatter shape at burst initiation tends to be offset and it is not obvious which configuration should result in less disturbance to the shock.

An experiment was performed to answer this question. Blade shapes and diaphragm thicknesses were chosen so as to produce the

same bursting pressure and Mach number, fired into the same test gas. The counter readings which are converted into shock speed and Mach number were identical for the two cases, thus the Mach numbers were identical to within 1/2 of one percent. The resulting shock shapes are shown in figure V.9.

The unsteady nature of the shock shapes limits the quantitative significance of the results. Still, there seems to be a definite indication that the flat blades with the thicker diaphragm produce a more nearly plane shock. If this is true, then one can envision the possibility of reducing the deviation from planarity still further by forcing the diaphragm to burst with a reverse (toward the driver) bulge, thus partially compensating for the opening time. This would involve pre-straining the diaphragm with the blades removed, then turning it around and using a set of blades with reversed curvature (convex). See chapter IX for additional discussion.

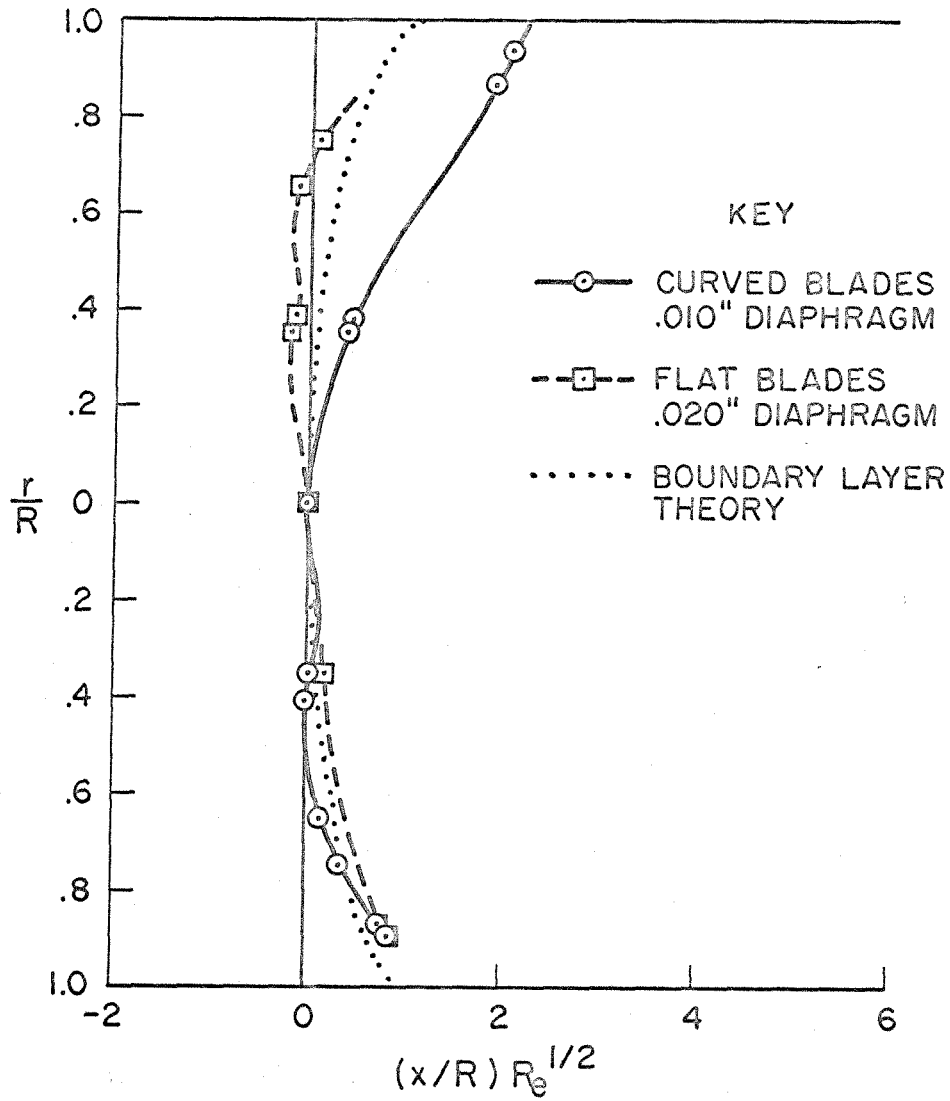


FIG. V.9

EFFECT OF KNIFE BLADE SHAPE AT $p_1 = 1 \text{ mm Hg}$,
 (ARGON, $M = 5.63$ $Re = 6,480$)

V.4 Effect of Driver/Test Section Area Ratio

The low pressure shock tube being a very new instrument, it is natural and healthy that there are differences of opinion about its optimum design. One of the most obvious differences concerns the relative cross-sectional area of the driver and test sections. Small drivers opening into much larger test sections introduce transverse disturbances to the shock wave geometrically. Large drivers (like the GALCIT 17" driver, whose cross section is identical to that of the test section) introduce similar disturbances through their much larger opening times.

An experiment was performed to compare the shock shapes produced by the two types under the same flow conditions (Mach number and Reynolds number or initial pressure). In order to simulate the small driver, a shield with a small (3.5" diameter) central opening was placed between the diaphragm and the knife blades. Since an area reduction at the diaphragm greatly reduces the shock Mach number obtained at a given driver pressure and composition, it was necessary to adjust these parameters to obtain the same M at the same p_1 for both driver configurations. By using a higher driver pressure with the small driver and diluting the helium with nitrogen in the large driver, the difference between the Mach numbers obtained was kept to less than one percent.

The resulting shock shapes are plotted in figure V.10. The similarity between them is striking. Not only is the overall amplitude of the disturbance exactly the same for the two shocks, but the

character and general shape of the two is identical. There is a very slight phase shift which is not much larger than is occasionally observed between two shocks produced under identical conditions.

Because the magnitude of the disturbances are the same we can conclude that there is little to choose, so far as shock planarity is concerned, between a small driver and a large one with curved blades. We have seen, however, that it may be possible to substantially reduce the disturbances in the large-driver tube by changing the diaphragm-blade geometry. Moreover, we may gain some insight as to how this may be accomplished more practically and effectively by an unexpected and more significant conclusion which can be drawn from the results of this experiment.

Because the character of the disturbances are the same we can conclude that it is possible to consider the shock produced by a real diaphragm to be equivalent to a shock produced by an ideal diaphragm with an area constriction just downstream of the diaphragm. This apparent equivalence suggests undertaking a detailed investigation of the disturbance produced in an initially plane shock by an area constriction of known amplitude. If one could determine the nature and decay rate of such a disturbance and learn how to cancel it out, then one could intelligently tackle the problem of eliminating the transverse waves caused in a shock tube by a real diaphragm. Moreover, it is hoped that such knowledge would enable one to predict under what conditions and to what extent transverse

wave disturbances will exist in any given shock tube, i.e. determine the factors which govern the extent of the transverse wave regime. Such an investigation is the subject of chapter VI.

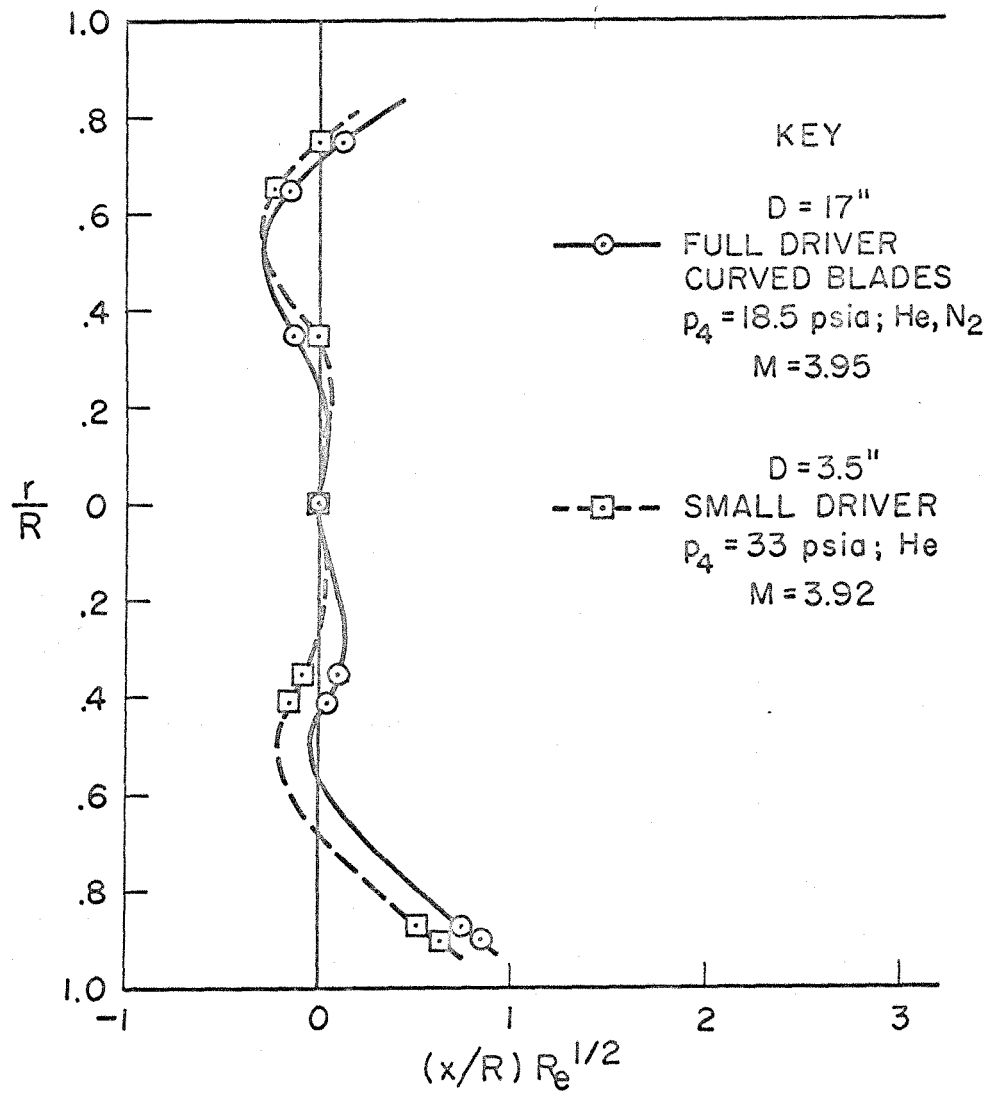


FIG. V.10

EFFECT OF DRIVER / TEST SECTION
 AREA RATIO AT $p_1 = 1$ mmHg,
 (ARGON, $M = 3.9$ $Re = 6,480$)

V.5 Superposition of Viscous and Non-Viscous Effects

If one examines the shock shapes of, for example, figures V.8 and V.9, the following fact may be noted: No matter what wild variations in the shock shape are produced by different diaphragm configurations, the angle at which the shock approaches the wall appears to be the same for all shocks at a given initial pressure. Moreover, this angle is approximately that which, on the basis of the previous experiments in the boundary layer regime, might be expected from the boundary layer effect alone. This empirical observation suggests the assumption that the shock shape near the wall is governed by the viscous boundary layer and is independent of disturbances intersecting the shock away from the wall.

Since the angle at which a shock deviates from a plane is always very small throughout the transverse wave regime, it should be possible to consider the shock shape to be caused by a linear superposition of the deviations due to the boundary layer and those due to transverse waves. From the results of the experiments in the boundary layer regime it is clear that the deviations not too close to the wall due to the boundary layer are given quite accurately by the theory above $p_1 \approx 100\mu$ Hg. Thus if one subtracts this deviation due to the boundary layer from the experimental shock shape the resulting adjusted shock shape should be that which is due solely to the transverse disturbances.

The conclusions of the preceding two paragraphs lead to the reasonable expectation that such adjusted shock shapes should all

intersect the walls at right angles. This expectation seems to be supported by the experiments. The use of this superposition principle greatly clarifies the nature of the transverse wave disturbances by eliminating the viscous effects from the shock shape.

When normal wall intersection is applied as a boundary condition to the adjusted shock shapes the results bear a striking resemblance to the shapes recorded optically by Lapworth (Ref. 11) for an initially plane shock* perturbed by a rooftop or area constriction disturbance. This fact lends further weight to the conclusion reached in section V.4 regarding the nature of the diaphragm disturbance in a shock tube.

In the next section both "raw" and adjusted shock shapes will be presented. The results of the experiments reported in chapter VI, however, will be given entirely in the form of adjusted shock shapes.

*Lapworth's experiments were performed at sufficiently high initial pressures that viscous effects were negligible compared to the large scale disturbances induced.

V.6 Effect of Mach Number: Phase Shift

The experiments reported in the first five sections of this chapter were all conducted at constant Mach number. To determine the effect of Mach number on the shock shape an experiment was conducted in which the Mach number was varied by changing the composition of the driver gas, all other parameters remaining constant. The results of the first such experiment are plotted in figure V.11.

The gross magnitude of the deviation from a plane is the same at both Mach numbers. If we assume the shock shape to be oscillating as transverse waves reflect back and forth across the tube, then the change in Mach number appears to have caused a phase shift. These results are not surprising. Since the diaphragm configuration, blades, material, and differential pressure were all identical, then the geometry of the bursting diaphragms and thus the disturbance inherent in the shock formations should also be the same. The change in Mach number changes the speed at which the transverse waves cross the tube as well as the forward speed of the shock. These effects, while partially compensating, do not cancel completely and there is a net change in the wavelength of the disturbance. The "wavelength" of the disturbance is defined as the number of tube radii which the shock travels while the transverse waves make a round trip across the tube and back to their original position. If the disturbance is completely symmetric, then the shock shape will repeat its cycle twice during one of these wavelengths. If, however,

there are asymmetric components in the disturbance, as are evident in figure V.11 at $p_1 = 1$ mm Hg, then the shock will travel a complete wavelength before repeating its shapes.

The fact that the magnitude of the disturbance is approximately (at least) independent of Mach number means that the decay of the disturbances as they travel down the tube is either small or nearly independent of Mach number.

Since, to this point, the oscillatory nature of the disturbances had been only an assumption, it was deemed necessary to carry out a more detailed experiment to show the slow shift in shock shape as the Mach number is changed in small increments. Accordingly, a series of 14 shots were fired at various Mach numbers, all other conditions being the same. The resulting shapes, plotted in figure V.12, show clearly a slow, gradual phase shift in the disturbance with M . Note that these are "adjusted" shock shapes, that is the curvature due to the boundary layer has been subtracted out from the raw data. The spacing between the shock shapes in figure V.12 (which were all measured at the same tube length) is conceptual, and represents the change in "effective tube length", measured in transverse disturbance wavelengths, which occurs when the Mach number is changed.

The results of this experiment can be considered as sufficient proof of the periodic nature of shock shape disturbances due to the diaphragm opening and other tube-fixed sources. Thus is justified the use of the name "transverse wave regime".

The experiments reported in the next chapter probe more deeply into the nature and decay of these transverse waves and seek to answer the riddle of why such waves are not apparent at all initial pressures.

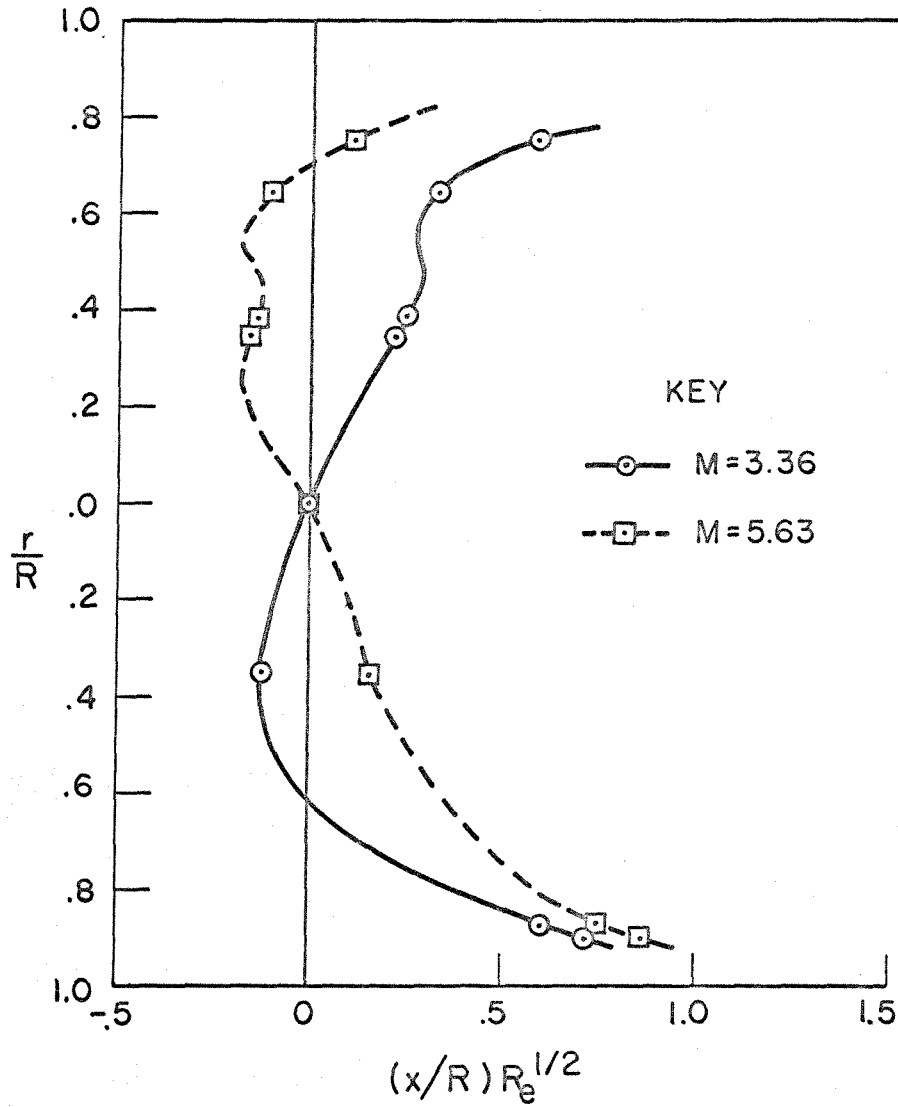


FIG. V.11

EFFECT OF MACH NUMBER AT
 $p_1 = 1$ mm Hg, ARGON, FLAT BLADES
 p_4 CONSTANT @ 27.5 psia
 (M CONTROLLED BY He - N₂ DILUTION)
 ($Re = 6,480$)

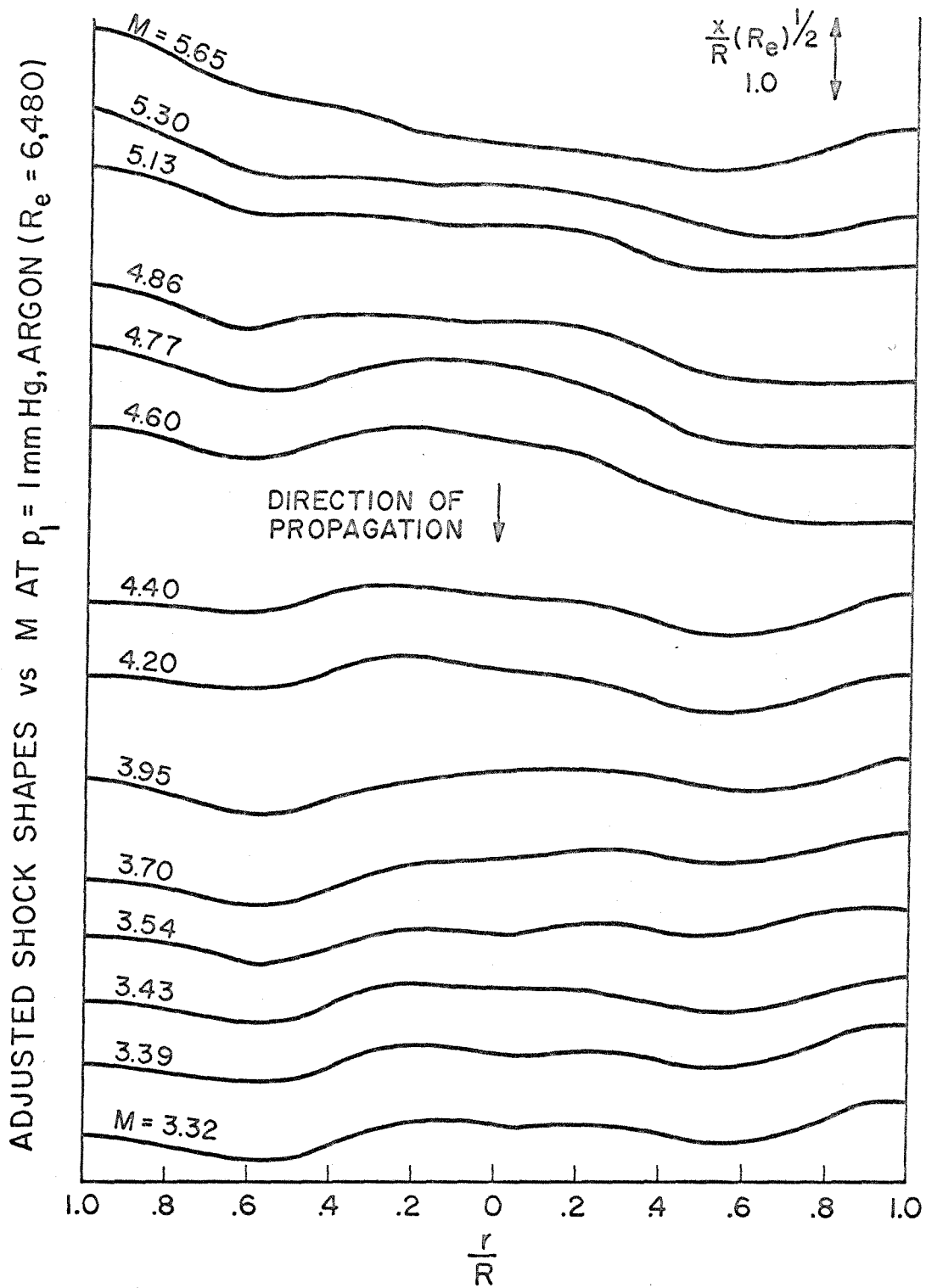


FIG. V.12

VI. TRANSVERSE WAVE REGIME: "ROOFTOP EXPERIMENTS"

VI.1 The Riddle of Pressure-Dependent Disturbances

The experiments of the previous chapter proved that disturbances to the shock shape due to diaphragm opening do exist, propagating downstream in the form of transverse waves, reflecting across the tube with some M-dependent wavelength. On the basis of these experiments alone, one would be tempted to predict that the shock shape deviations so caused should exist at all initial pressures with about the same gross magnitude, and that these deviations can be ignored only when the initial pressure is so low that the curvature due to the boundary layer is large in comparison with these deviations. One finds, however, that such a prediction is resoundingly contradicted by experimental fact.

Such a prediction would require that the adjusted shock shape have about the same gross deviation from a plane at all pressures. In contrast to this, the actual deviations are of about the same magnitude for pressures within the transverse wave regime, but at about $p_1 = 1$ mm Hg the magnitude of these deviations falls rapidly as the pressure is lowered, till at about $p_1 = .1$ mm Hg (100 μ Hg) the deviations are almost totally absent. Certainly, between these two pressures, while the thickness of the boundary layer is changing by a factor of about three, the mean deviation from a plane of the adjusted shock shape is changing by several orders of magnitude. At

even lower pressures the deviations remain very small, but never vanish entirely.

Granted, then, that these are the experimental facts, two main questions remain to be answered:

- (1) Why are these transverse wave disturbances not pressure-independent? What causes the observed dependence?
- (2) What determines the initial pressure at which the transition between the transverse wave and boundary layer regimes occurs in any given shock tube?

The answer to the second question can obviously be found only through knowledge of the answer to the first (unless one resorts to the unwieldy empirical approach of doing experiments such as these in a great number of shock tubes). Thus it is the first question to which an answer will next be sought.

VI.2 Possible Causes of the Pressure Dependence

The fact that the deviations from planarity of the shock shape (adjusted) are much smaller at low pressures than at high pressures can be explained by any one or more of the following possibilities.

Either

- (1) The same diaphragm configuration somehow produces weaker transverse waves at low pressures,
- (2) The same transverse waves produce smaller changes in the shock shape at low pressures, or
- (3) The decay of the transverse waves is greater at low pressures.

The first of these possibilities is listed for completeness although its existence seems much more remote than the other two. Since the pressure difference across the diaphragm is very nearly the same at all p_1 , then the opening time should be constant and so should the shape of the initial compression waves which form the shock. Since the strength of the main shock is held constant, it is difficult to conceive of the transverse waves being otherwise. (The experiments of this chapter show that the transverse waves are initially of constant strength, as one would expect.)

The second possibility is not so easily disposed of. It is possible to conceive of a shock wave as possessing some inherent "stiffness-like" quality which increases with shock thickness and therefore with decreasing initial pressure. The mechanism for such

a quality might be the size of the intersection region of the shock wave and transverse wave. Since each has a finite thickness, their intersection is not a point, but a finite region which increases in size as the waves themselves thicken. Thus, as the pressure is lowered the slope-changing power of the transverse wave is spread out over a larger portion of the shock, smoothing out its effects, and leading to overlapping of compression and expansion regions. There is no doubt that such an effect can exist at extremely low pressures. Whether or not such an effect can be significant at $p_1 = 100\mu$ Hg, where the shock thickness is still a quite small fraction of the tube radius, is, however, a matter to be answered by the experiments. (It will be shown that the experiments answer in the negative: the initial shock shapes produced by identical disturbances at 100μ Hg and at 3 mm Hg are identical and therefore this possible effect cannot explain the observed pressure dependence.)

The third and final possibility is that the decay of the transverse waves is greater at low pressure. From an inviscid point of view, there is no basis in theory for such an effect. The shock stability theories of both Freeman (Ref. 10) and Whitham (Ref. 20) result in predicted disturbance decays which are independent of initial pressure.

In these inviscid theories, however, the transverse waves are reflecting off rigid walls, while in reality they are reflecting off boundary layers. Thus an attractive explanation for the

pressure dependent decay is based on the gradual growth in the boundary layer as the pressure is lowered. The change in the decay rate, however, is not a gradual thing, but is nearly discontinuous, occurring in the GALCIT tube at about $p_1 = 300\mu$ Hg. Thus several difficulties and uncertainties remain unresolved by speculation. To resolve these and hopefully solve the riddle of the pressure dependent disturbances an exhaustive series of experiments were performed wherein initially plane shocks at the same M but at pressures both above and below the transition region of 300μ Hg were perturbed by identical disturbance sources and the resulting shock shapes observed over the length of the tube. These experiments and their results are described in the next sections.

VI.3 The Axisymmetric Rooftop Disturbance Experiment

The eventual goal of the axisymmetric rooftop (see Fig. VI.1) disturbance experiment is, of course, to answer the questions raised in the last sections. To this end, the immediate objective of the experiment is the comparison of the shock shapes produced by the same disturbances at $p_1 = 3 \text{ mm Hg}$ (well within the transverse wave regime) and at $p_1 = 100\mu \text{ Hg}$ (in the heart of the boundary layer regime). In order to obtain this objective, the experiment must satisfy the following requirements:

- (1) Prior to reaching the disturbance, the shocks must be effectively plane. This requires that the disturbance be located far enough downstream of the diaphragm so that the diaphragm disturbances have at least begun to decay and the shock is well formed, if not plane, and that the rooftop disturbance be large enough so that it produces shape deviations much larger than those remaining due to the diaphragm. This requirement was satisfied by placing the disturbance approximately 22 diameters downstream of the diaphragm and using a disturbance which blocked off about 58% of the cross-sectional area of the tube.
- (2) The undisturbed Mach numbers of the shocks must be the same for both initial pressures and held constant throughout the experiment. This requirement was satisfied by performing all the 3 mm experiments with a pure helium driver and all the 100 μ experiments with a driver mixture

containing 45.0% nitrogen and 55.0% helium. The diaphragm configuration and driver total pressure were the same for all the runs and the Mach number was recorded for each run. Variations in M were usually less than one percent.

- (3) The results must be independent of the curvature due to the boundary layer. This requirement was satisfied by using adjusted shock shapes, the shape given by boundary layer theory being subtracted from all data.
- (4) The disturbance must be simple enough to produce a distinct set of transverse waves causing a simple, regular, periodic fluctuation of the shock shape, qualitatively similar to that produced by the diaphragm disturbance. This requirement was satisfied by the axisymmetric rooftop disturbance shown in figure VI.1 and alternatively describable as a "doughnut with a triangular cross section".
- (5) The data points downstream of the disturbance must be such as to reveal the nature of the shock shapes, the wavelength of their periodicity, and the amplitude of each peak during the decay process. This requirement was satisfied by allowing the distance between the disturbance and the end plate where the shape was recorded to be controllable in 1 inch increments from zero to 451".

Figure VI.2 is a schematic diagram of the experimental setup.

CUTAWAY VIEW OF
AXISYMMETRIC ROOFTOP DISTURBANCE

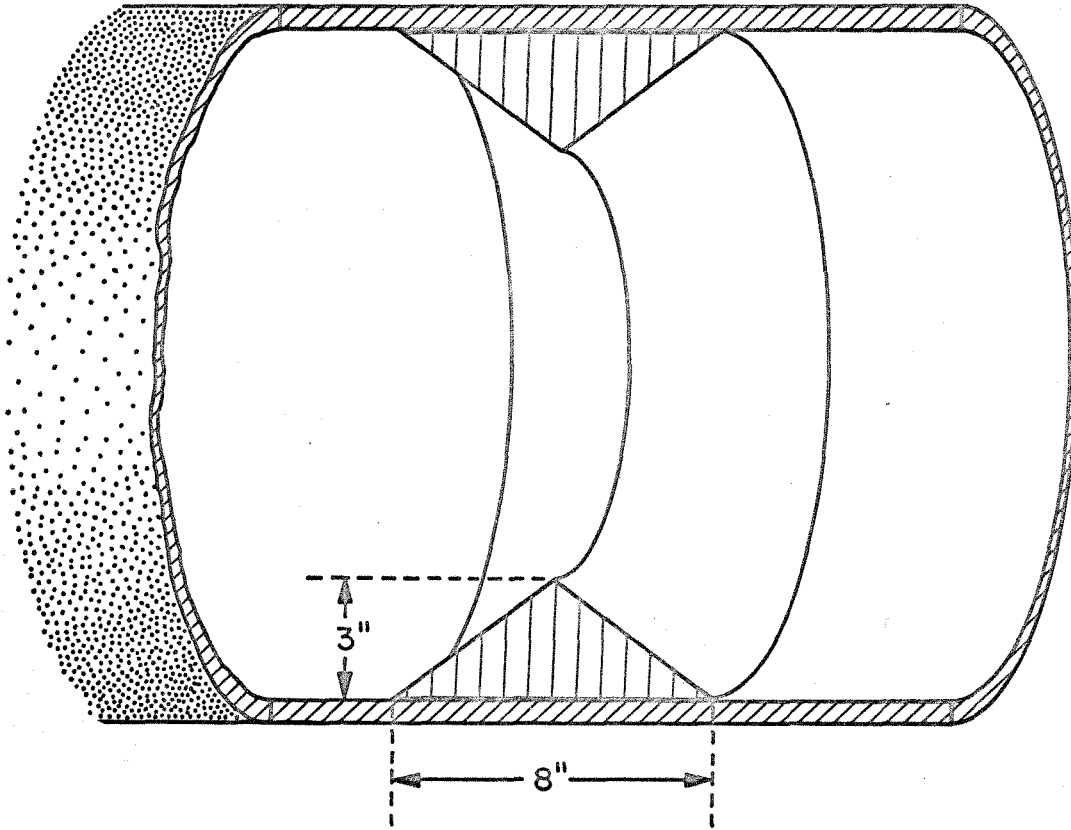


FIG. VI .1

EXPERIMENT SCHEMATIC

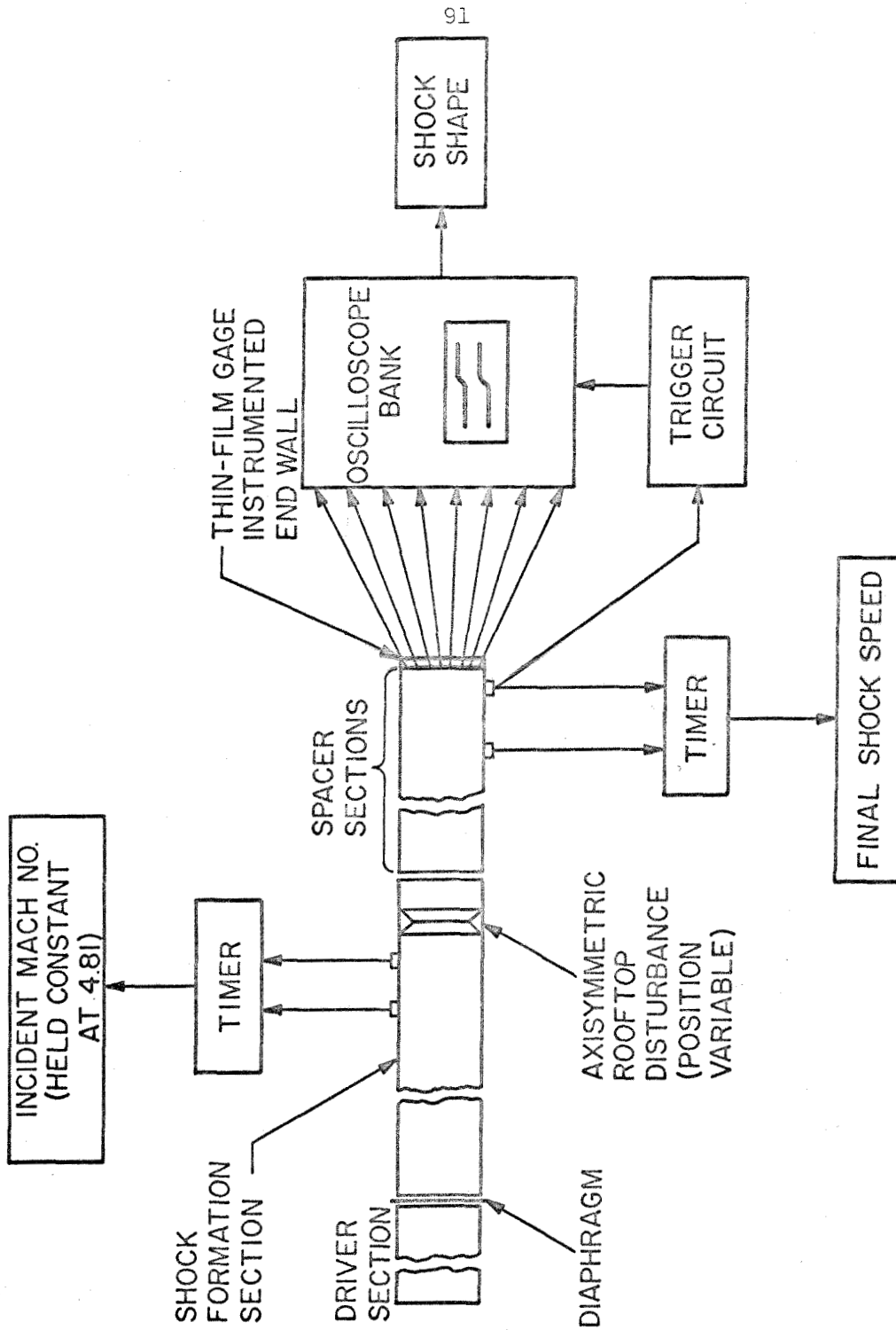


FIG. VI. 2

VI.4 Results of the "Rooftop" Experiment

The first major result of the experiment was that the shock shapes immediately downstream of the disturbance were independent of initial pressure. This finding rules out the first two possible causes of the pressure dependence set forth in section VI.2. Since the shock shapes at 100 μ and at 3 mm are identical initially (see Fig. VI.3) and are known to be vastly different at the end of the tube (this was confirmed with the rooftop disturbance), then there must be some great difference in their rates of decay.

A second result was that the shock shapes produced by the axisymmetric disturbance are qualitatively very similar to those produced by a two-dimensional rooftop in the experiments of Lapworth. Compare, for example, figure VI.3 with figure 6 of reference 11.

A rooftop disturbance does not produce a single compressive transverse wave, but a complex system containing two compressions and a rarefaction. The effect of the rarefaction is, however, spread out and soon disappears and for a particular rooftop length the second compression coincides with and reinforces the first from the opposite wall. This condition was approximated in Lapworth's experiments. In the axisymmetric rooftop experiment, although no attempt was made to satisfy such a reinforcement condition, the very complex shock shapes which would correspond to a complex wave system were not observed. Whether the apparent existence of but a single compressive transverse wave was due to a fortuitous combination of Mach number and geometry, the effect of the focusing at the center

of the tube, the separation of the flow on the downstream side of the disturbance, or some other cause is not known. Nevertheless, because the observed shock shapes are explainable in terms of a single compressive transverse wave, this idealization of the transverse wave system will be used throughout this and the following chapters.

A third result was that the shock shapes were indeed regularly periodic, "oil-canning" back and forth with a constant wavelength of about three tube radii. Since the disturbance and shock shapes are completely axisymmetric, this wavelength corresponds to the distance required for the transverse waves to cross the tube once. A distinction must really be made between the transverse waves and the trace of their intersection with the main shock. This intersection trace (which Whitham calls a shock-shock) is what controls the periodicity of the shock shape. From the experimental value of the wavelength, the angle β which this intersection trace makes with the walls of the tube can be calculated.

$$\beta = \tan^{-1} \frac{2R}{3.05R} = \tan^{-1} .656 = 33.3^\circ \quad (\text{Eqn. 6.1})$$

This result leads in turn to an estimate of the strength of the transverse wave. Figure VI.4 shows the geometric relationship between the shock, the transverse wave, and the intersection trace. It can be seen that the angle β is a function of M_w , the strength of the transverse wave. All the other parameters are fixed, M_t being the Mach number of the main transmitted shock wave after it

has interacted with the disturbance source. This is somewhat less than M , the strength of the incident shock. M_2' is the Mach number of the flow behind the shock relative to the walls of the tube.

The following relationships are obvious:

$$\Psi = \cos^{-1} \frac{M_t \frac{a_1}{a_2} - M_2'}{M_w} \quad (\text{Eqn. 6.2})$$

and

$$Y = M_w \sin \Psi \quad (\text{Eqn. 6.3})$$

and

$$\beta = \tan^{-1} \frac{Y a_2}{M_t a_1} \quad (\text{Eqn. 6.4})$$

In the rooftop experiment $M = 4.81$, $M_t = 4.48$, $M_2' = 1.196$, $a_2/a_1 = 2.68$. If the transverse wave were a Mach wave ($M_w = 1$) then the above equations would give $\Psi = 61.6^\circ$, $Y = .880$, and $\beta = 27.8^\circ$. However, if $M_w = 1.2$ then

$$\Psi = 66.6^\circ$$

$$Y = 1.10$$

$$\beta = 33.3^\circ$$

which agrees with the experimentally observed value based on the wavelength of the shock shape. Of course the strength of the transverse wave decays somewhat as it moves down the tube and its

strength also varies within each period, increasing as it is focused near the center of the tube. Nonetheless we may conclude that the mean value of the strength of the transverse wave is given approximately by $M_w = 1.2$. It will be seen that this applies to the $p_1 = 3$ mm shock over the entire length of the tube, but to the $p_1 = 100\mu$ shock only for a limited distance downstream of the disturbance.

We are led to yet another result as we note that the strength of the transverse wave is (within the accuracy of the calculation) equal to the flow Mach number M_2' . This means that rather than being swept downstream as in figure VI.4, leaving an oblique shock or Mach wave envelope, the original transverse wave disturbance grows with time but its trailing edge remains stationary at the disturbance as a normal detached shock as shown in figure VI.5. This is just what one should expect, since the rooftop disturbance wedge angle was greater than that which can allow an attached oblique shock at a Mach number M_2' . It is to be expected that if the wedge angle were reduced or M_2' increased (the latter possibility being extremely limited) the geometry would then be as in figure VI.4. It should be noted that figure VI.5, which agrees with all observations of the experiment and satisfies all the boundary conditions of the flow, is basically unaffected by the reflection from the opposite wall. This case is shown in figure VI.6 and can obviously be extended through any number of reflections. Figures VI.4,5,6 are for $M_2' > 1$. The corresponding subsonic case

is similar and will be presented in connection with a discussion of Lapworth's experiment.

The sixth and by far most significant and surprising result concerns the rate of decay of the shock shape deviations caused by the transverse waves. This decay is characterized by the decay constant n which is the exponent of the distance down the tube (or equivalently, the time) in an expression such as

$$A \propto z^{-n}$$

where A is the amplitude of the shock shape deviation. Although Whitham's theory leads to $n = .5$, the most widely accepted value has been $n = 1.5$ predicted theoretically by Freeman and apparently verified experimentally by Lapworth. It turns out that this apparent verification is dependent upon the manner in which the data is analyzed.

The data from the axisymmetric rooftop experiment lead conclusively to a decay constant of $n = 0.50$. This may be seen from figure VI.7. This figure will be discussed in more detail in the next section.

The final result of the experiment leads to the solution of the riddle of pressure-dependent decay. After being almost identical with the 3 mm shock, the shape of the 100 μ shock suddenly at about 13 radii down the tube begins to oscillate with a much smaller wavelength and decay much faster. The details of this process will be discussed in chapter VII.

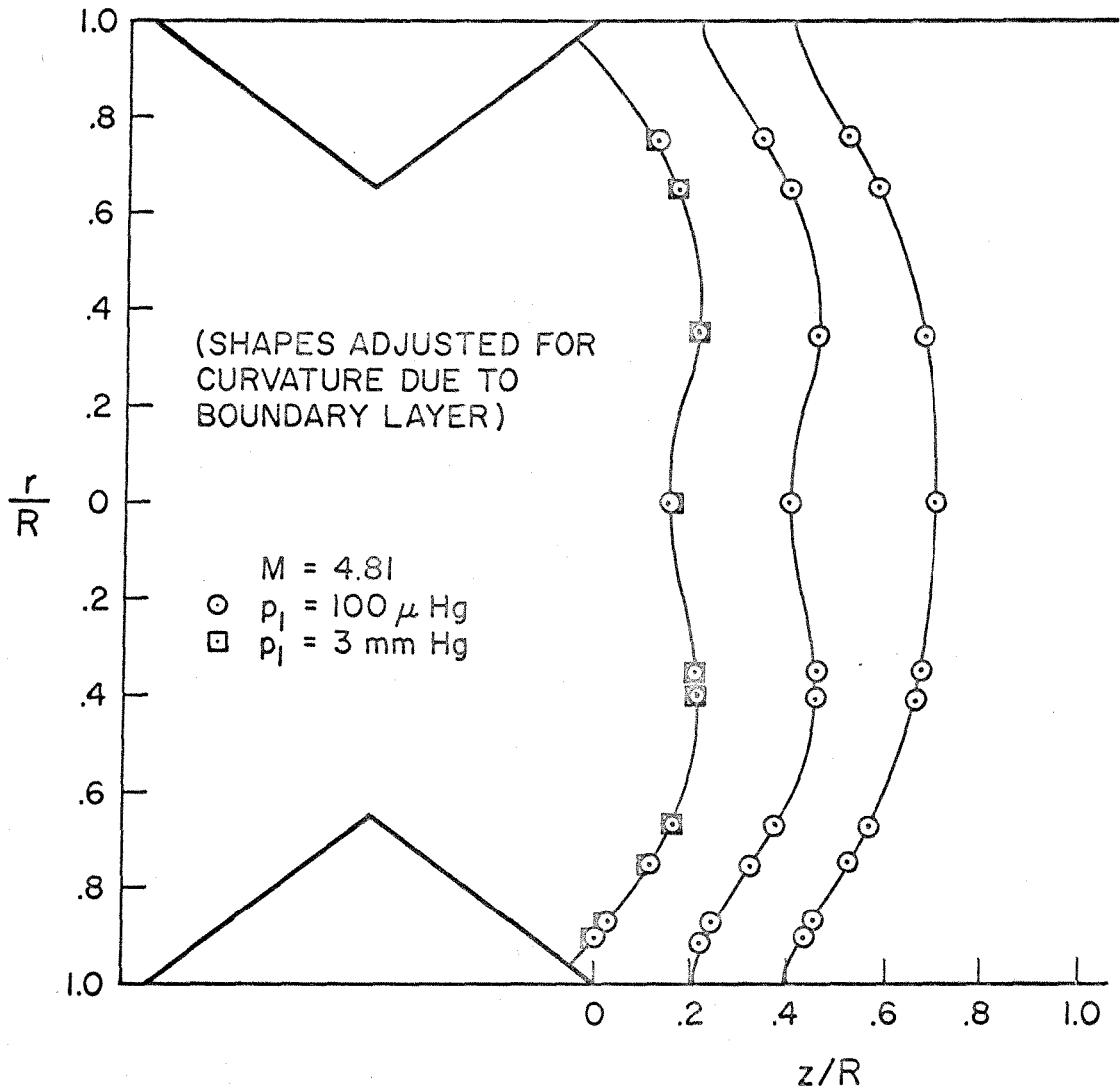
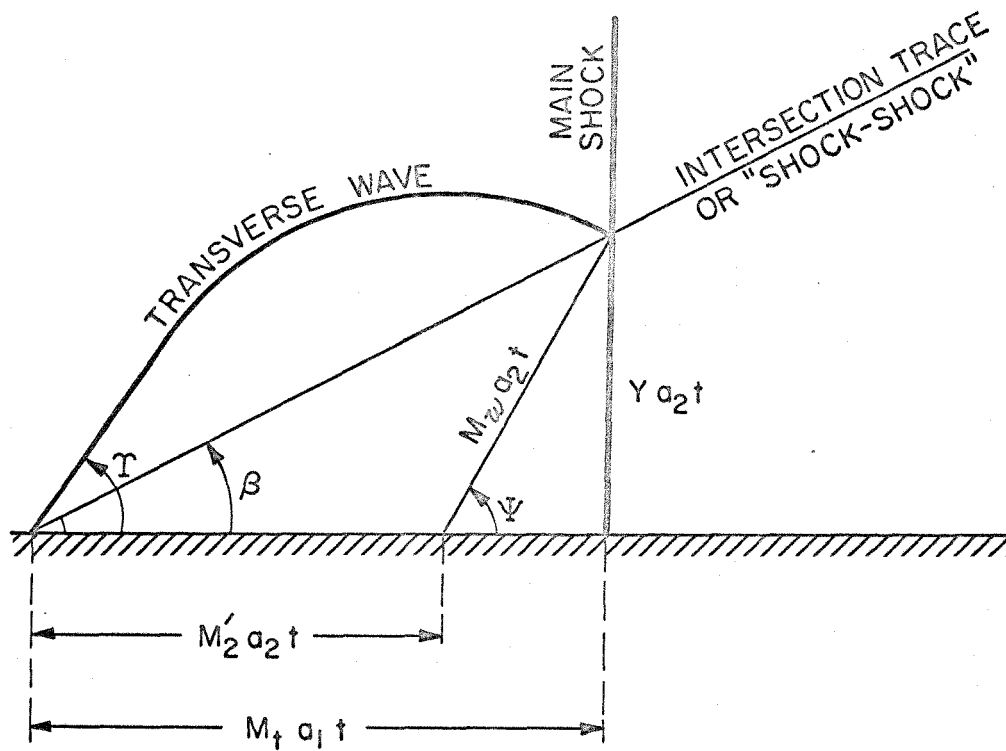


FIG. VI.3
 TRUE SCALE SHOCK SHAPES
 IMMEDIATELY DOWNSTREAM OF
 AXISYMMETRIC ROOFTOP DISTURBANCE



NOTE: IF $M_w = 1$, THEN τ IS THE MACH ANGLE

FIG. VI.4

TRANSVERSE WAVE GEOMETRY FOR
DERIVATION OF EQNS. 6.2-6.4

$$(M_2' > M_w \geq 1)$$

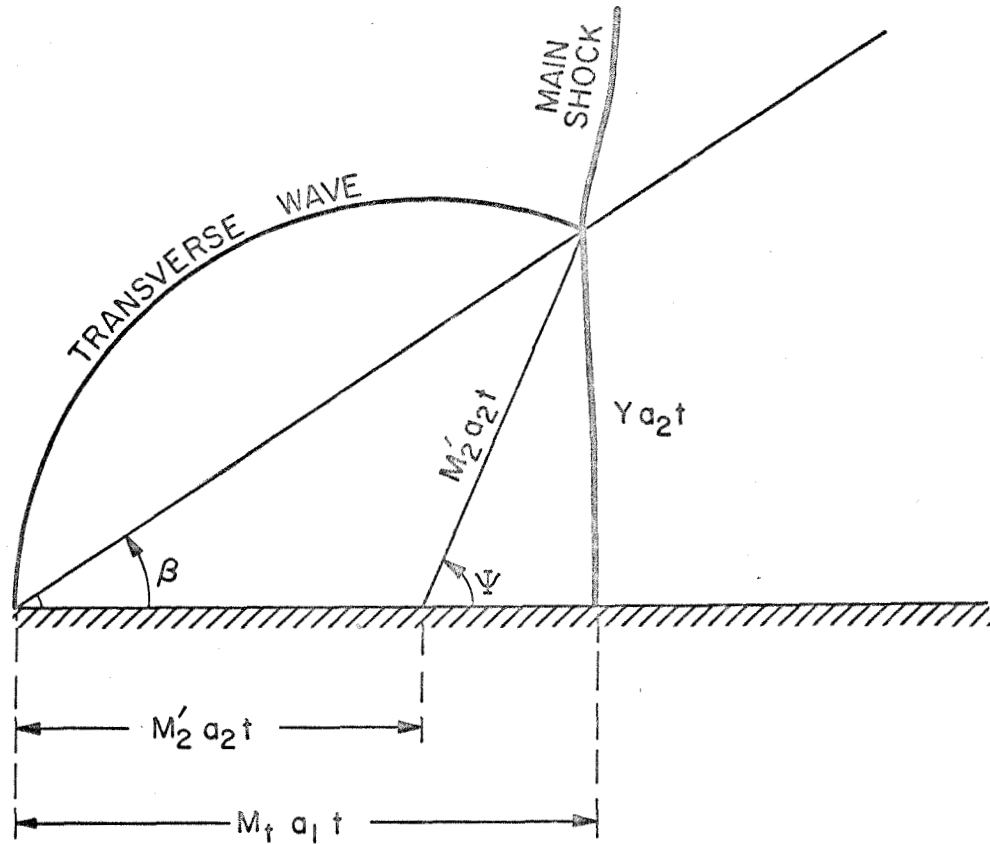


FIG. VI.5

TRANSVERSE WAVE GEOMETRY FOR
 AXISYMMETRIC ROOFTOP EXPERIMENT &
 ALL CASES OF LARGE WEDGE ANGLE

$$(M_w = M_2' > 1)$$

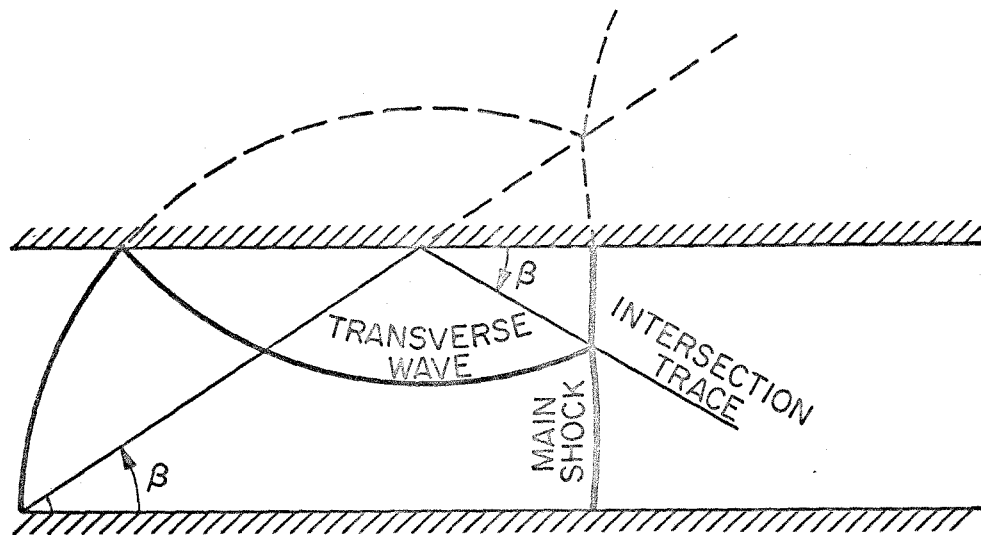


FIG. VI.6

TRANSVERSE WAVE GEOMETRY
AFTER REFLECTION

$$(M_{2'} = M_2' > 1)$$

SHOCK PERTURBATION @ $\zeta/R = .896$ vs DISTANCE TRAVELLED
 DUE TO AXISYMMETRIC ROOFTOP DISTURBANCE

$p_1 = 3 \text{ mm Hg}$ ($R_e = 19,450$), $M = 4.81$

DATA POINTS
 □ (GALCIT 17" SHOCK TUBE)
 ○ EMPIRICALLY CALCULATED MAXIMA & MINIMA

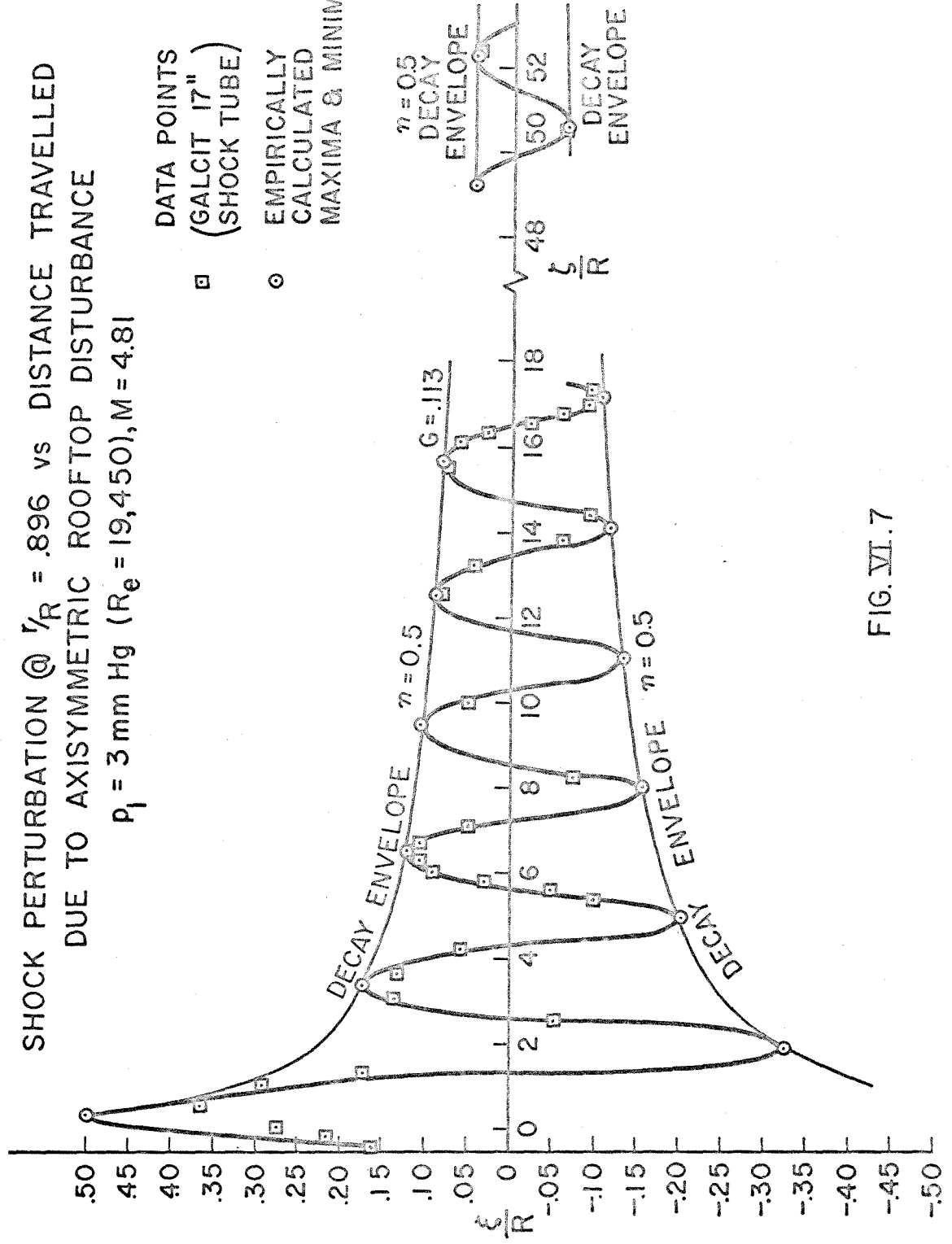


FIG. VI.7

VI.5 Discussion of "Rooftop" Results

In discussing the results of the axisymmetric rooftop experiment, notation has been used which parallels as closely as possible that used by Freeman and Lapworth for the two-dimensional equivalent. Some of the quantities, however, must be redefined in order that the experimental results may be compared with a more realistic theoretical model.

Freeman characterizes the amplitude of the shock disturbance by a quantity ξ which he defines as the "total perturbation", a quantity which is similar to $\Delta x(.8)$ defined in figure IV.4 except that it takes in the entire diameter of the tube. In his theory the shape of the shock wave is always a standing cosine wave whose amplitude is oscillating about zero. Thus the "total perturbation" is synonymous with the horizontal displacement of the shock at the wall from its position at the center in such a theory. This shape, however, does not exist in reality and is inconsistent with the boundary condition that the shock (after boundary layer effects have been subtracted) meet the wall at right angles. The real shock, then, has "higher modes" and never possesses a total perturbation of zero. For this reason, and because the "total perturbation" of a complex shock shape cannot easily be classified as positive or negative, the "total perturbation" so defined is an extremely inconvenient quantity for relating experiment and theory. A more meaningful quantity experimentally (and one just as easily measurable from Lapworth's optical data) is the horizontal (or

axial) displacement of the shock-wall intersection from the shock location at the centerline. This quantity does pass through zero and oscillates in a regular manner as predicted by the theory. The shock shapes resulting from the axisymmetric rooftop experiment were, however, obtained not optically, but from a number of discrete data points sensing arrival of the shock. Thus a quantity, related to the above but requiring no extrapolation, is the simple axial displacement of the shock position at the outermost data point ($r/R = .896$) from its position at the centerline ($r/R = 0$).

Accordingly, ξ is herein redefined to be this quantity after being adjusted by subtracting the boundary layer curvature from each data point. The difference between these two definitions of ξ can be seen more clearly by noting that in figure VI.8b, ξ as herein defined is zero, while according to Freeman's definition it is finite.

The independent variable is the distance down the tube and is denoted by z when measured from the trailing edge of the rooftop disturbance (Freeman uses x) and by ζ when measured from the origin of decay. In Freeman's theory the difference between these two quantities is fixed by the geometry. However, since Freeman's theory is an asymptotic one, invalid near the origin, this difference will herein be left free, to be determined from the experimental data. One other difference in the definition of these variables will be introduced. In Freeman's work ζ is dimensional while z is non-dimensionalized with respect to the diameter. In

this chapter both will be treated as dimensional quantities and the non-dimensionalization will be explicitly indicated in the equations.

Freeman writes the results of his theory in a form which, in the above variables, becomes

$$\frac{\xi}{R} = \frac{2G}{(\zeta/2R)^n} \left| \sin \left(\frac{m\zeta}{2R} + \psi \right) \right| \quad (\text{Eqn. 6.5})$$

where $\zeta = z + 1.776R$ and $n = 1.5$. G , ψ , and m are functions of Mach number. Alternatively, in order to more realistically evaluate the experimental data, it has been found necessary to herein use a function of the following form:

$$\frac{\xi}{R} = \frac{2G}{(\zeta/2R)^n} W \left(\frac{m\zeta}{2R} + \psi \right) \quad (\text{Eqn. 6.6})$$

where $\zeta = z + 2aR$ and n , G , ψ , m , and a are all to be determined by the data. Figure VI.7 is a plot of ξ/R vs. ζ/R for the axisymmetric rooftop experiment and from it the above parameters are determined to be:

$$\begin{aligned} n &= 0.50 \\ G &= .113 \\ \psi &= .747 \\ m &= 4.12 \\ a &= -.25 \end{aligned} \quad (\text{Eqns. 6.7})$$

The differences between equations 6.5 and 6.6 are small but critical to the analysis. If the actual shock shapes were standing

cosine waves as in Freeman's theory, then these differences would disappear. They are:

- (1) $W(\vartheta)$ is an empirical function which can be considered to be a "distorted sine wave". This function is periodic with a constant frequency. The details of its cycle shape are peculiar to the axisymmetric geometry (see Fig. VI.9). Of these details, only the ratio of peak heights (negative to positive) $S_1 = 1.39$ affects the analysis. It is, in effect, a sixth free parameter to be determined from the data along with the five in equations 6.7.

- (2) Freeman considers only the absolute value of the function.

The necessity for introducing these changes is explainable in terms of the shock shapes shown in figure VI.8. Note that, as was explained in section VI.4, the treatment of the transverse wave system as a single compressive wave is an idealization which may not be universally applicable.

When the transverse waves intersect the main shock at the walls of the tube, the shape of the shock is convex forward as shown in figure VI.8a and ξ takes on its maximum value. This shape is fairly similar to the theoretical shape in VI.8d.

As the transverse waves move in toward the center, the shock has a compound shape as ξ passes through zero. Note that the "total perturbation" as defined by Freeman is not zero. This shape is shown in figure VI.8b and contrasts with the theoretical shape in

VI.8e. In the axisymmetric case, at least, the shape for $\xi = 0$ occurs when the transverse waves are closer to the center than to the walls, causing the negative half of the cycle to be narrower than the positive half. In VI.8b the value of ϑ is somewhat greater than π , while the theoretical shape VI.8e occurs at $\vartheta = \pi$ exactly.

When the transverse waves meet at the center of the tube the shape of the shock is concave forward as shown in figure VI.8c and ξ takes on its maximum negative value. In the axisymmetric case there is a focusing of the waves at the center which causes the amplitude of this negative half of the cycle to be slightly larger than that of the positive half. Notice that this shock shape is nothing like the theoretical shape of VI.8f which is physically impossible.

The net result of all these considerations is that the function $W(\vartheta)$ has the shape shown roughly in figure VI.9.

This function shows up in the data plotted in figure VI.7. From this figure one can readily see the significance of the differences between equations 6.5 and 6.6. The use of $W(\vartheta)$ allows the amplitudes of the positive and negative peaks to be independently determined. The separation of the positive and negative peaks allows their decay envelopes to be independently determined. These two independent decay calculations each lead to the values $\alpha = -.25$ and $n = 0.50$. Although all the other parameters determined from figure VI.7 are peculiar to the particular geometry of the experiment, there is no reason to believe that the value of the decay

constant n should not apply universally to all transverse disturbances in all shock tubes and, in fact, to the problem of shock stability in general.

Because of the extreme importance of this decay constant and the large discrepancy between it and the one arrived at by Lapworth, it was felt necessary to re-evaluate his experiments in detail. This is accomplished in the next section.

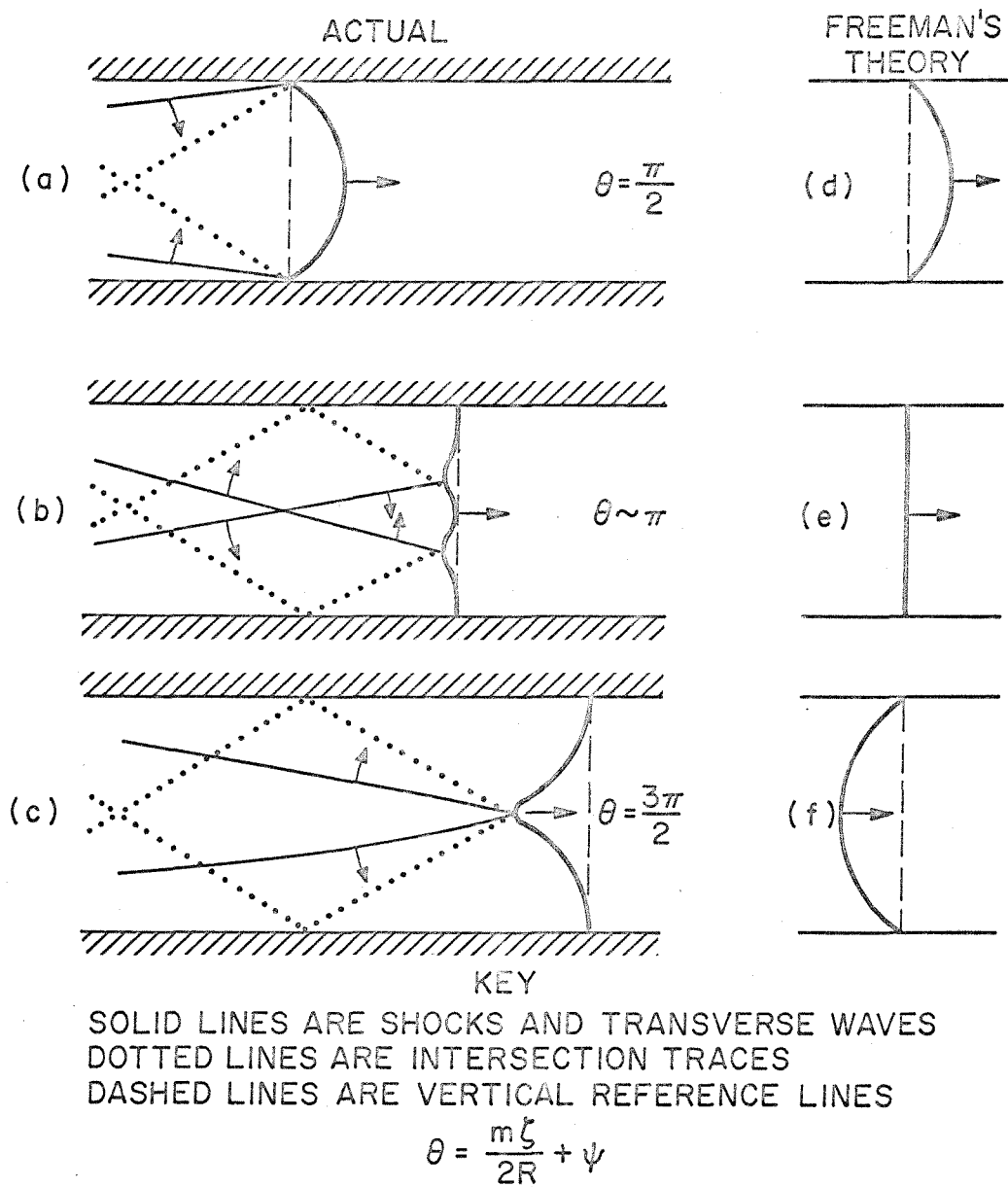


FIG. VI.8
 SHOCK SHAPES

KEY

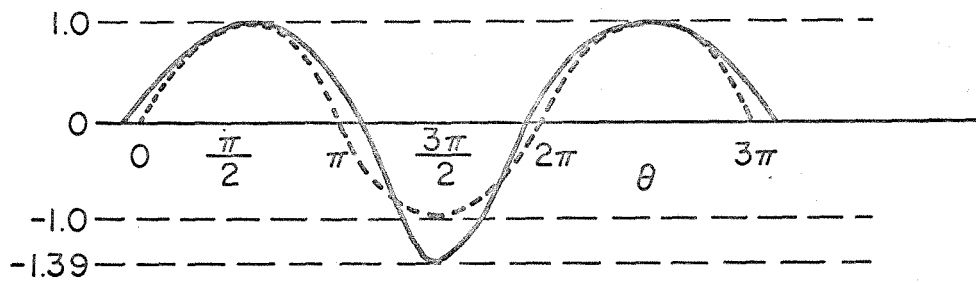


FIG. VI.9
SKETCH OF THE
EMPIRICAL FUNCTION $W(\theta)$

VI.6 Re-Evaluation of Lapworth's Experiment

Lapworth's experiment differed from ours in two important respects:

- (1) The geometry was two-dimensional rather than axisymmetric.
- (2) The post-shock flow past the disturbance was subsonic rather than supersonic.

The second seems to tie in with an apparent discrepancy between "high" Mach numbers and "normal" Mach numbers in Freeman's theory. (This turns out to be coincidental.) Nevertheless, it was thought advisable to replot the data from Lapworth's experiments and recompute the decay constant, fitting the data to equation 6.6 (but with W' particular to the two-dimensional geometry) rather than 6.5. This replot for $M = 1.41$ is figure VI.10 and corresponds to figure 9 of reference 11.

It is immediately apparent that the data of Lapworth's experiment fit beautifully the same decay constant ($n = 0.50$) which was determined in the axisymmetric experiment. This raises the question of why Lapworth obtained a decay constant of about 1.5 (1.45 for this Mach number) from the same data.

This question may be satisfactorily answered by the following comparisons of Lapworth's analysis with ours:

- (1) He used a fixed position for the origin of decay based on the asymptotic form of Freeman's theory (which is invalid

near the origin), while in our analysis this position was left open as a free parameter to be determined by the data.

- (2) He discarded the downstream data, regarding it as anomalous, whereas we believe this downstream data to be most valuable in calculating the decay constant.
- (3) He made no distinction between the positive and negative (or convex forward and concave forward) halves of the cycle. This makes the downstream data look more anomalous than it would otherwise. This was probably the most serious effect of his choice of the "total perturbation" as dependent variable.
- (4) He apparently used a constant weighting function in his least-squares fit, while we have used a repeating delta function, using only the peak values in the determination of the decay envelope, thus making the decay fit independent of the cycle shape of the periodic function used in the fit.

In order to show explicitly how the choice of the origin of decay dominated the results, equations 6.5 and 6.6 will be rewritten in terms of z , the distance from the trailing edge of the disturbance, rather than ζ , the distance from the origin of decay.

Equation 6.5 becomes

$$\frac{\xi}{R} = \frac{2G}{\left(\frac{z}{2R} + .883\right)^n} \left| \sin \left[m \left(\frac{z}{2R} + .883 \right) + \psi \right] \right| \quad (\text{Eqn. 6.8})$$

It is to this equation that Lapworth fitted his data and got $n = 1.45$, $G = .066$, $m = 3.31$, and $\psi = -2.3$. On the other hand, equation 6.6 becomes

$$\frac{\xi}{R} = \frac{2G}{\left(\frac{z}{2R} + a\right)^n} W' \left[m \left(\frac{z}{2R} + a \right) + \psi \right] \quad (\text{Eqn. 6.9})$$

to which his same data were fitted, yielding $n = 0.50$, $G = .0194$, $m = 3.31$, $\psi = 1.24$, and $a = -.175$. [As noted on page 111, the fit for n , G , a is independent of cycle shape.]

Consider the general problem of determining the decay constant of some function of the form

$$\xi = \frac{A}{(z-a')^n}$$

with data available for ξ vs. z at, say, two points. Then

$$\frac{\xi_1}{\xi_2} = \left(\frac{z_2 - a'}{z_1 - a'} \right)^n \quad (\text{Eqn. 6.10})$$

and for small values of a'/\bar{z} , this becomes

$$\frac{\xi_1}{\xi_2} \approx \left(\frac{z_2}{z_1} \right)^{n[1 + a'/\bar{z}]} \quad (\text{Eqn. 6.11})$$

which leads to an apparent value for the decay constant of

$$n(\text{apparent}) \approx n(1 + a'/\bar{z}) \quad [a'/\bar{z} \ll 1] \quad (\text{Eqn. 6.12})$$

and for large (of order 1) values of a'/\bar{z} the error in n tends to infinity.

This general result can now be applied to the problem at hand. In Lapworth's work the quantity a'/\bar{z} corresponds to the ratio of the difference in placement of the origin of decay to the mean distance from the origin to the points used in the computation, and this quantity has a value of about 1/2. This easily accounts for the difference in the decay constants obtained from the two analyses.

Intimately related to the placement of the origin of decay is the failure (noted by Lapworth) of Freeman's theory to properly predict the phase angle ψ , which might be called the "origin of periodicity". The point is that these are not "failures" of the theory at all, but limitations of it due to its asymptotic nature.

Figure VI.5 showed the transverse wave geometry for the axisymmetric rooftop experiment, where the post-shock flow was supersonic with respect to the disturbance. Figure VI.11 is a corresponding diagram for Lapworth's experiment where the disturbance was

subsonic. In the subsonic case the transverse wave propagates back toward the diaphragm instead of being held at the disturbance, but the cases are otherwise identical. The angle at which the intersection trace meets the walls is still given by equations 6.2,3,4 and for Lapworth's experiment ($M = 1.41$ in air) these equations lead to $\Psi = 42.7^\circ$, $Y = .678$, and

$$\beta = 28.4^\circ \quad (\text{based on } M_w = 1)$$

The experimental value, based on the wavelength of figure VI.10 is 28° . There is some uncertainty in the calculation of the theoretical β since only the incident Mach number is known. The transmitted Mach number was not measured in Lapworth's experiments but could not have varied much from the incident value. Thus it is concluded that M_w was very close to 1.

On the basis of this re-evaluation of Lapworth's experiment, the following conclusions are drawn.

- (1) There is no essential difference in the mechanism or geometry of downstream transverse wave propagation between the cases of subsonic and supersonic post-shock flow past a disturbance.

- (2) In either of the above cases and for either rectangular or cylindrical geometry, shock shape perturbations due to symmetric disturbances seem to die out with a decay constant $n = 0.50$ as they travel down the tube.

RE-PLOT OF LAPWORTH'S DATA
TOTAL PERTURBATION vs DISTANCE TRAVELLED

$M = 1.41$

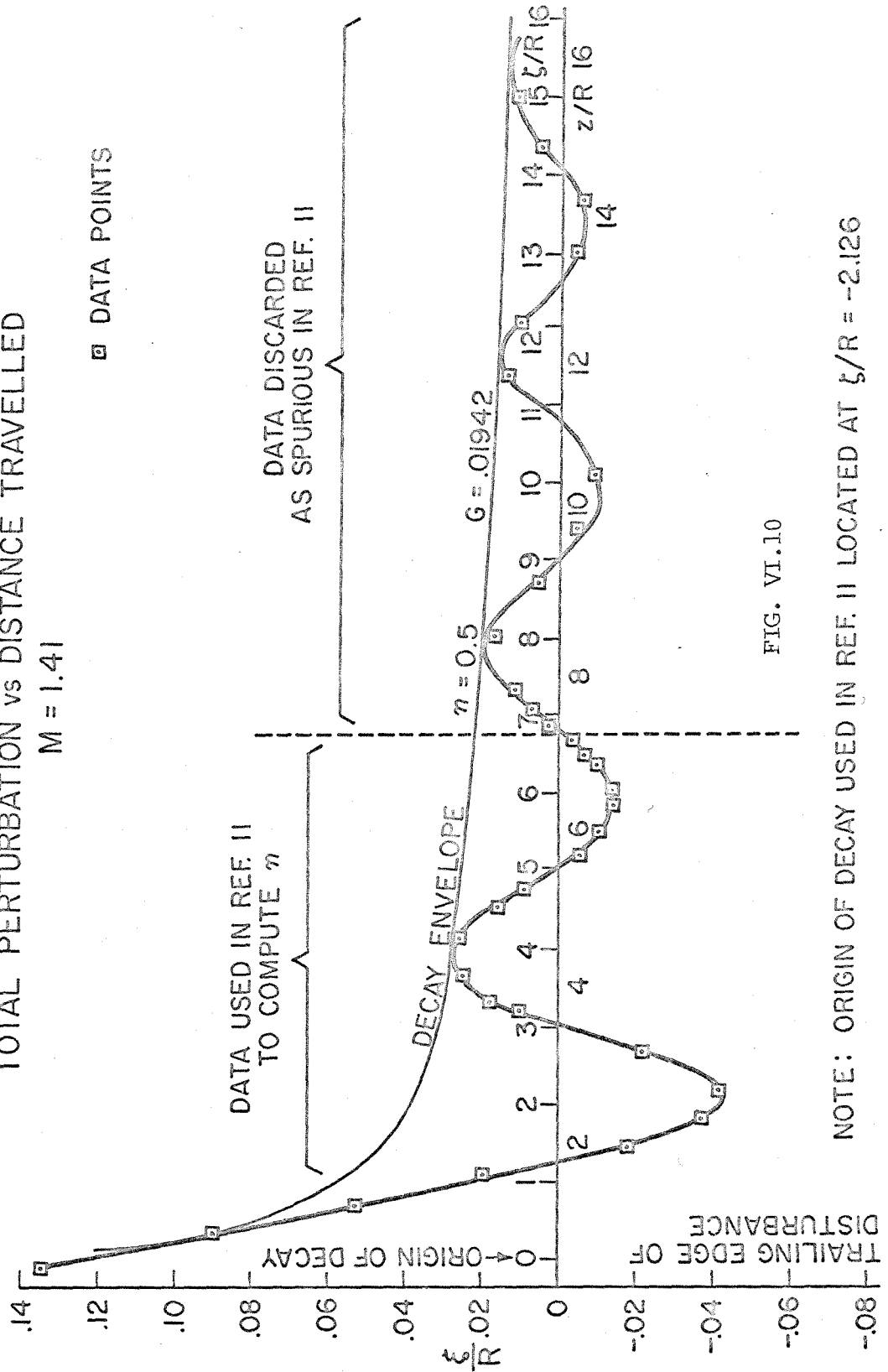


FIG. VI.10

NOTE: ORIGIN OF DECAY USED IN REF. II LOCATED AT $\xi/R = -2.126$

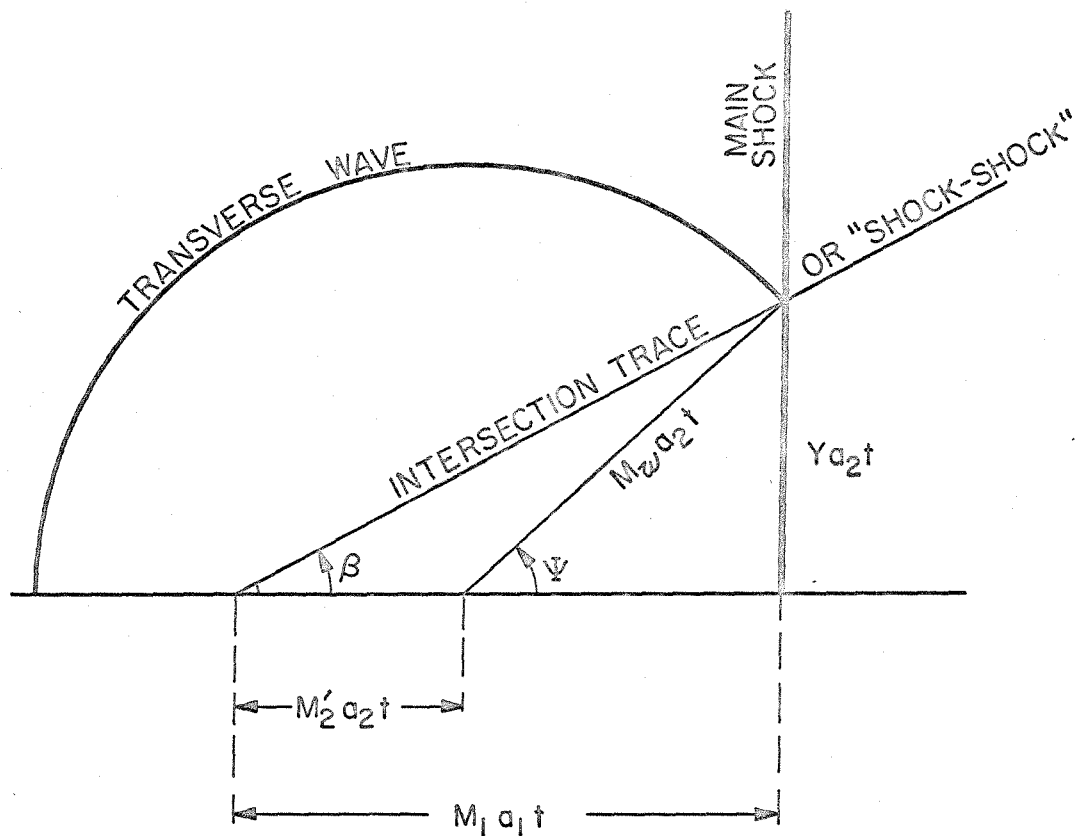


FIG. VI.11

TRANSVERSE WAVE GEOMETRY
FOR SUBSONIC DISTURBANCE

$$(M_w \geq 1 > M'_2)$$

VII. TRANSITION BETWEEN THE TRANSVERSE
WAVE AND BOUNDARY LAYER REGIMES

VII.1 The Rooftop Experiment at $p_1 = 100\mu$ Hg

It was shown in figure VI.3 that the shock shapes produced by the axisymmetric rooftop disturbance were the same at both pressures tested. This similarity of shape, including both magnitude and phase of oscillation continued down the tube for approximately 14 radii before ending rather abruptly. Figure VII.1 shows how the experimental values of shock perturbation at 100μ Hg compare with the experimental curve followed by similar data at 3 mm Hg. Three different regions can be observed. In the first region, corresponding to the transverse wave regime, agreement between the two sets of data is excellent. Then in the second region, corresponding to the transition between regimes, the 100μ perturbation decays much more rapidly and the shock shape oscillates with a much shorter wavelength. In the third region, corresponding to the boundary layer regime, the perturbations at 100μ Hg have essentially disappeared and the shock shape is just that predicted by boundary layer theory.

SHOCK PERTURBATION @ $\xi/R = .896$ vs DISTANCE TRAVELLED
 DUE TO AXISYMMETRIC ROOFTOP DISTURBANCE

$p_1 = 100 \mu \text{ Hg}$ ($Re = 648$), $M = 4.81$

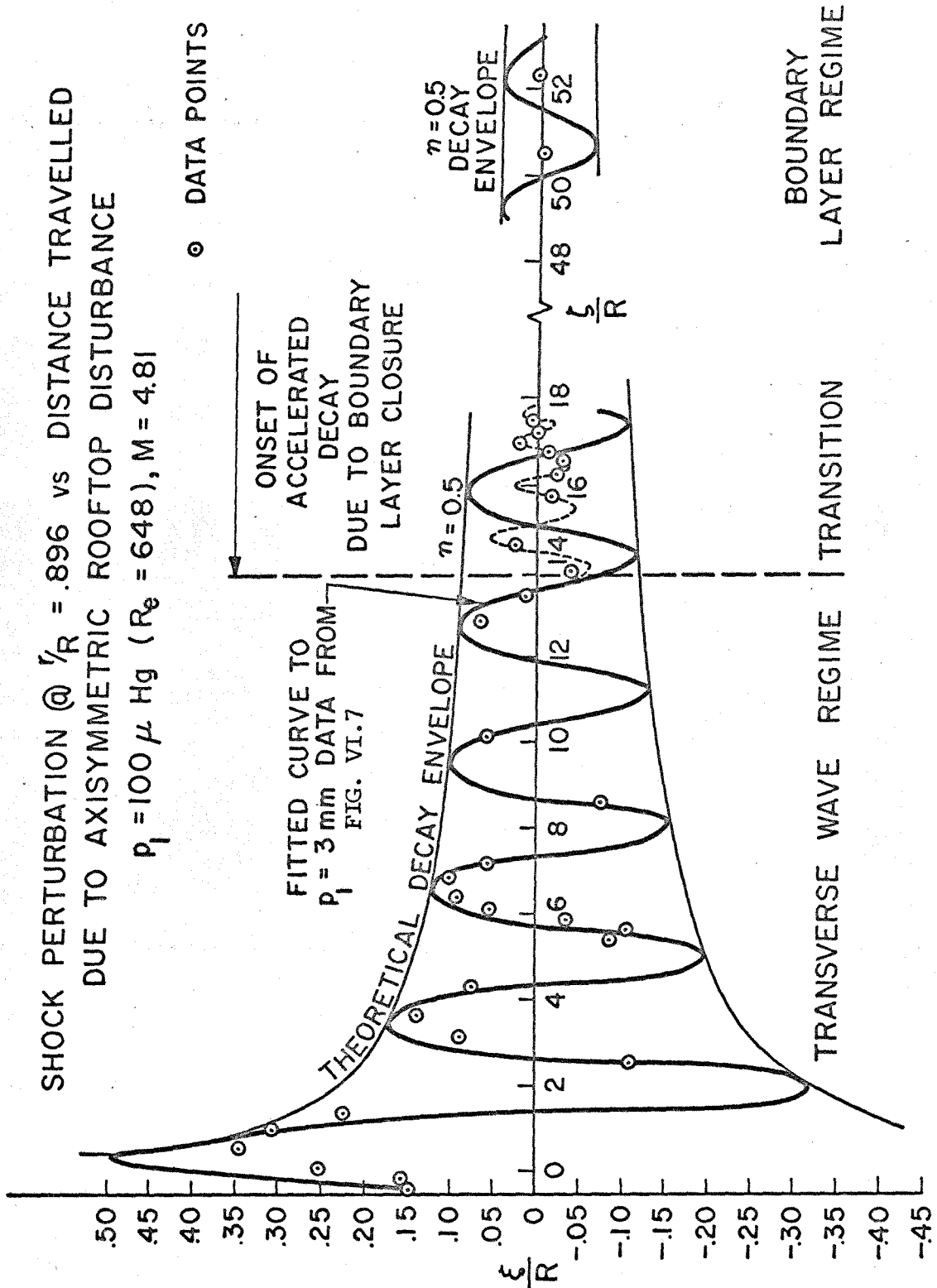


FIG. VII.1

VII.2 Physical Explanation of the Transition Region

Back in section VI.2 three possible causes of the pressure dependence were suggested. The rooftop experiments definitely eliminated the first two. It is now obvious that the third possibility is the correct one, but that it must be modified as follows:

The decay of the transverse waves is greater
at low pressures for a particular tube length.

Thus it is not really correct to speak of a pressure dependent decay, for the decay, as shown in figure VII.1 is really dependent upon some dimensionless combination which includes both the tube length and the initial pressure. Such a combination is the ratio of the boundary layer thickness to the tube radius, measured at the disturbance. This boundary layer may be thought of as a variable-density atmosphere which is diffracting the shock wave. Alternatively, the boundary layer may be idealized as a fictitious wall closing in on the transverse wave system, shortening the wavelength of reflection until the waves are completely "choked off". While the first of these two explanations is probably closer to the truth, the second leads to a simple rule of thumb which works well for the experiments available.

VII.3 Rule of Thumb Transition Condition

Whatever the mechanism through which the boundary layer effects the accelerated decay of the transverse waves, the experimental observations can be correlated with the ratio of some boundary layer thickness to the tube radius.

Let the boundary layer thickness at a distance L behind the shock be

$$\delta' = 10 \sqrt{\frac{L}{p_1}} \quad (\text{Eqn. 7.1})$$

where L is in mm and p_1 is in μ Hg, then for argon and air this represents a positive thickness which is (to within 10% or so) numerically equal to the displacement thickness of a completely laminar boundary layer. The experiments with both the rooftop disturbance and the natural diaphragm disturbance indicate that transition from the transverse wave regime to the boundary layer regime always takes place when the boundary layer as defined above is about $1/4$ to $1/2$ of the tube radius, or

$$\frac{1}{4} < \frac{\delta'}{R} = \sqrt{\frac{100L}{p_1 R^2}} < \frac{1}{2} \quad (\text{Eqn. 7.2})$$

where L and R are in millimeters and p_1 is in μ Hg.

Changing the pressure units and squaring equation 7.2, one obtains the equivalent condition:

$$.6 < \frac{L}{p_1 R^2} < 2.3 \quad (\text{Eqn. 7.3})$$

where L and R are still in millimeters, but p_1 is in mm Hg. Of course the constant of proportionality used in the definition of the boundary layer thickness, for a real boundary layer would be a function of the coefficient of viscosity and of the ratio of specific heats of the gas and is also a weak function of Mach number, the Mach number dependence becoming more important as the viscosity-temperature coefficient departs from $\omega = .7$. Other possible effects not explicitly taken into account are those of the contact surface and of transition. We have, however, qualitative evidence that these do not significantly affect the results. At $p_1 = 3$ mm Hg the decay followed the $n = .5$ scheme far past where other experiments in the same tube by Roshko and Smith (Ref. 21) indicate transition and contact surface occur. At $p_1 = 100\mu$ Hg, where a marked increase in the rate of decay and a rapid shift in disturbance wavelength occur, these effects take place well past the contact surface and long before transition.

Thus it is felt that in the absence of accurate boundary layer growth, transition, and contact arrival measurements in a particular tube, the best one can do is use the rule of thumb that transition between the transverse wave and boundary layer regimes takes place when the quantity $L/p_1 R^2$ is of order 1, where L and R are the tube length and radius in millimeters and p_1 is the initial pressure in the test section in mm Hg.

It must be strongly emphasized that this rule of thumb, being dimensional, must be applied with care. If one is operating in an "unusual" gas such as hydrogen or xenon, or at exceptionally low or high Mach numbers, one might wish to resort to the more fundamental dimensionless transition criterion, $|\delta^*|/R \sim 1/3$. However, because of the "order of magnitude" nature of the analysis and the fact that the boundary layer closure is merely a conceptual convenience (the true mechanism not being fully understood) the results of any such effort should not be taken too seriously.

VIII. IMPLICATIONS FOR DATA INTERPRETATION

VIII.1 General Considerations

It has been found that in the absence of boundary layer closure acceleration of the decay process, the transverse waves set up by a disturbance such as an area change or the diaphragm opening persist indefinitely, decaying only like $z^{-1/2}$. In the GALCIT 17" tube the disturbance due to diaphragm opening produces shock slopes at the centerline of the tube (tilt) of as much as 1 1/2 degrees after $z/R = 96$. In order that this disturbance be reduced to say half a degree, it would be necessary that the tube be nearly 900 radii long. This is, of course, impractical.

The relationship between diaphragm opening time and tube radius is such that the initial disturbance magnitude is probably of the same order for all conventional diaphragm-operated shock tubes. Thus in all such tubes the three-dimensional effects of transverse waves can only be considered negligible after the boundary layer has "choked off" the disturbance by essentially filling the tube at some point between the disturbance and the test section.

The rule of thumb derived in the last chapter therefore should be applied to all shock tubes when the shock shape is important in the experiment (such as in Schlieren, light refraction, electron beam and other such experiments).

When L/p_1R^2 is significantly less than one, then the shock shape will be completely dominated by transverse wave effects from the diaphragm (or other disturbance if present).

When this quantity is significantly larger than one, the shock shape can be expected to be governed by the boundary layer theory of Hartunian and de Boer, with no influence of diaphragm opening.

It must be noted that if there are other protrusions in the tube (such as ports or windows) large enough to cause disturbances of significant magnitude, then the above criteria must be applied to this disturbance, with L being the distance from the disturbance to the test section.

The next section contains example applications of the rule of thumb. The results are summarized in figure VIII.1, where the range of the parameter L/p_1R^2 covered for each experiment is shown. Where the bar is cross-hatched, the data showed definite signs of being in the transverse wave regime. Where the bar is dotted the data followed roughly the predictions of the boundary layer theory but considerable scatter was evident. Where the bar is clear the data agreed exceptionally well with the theory of the boundary layer regime.

VIII.2 Example ApplicationsVIII.2.1 Duff & Young (Ref. 3)

$$R = 14.3 \text{ mm}$$

$$L/R = 268$$

$$p_1(\text{max}) = 20 \text{ mm Hg}$$

$$\frac{L}{p_1 R^2} = \frac{268}{(20) 14.3} = .94$$

in the transition region. Accelerated decay should be occurring, but probably is not complete. Some scatter in data due to diaphragm disturbance is to be expected. However, in the same tube at $p_1 = 10 \text{ mm Hg}$:

$$\frac{L}{p_1 R^2} = \frac{268}{(10) 14.3} = 1.88$$

Decay of transverse waves should be about complete. At this and lower pressures less scatter in data due to these effects (see section I.1.3).

The experiments show very little scatter except at $p_1 = 20 \text{ mm Hg}$ and at the lowest pressures. The scatter in the very low pressure data could be due to the difficulty of reading low amplitude responses (see figure 4 of reference 3).

VIII.2.2 Lin & Fyfe (Ref. 2)

$$R = 305 \text{ mm}$$

$$L/R = 41$$

$$p_1(\text{max}) = .30 \text{ mm Hg}$$

$$\frac{L}{p_1 R^2} = \frac{41}{.3 (305)} = .45$$

probably near the limit of the transverse wave regime. Expect scatter with M and apparent thickening of shock. In the same tube at $p_1 = .10 \text{ mm Hg}$:

$$\frac{L}{p_1 R^2} = \frac{41}{(.1) 305} = 1.35$$

Accelerated decay should be taking place. Deviations, though detectable in shape should have little effect on apparent thickness, which is quite large at this p_1 (see section I.1.2).

Only the low pressure data in Lin & Fyfe's experiments cover a range of Mach numbers. This data shows considerable random scatter but no Mach number dependence. The expected Mach number scatter at high pressures cannot be confirmed because the data were isolated points.

VIII.2.3 Linzer & Hornig (Ref. 22)

$$R = 35 \text{ mm}$$

$$L/R = 98$$

$$p_1(\text{min}) = 310 \text{ mm Hg}$$

$$\frac{L}{p_1 R^2} = \frac{98}{310 (35)} = .00904$$

This is orders of magnitude too small for any damping of the transverse waves by the boundary layer. Decay is definitely $n = .5$.

Pressures in these optical reflectivity experiments ranged from this to a factor of ten higher still. Any curvature due to the boundary layer should be completely negligible. Data should be completely dominated by disturbances of the diaphragm and other sources (there were windows protruding 1/16" into this small tube). Tilt of 1/2 a degree is sufficient to change optical reflectivity measurements by 50%. It is very possible that tilt angles much greater than this were present.

It is interesting to note that in the experiments of Linzer & Hornig, the data were adjusted for "shock curvature" with the correction factor scaled according to $p_1^{-1/2}$. Such a scaling law is, of course, only valid within the boundary layer regime.

VIII.2.4 Wray (Ref. 7)

$$R = 305 \text{ mm}$$

$$L/R = 60$$

$$p_1(\text{max}) = 10 \text{ mm Hg}$$

$$\frac{L}{p_1 R^2} = \frac{60}{10 (305)} = .0197$$

This experiment is definitely in the transverse wave regime. Shock shape should be dominated by disturbances from upstream. At the lowest initial pressure,

$$p_1(\text{min}) = .25 \text{ mm Hg}$$

$$\frac{L}{p_1 R^2} = \frac{60}{.25 (305)} = .79$$

the shock shape should be entering the transition region. Transverse wave effects should be still evident, but possibly of lesser magnitude.

This explains why Wray, even though he reduced the optical path length to take in only the center section of the tube, had to discard the high pressure data completely because of "tremendous scatter" (see section I.1.6).

VIII.2.5 Daen & de Boer (Ref. 6)

$$R = 12.7 \text{ mm}$$

$$L/R = 197$$

$$p_1(\text{typical}) = 127 \text{ mm Hg}$$

$$\frac{L}{p_1 R^2} = \frac{197}{127 (12.7)} = .122$$

This should be well within the transverse wave regime, which explains the apparent shock zone thicknesses 2 to 10 times those expected which were observed in their experiments (see section I.1.6).

VIII.2.6 de Boer (Ref. 8)

In this reference, de Boer notes that there seems to be a dividing line at $p_1 = 30$ mm Hg above which the shock apparent thickness no longer decreases as predicted by theory. This dividing line is evident in figure 42 of reference 8. If the theory of chapter VII is to hold, then $p_1 = 30$ mm Hg should correspond to the transition region in de Boer's experiments and the shock shape regime parameter $L/p_1 R^2$ at this pressure should be of order 1. The half-heights in de Boer's rectangular tube were 3/8" and 5/8". Thus 1/2" will be chosen as R , the effective mean radius.

$$R = 12.7 \text{ mm}$$

$$L/R = 384$$

$$p_1(\text{transition}) = 30 \text{ mm Hg}$$

$$\frac{L}{p_1 R^2} = \frac{384}{30 (12.7)} = 1.007$$

which is indeed of order one. (Since this calculation is only accurate to one significant figure due to the nature of the derivation of this rule of thumb, no claim is made that the extreme proximity of this value to 1 is anything but fortuitous.)

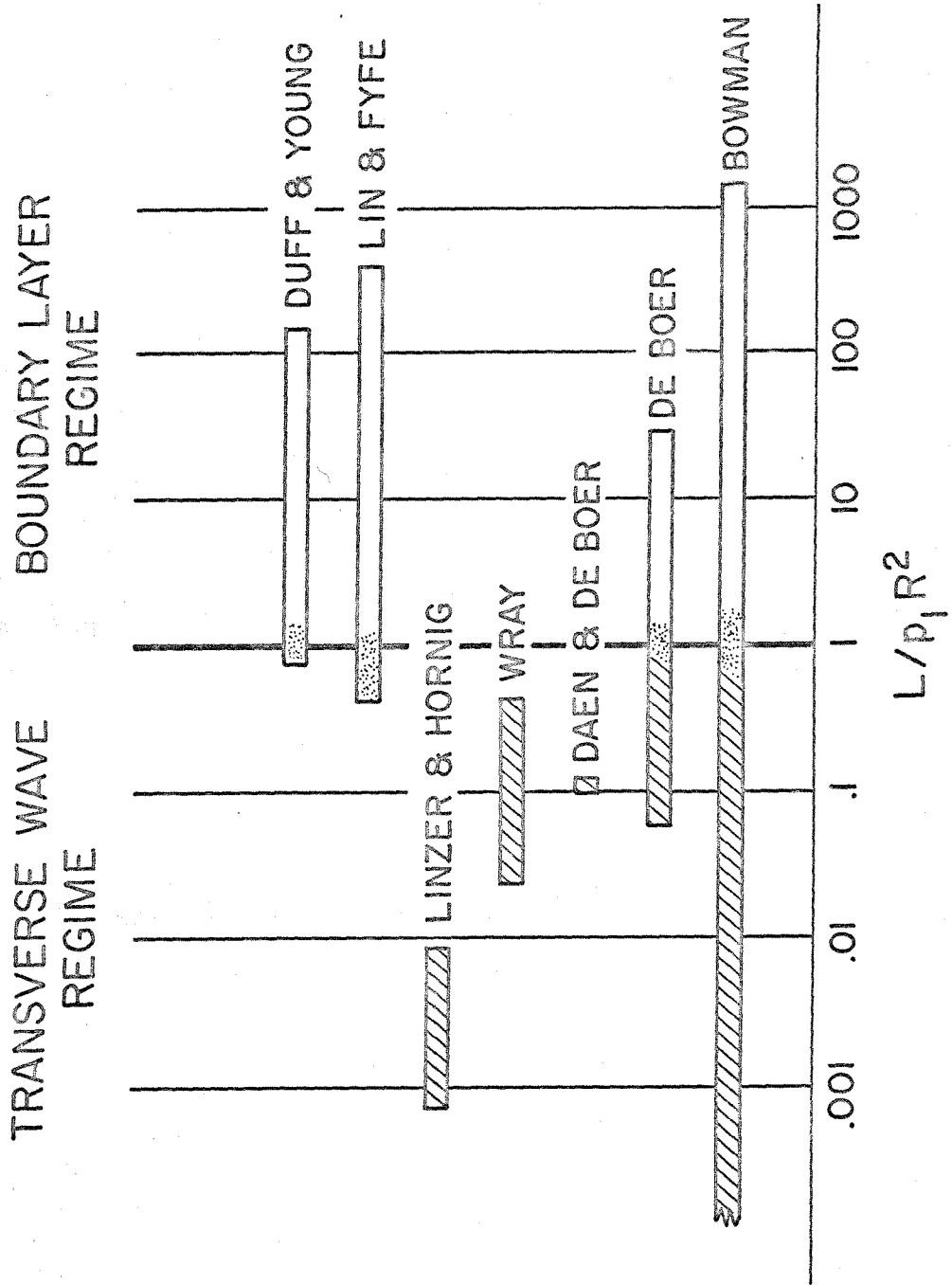


FIG. VIII.1

DATA INTERPRETATION SUMMARY

IX. IMPLICATIONS FOR SHOCK TUBE DESIGN

IX.1 The Conventional Shock Tube

The implications of these results to the design of conventional shock tubes are obvious. If any kind of work is contemplated in the tube in which shock shape is important, then the dimensions of the tube, its strength (or pressure capacity), its vacuum capability, and its instrumentation must all be compatible with an operating regime for which the relationship $L/p_1R^2 \geq 1$ holds.

Because of the extremely small testing time (and therefore possibility of interaction between contact region and the main shock) at very low pressures, it is desirable that the upper limit of the testing regime be at as high a pressure as the instrumentation rise time and resolution will allow. For shock thickness, shock structure, and relaxation time studies, this means $p_1(\text{max})$ should be about 1 mm Hg. This leads to the requirement that the tube geometry satisfy

$$L/R^2 = 1 \quad (\text{dimensions in mm}) \quad (\text{Eqn. 9.1})$$

Now the low pressure limit to the operating regime is dependent upon the testing time analysis. For example it may be required that the testing length ℓ_m , as defined by Roshko (Ref. 23), be a particular multiple of the shock thickness (say 10, for example). Using the value of ℓ_m given by the somewhat refined theory of

Mirels (Ref. 24) for the case of argon or air, and converting the units to mm and mm Hg for pressure, we obtain for large Mach numbers and a laminar boundary layer:

$$\ell_m = .346 p_1 R^2 \quad (\text{Eqn. 9.2})$$

The shock thickness δ has been measured as a by-product of the shock shape experiments and under the above conditions, and in the same units, is found to be given approximately by

$$\delta = .8 p_1^{-1/2} \quad (\text{Eqn. 9.3})$$

Then the ratio of the testing length to the shock thickness is

$$\frac{\ell_m}{\delta} = .44 p_1^{3/2} R^2 \quad (\text{Eqn. 9.4})$$

If it is required that this ratio be at least 10, then it follows that the minimum permissible initial pressure is given by

$$p_1(\text{min}) = 8/ R^{4/3} \quad (\text{Eqn. 9.5})$$

There is an additional restriction on the initial pressure imposed by the geometry which, it will be shown, is important only for the very smallest tubes. This is the requirement that the tube radius be large (again say by a factor of 10) compared with the shock thickness. From equation 9.3 this requirement leads to

$$p_1(\text{min}) = 8/ R^2 \quad (\text{Eqn. 9.6})$$

The two restrictions on the initial pressure given by equations 9.5 and 9.6 coincide for $R = 1$ mm. For all larger radii the restriction imposed by the testing length (equation 9.5) is the more restrictive. In fact it is easy to show that for the type of shock tube being considered, equation 9.6 is completely academic, for the smallest possible shock tube has a radius greater than 1 mm. Such a tube would be one for which $p_1(\text{min})$ and $p_1(\text{max})$ coincide so that the operating regime is just a point. Since $p_1(\text{max})$ has been chosen to be 1 mm Hg from instrumentation rise time considerations, the radius of this "smallest possible useful shocktube" is obtained by setting $p_1(\text{min}) = 1$ in equation 9.5. The result is $R = 4.8$ mm.

As the tube radius is increased from this value, the operating regime widens indefinitely. However, this widening of the operating regime takes place only provided equation 9.1 is satisfied. Thus as R is increased, the tube length L must increase as R^2 . Now the initial cost of a shock tube is roughly proportional to the weight and thus will be given approximately by

$$\text{Initial Cost} \sim L R^{3/2} \sim R^{7/2} \quad (\text{Eqn. 9.7})$$

Moreover the operating cost of a shock tube is roughly proportional to the internal volume and thus will be approximately

$$\text{Operating Cost} \sim L R^2 \sim R^4 \quad (\text{Eqn. 9.8})$$

Thus it is advisable to set a practical limit to the tube radius (and thus to the operating regime). It seems desirable to be able

to vary the initial pressure by a factor of 100. This leads to $p_1(\text{min})$ given by

$$p_1(\text{min}) = \frac{1 \text{ mm Hg}}{100} = 10\mu \text{ Hg} \quad (\text{Eqn. 9.9})$$

This in turn requires that the tube radius be (using equation 9.5)

$$R = (8/.01)^{3/4} = 150 \text{ mm} \approx 6" \quad (\text{Eqn. 9.10})$$

and from equation 9.1 its length must be

$$L = R^2 \approx 23,000 \text{ mm} \approx 900" = 75' \quad (\text{Eqn. 9.11})$$

Then from the above determined tube dimensions and operating pressures, all the other design factors, such as vacuum capability, necessary driver pressure, wall thickness, driver dimensions, etc., can be easily determined.

The operating regime of the shock tube resulting from this example design and that of the GALCIT 17" shock tube are shown in figure IX.1. This figure is a Low Density Shock Tube Design Chart incorporating the limitations

$$p_1(\text{min}) = 8/R^{4/3} \quad (\text{Eqns. 9.12})$$

$$p_1(\text{max}) = L/R^2$$

The instrumentation limit of $p_1(\text{max}) = 1 \text{ mm Hg}$ may, of course, be adjusted as desired for the particular equipment available. It is based on the best gage-electronics combination available at this time for shock structure experiments, Baganoff's (Ref. 25) pressure

gage, which has a rise time of about .1 μ sec. The shock passage time should be at least ten times this, or 1 μ sec. The slowest shock speed normally used is roughly .5 mm/ μ sec, which corresponds to a Mach number of about 1.5. Thus the thinnest shock amenable to accurate structure analysis is one .5 mm thick. This corresponds roughly to an initial pressure of 1 mm Hg.

Note that some types of instrumentation impose a lower limit on usable initial pressures. Pressure gages such as Baganoff's, for example, lose response magnitude rapidly as p_1 is decreased and are practical without amplification (and hence distortion) only above about 10 μ Hg. The heat transfer gages designed for the shock shape study, however, are essentially without a lower pressure limit (see appendix B). They, of course, are unable to faithfully reproduce shock structure in the way that is possible with Baganoff's gages. Such considerations, then, as the type of experiments contemplated and the type of instrumentation anticipated may help establish the desired operating regime of a shock tube and hence, through figure IX.1, the tube dimensions.

The shock deviation from planarity through and on either side of the operating regime of the GASCIT 17" shock tube is shown in figure IX.2. This figure is basically a combined replot of the data presented in figures III.4, IV.2, and V.1 in previous chapters.

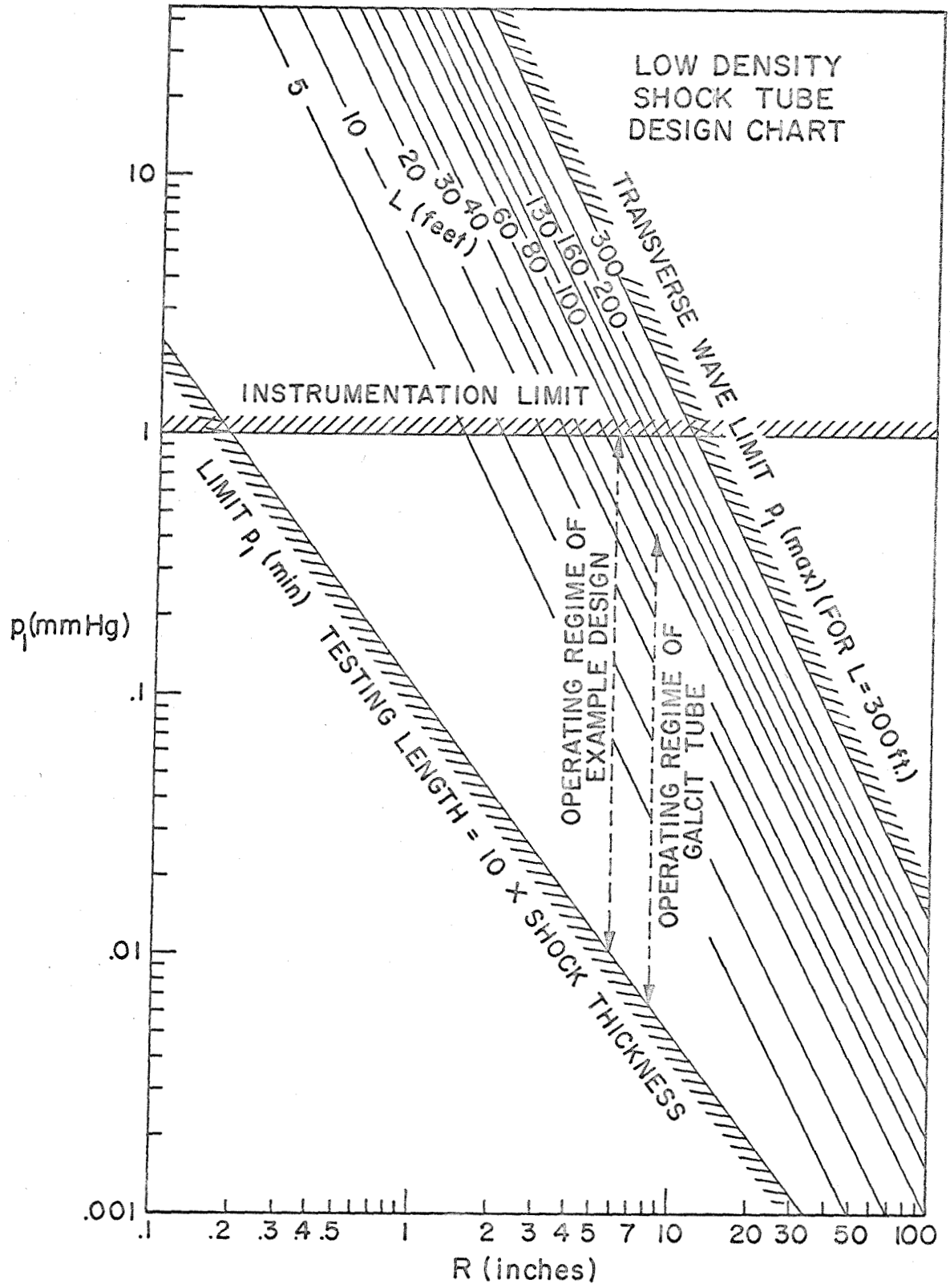
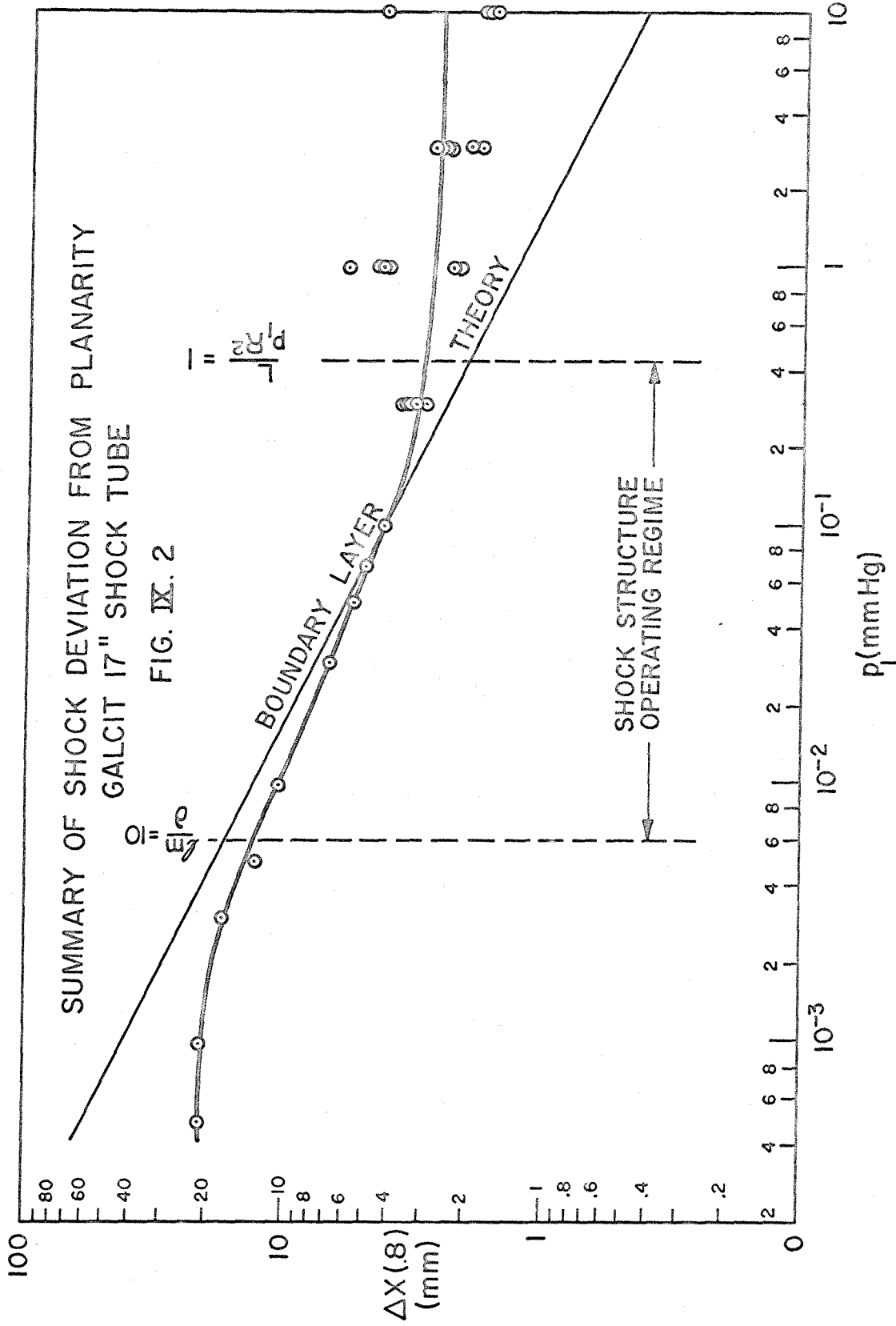


FIG. IX. I



IX.2 The "Hi-Fi" Shock Tube

The results of the last section indicate that in order to avoid the transverse wave regime in a large radius shock tube at moderately high pressures it is necessary to make the tube prohibitively long. Yet the instrumentation capabilities of the large shock tube are so dramatically superior that it seems profitable to search for alternative means of extending the operating regime of such tubes.

Using an extremely long tube to insure boundary layer "choking" of the transverse waves created at the diaphragm is perhaps the "brute force" approach to the problem. It would be more desirable, from both an economic and an esthetic point of view, to eliminate or greatly reduce in magnitude these waves at their source. The resulting "hi-fi" shock tube could be essentially disturbance-free over a wide operating regime and need be only long enough to insure:

- (1) the coalescence of the compression train into a well-defined equilibrium shock and
- (2) the attainment of sufficient testing length between shock and contact surface.

The first method which comes to mind for eliminating the transverse waves at their source is simply to eliminate the source--the bursting diaphragm. The perfection of an entirely new flow initiation device is an undertaking with tremendous possibilities, but one which is fraught with difficulties. Many configurations

suggest themselves which have many of the attributes required of such a device, but so far none which has them all. Some of these elusive attributes are listed below.

A flow initiation device should:

- (1) be strong enough to withstand the differential pressures applied to it.
- (2) be completely vacuum tight even while subjected to the stresses caused by the differential pressure.
- (3) be either automatic or controllable from outside the tube without noise-generating electric signals which could prematurely trigger other instrumentation.
- (4) initiate the flow within a very short time interval (a millisecond is typical for diaphragms) in such a way that the flow will be coaxial and uniform in the tube.
- (5) be capable of operating over as wide a range of driving pressures as possible, consistent with the tube design and operating regime.
- (6) preferably be capable of being reset for the next shot remotely, without the tube being opened.

A second method for eliminating the transverse waves is to cancel them out as soon as they are created or, looking at it another way, prevent them from forming. One possible method for reducing their amplitude by using a reverse-bulging diaphragm has already been mentioned in section V.3.

In Whitham's (Ref. 26) theory of shock dynamics he shows that, to the approximation of the theory, the shock propagation problem is identical to the analogous steady supersonic flow problem. If one can calculate the equipotentials of the latter, then he has the successive shock positions of the former. Based on this analogy, the method of characteristics might be used to design a transition section just downstream of the diaphragm of a shock tube, such that the shock wave, which is roughly spherical when produced, may leave the transition section plane. The problem is analogous to designing a supersonic inlet subjected to an inflow which has a radial component of velocity and which must be turned parallel, producing a uniform pressure at the compressor. Figure IX.3 shows how such a transition section might look.

Note that there is the possibility that early boundary layer closure might occur in the transition section. In that case the device could extend the boundary layer regime as well as modify the transverse wave regime. In fact it may be possible to extend the operating regime of existing shock tubes by merely inserting a set of concentric cylindrical sleeves within the tube downstream of the diaphragm, thereby multiplying the number of transverse wave reflections and promoting premature boundary layer closure within the sleeve section.

It should be pointed out that these are merely suggested as possibilities warranting further study. Follow-up research is being conducted under the direction of the author at the Air Force

Institute of Technology. First results from a pilot experiment in a small shock tube are inconclusive.

Even if the above suggestions do not bear immediate fruit, the mere existence of transverse waves justify the hope that one day they will be overcome and researchers will work in a new generation of "hi-fi" shock tubes.

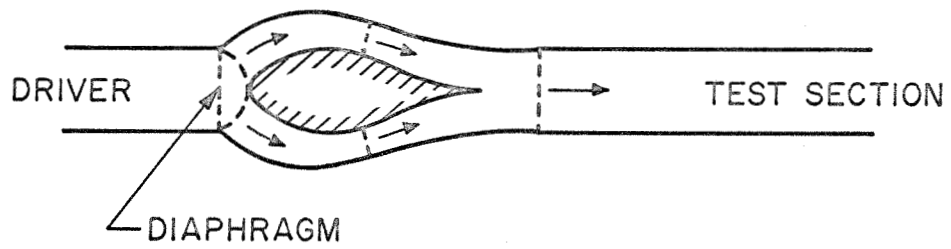


FIG. IX.3
TRANSITION SECTION FOR A
"HI-FI" SHOCK TUBE

REFERENCES

1. Bleakney, W., Weimer, D., & Fletcher, J.C. The Shock Tube: A Facility for Investigations in Fluid Dynamics. Rev. Sci. Instr. 20:807, 1949.
2. Lin, S.C. & Fyfe, W.I. Low Density Shock Tube for Chemical Kinetics Studies. Phys. Fluids 4:238, 1961.
3. Duff, R.E. & Young, J.L. III Shock-Wave Curvature at Low Initial Pressure. Phys. Fluids 4:812, 1961.
4. Hartunian, R.A. Shock Curvature Due to Boundary-Layer Effects in a Shock Tube. Phys. Fluids 4:1059, 1961.
5. Johnson, D.S. GALCIT Aeronautical Engineer's thesis, 1962.
6. Daen, J. & de Boer, P.C.T. Some Studies on Argon, Helium, and Carbon Dioxide with an Integrated-Schlieren Instrumented Shock Tube. J. Chem. Phys. 36:1222, 1962.
7. Wray, K.L. Shock-Tube Study of the Coupling of the O₂-Ar Rates of Dissociation and Vibrational Relaxation. J. Chem. Phys. 37:1254, 1962.
8. de Boer, P.C.T. The Curvature of Shock Fronts in Shock Tubes. U. Maryland TN BN-297, 1962.
9. de Boer, P.C.T. The Curvature of Shock Fronts in Shock Tubes. Phys. Fluids 6:962, 1963.
10. Freeman, N.C. On the Stability of Plane Shock Waves. J. Fluid Mech. 2:397, 1957.
11. Lapworth, K.C. An Experimental Investigation of the Stability of Plane Shock Waves. J. Fluid Mech. 6:469, 1959.
12. Liepmann, H.W. & Bowman, R.M. Shape of Shock Fronts in Shock Tubes. Phys. Fluids 7:2013, 1964.
13. Sichel, M. Leading Edge of Shock-Induced Boundary Layer. Phys. Fluids 5:1168, 1962.
14. Stewartson, K. The Theory of Laminar Boundary Layers in Compressible Fluids. Oxford, 1964.

15. Mirels, H. Laminar Boundary Layer Behind a Strong Shock Moving into Air. NASA TN D-291, 1961.
16. Mirels, H. The Wall Boundary Layer Behind a Moving Shock Wave. in Boundary Layer Research, Proceedings International Union of Theoretical and Applied Mechanics, edited by Gortler, H., Springer-Verlag, p. 283, 1958.
17. Mirels, H. & Hamman, J. Laminar Boundary Layer Behind Strong Shock Moving with Nonuniform Velocity. Phys. Fluids 5:91, 1962.
18. Roshko, A. & Baganoff, D. A Novel Device for Bursting Shock Tube Diaphragms. Phys. Fluids 4:1445, 1961.
19. Liepmann, H.W., Roshko, A., Coles, D., & Sturtevant, B. A 17 Inch Diameter Shock Tube for Studies in Rarefied Gas Dynamics. Rev. Sci. Instr. 33:625, 1962.
20. Whitham, G.B. A New Approach to Problems of Shock Dynamics. Part I. Two-Dimensional Problems. J. Fluid Mech. 2:145, 1957.
21. Roshko, A. & Smith, J.A. Measurements of Test Time in the GALCIT 17-Inch Shock Tube. AIAA Journal 2:186, 1964.
22. Linzer, M. & Hornig, D.F. The Structure of Shock Fronts in Argon and Nitrogen. Princeton U. TR 6, 1963.
23. Roshko, A. On Flow Duration in Low-Pressure Shock Tubes. Phys. Fluids 3:835, 1960.
24. Mirels, H. Test Time in Low Pressure Shock Tubes. Phys. Fluids 6:1201, 1963.
25. Baganoff, D. Pressure Gauge with One-Tenth Microsecond Risettime for Shock Reflection Studies. Rev. Sci. Instr. 35:288, 1964.
26. Whitham, G.B. A New Approach to Problems of Shock Dynamics. Part 2. Three-Dimensional Problems. J. Fluid Mech. 5:369, 1959.
27. Roshko, A. Heat Gauge Circuit Analysis. Unpublished notes.
28. Gradshteyn, I.S. & Ryzhik, I.M. Tables of Integrals, Sums, Series, & Products. Moscow 1963.
29. Wylie, C.R. Advanced Engineering Mathematics. McGraw-Hill, 1960.

30. Aldis Tables of Bessel Functions. Proc. Roy. Soc. LXIV, 1899.
31. Irving, J. & Mullineux, N. Mathematics in Physics and Engineering. Academic Press, 1959.
32. Flugge Four-Place Tables of Transcendental Functions. McGraw-Hill, 1954.
33. Dwight, H.B. Tables of Integrals and Other Mathematical Data, 4th ed., MacMillan, 1961.
34. Rott, N. & Hartunian, R. "On the Heat Transfer to the Walls of a Shock Tube." Cornell Univ. Grad. School of Aero. Eng. Rept., 1955.

APPENDIX A: SHOCK TUBE DESCRIPTION

A.1 Description of the GALCIT 17" Shock Tube

The best general description of the GALCIT 17" shock tube is contained in reference 19, while additional supplementary information is in references 18 and 21.

Since publication of the above references, the following modifications to the tube have been made:

- (1) All valves, pumps, and instrumentation were made operable by remote control from a central control panel, enabling the tube to be operated safely and conveniently by one man.
- (2) The movable diaphragm cutting blades were replaced by a set of interchangeable fixed blades of different cutting-plane curvatures.
- (3) The diaphragm section was equipped with four squaring plates, enabling each quadrant of the ruptured diaphragm to fold, rather than tear, and eliminating petal loss over a wide range of bursting pressures. This modification produced a slight area reduction at the diaphragm and resulted in the Mach number produced at a given diaphragm pressure ratio being reduced to 94% of that predicted by ideal tube theory.

APPENDIX B: FILM GAGE DESCRIPTION

B.1 Film Gage Response Theory

Consider the basic film gage circuit shown in figure B.1 (note that in this appendix only, the symbol R stands for resistance, rather than radius). Sometime prior to shock tube firing, the switch is closed and a steady voltage

$$E = \frac{E_0 R}{R + R_0} \quad (\text{Eqn. B.1})$$

becomes impressed across the gage. A steady current I flows through the circuit. When, after the tube is fired, the shock wave passes (or, in the case of the end wall, reflects from) the gage, the temperature of the gage is raised suddenly. This temperature jump causes the gage resistance to change by an amount ΔR . The relative resistance change is known as a function of the initial pressure of the gas and the shock Mach number. For the case of the end wall gage, this relation leads to the plot in figure B.2. The details of the analysis are given by Roshko (Ref. 27).

When the ballast resistance R_0 is large compared with R, the current is constant, and the output signal ratio, $\Delta e/E$ is equal to $\Delta R/R$. In this case the signal Δe can be increased only by increasing E. If E_0 is fixed, then E is increased by decreasing R_0 . Eventually, the assumption that $R_0 \gg R$ is violated and, finally, if R_0 is decreased to zero the signal also goes to zero for $E = E_0$ regardless of R.

It is clear, then, that the signal Δe must have a maximum for some particular value of R_0 . Since the existence of this maximum is inconsistent with the assumption that $R_0 \gg R$, this assumption must be discarded during the search for the R_0 which yields $\Delta e(\max)$.

By simple analysis of the circuit both before and after the resistance jump, it is found that the signal Δe is given by

$$\frac{\Delta e}{E_0} = \frac{\Delta R}{R_0 + R} \left\{ 1 - \frac{R}{R_0 + R} \left[1 + \frac{\Delta R}{R} \left(1 - \frac{R}{R_0 + R} \right) \right] \right\} \quad (\text{Eqn. B.2})$$

Considering E_0 and R as constants, this equation is differentiated with respect to R_0 and the result set equal to zero. This leads to a quadratic equation for the R_0^* for which Δe is a maximum. There is an explicit approximate solution for the case when $\Delta R \ll R_0, R$. It is simply

$$R_0^* = R \quad (\text{Eqn. B.3})$$

the optimum ballast resistance being equal to the gage resistance.

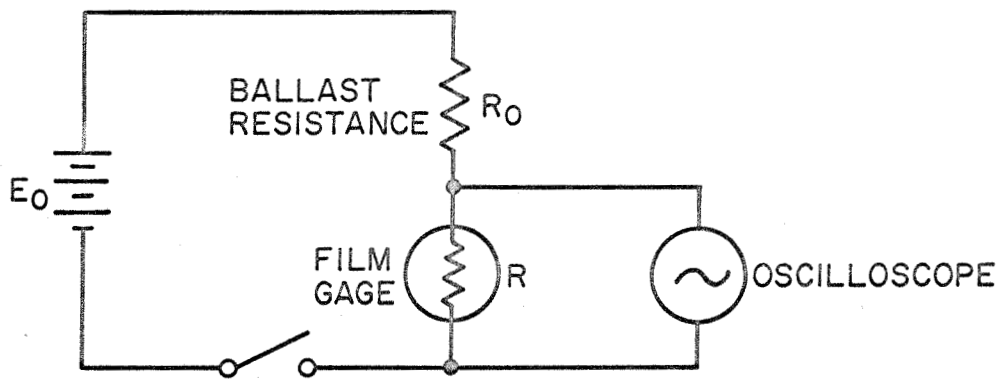


FIG. B.1
BASIC FILM GAGE CIRCUIT

THEORETICAL END-WALL FILM GAGE RESPONSE (FOR AIR AT $T_f = 300^\circ$)

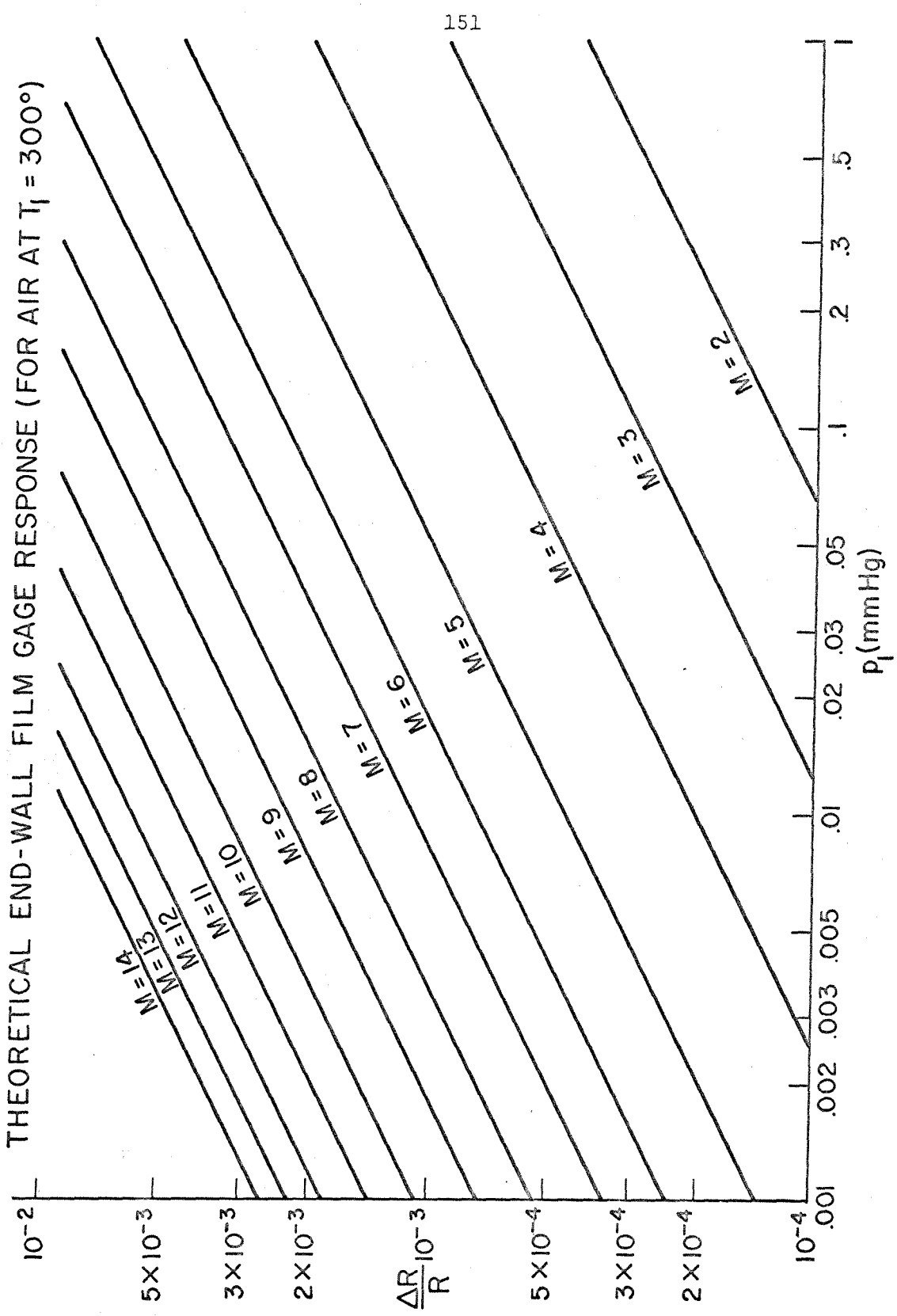


FIG. B-2

B.2 Non-ideal Gage Performance

Thin film gages have not been operable at the "optimum" conditions derived in the last section because of non-ideal behaviour associated with gage heatup. In the past, only small currents (typically 10 ma) have been passed through such gages so that the I^2R heat produced would be negligible. If the current were raised (R_0 lowered) the gage would fail, usually at the junction between the platinum film and the silver paint leads. Such gage burnout imposed a serious restriction on gage operating current (or voltage) and thus on gage response. This restriction has been removed by means described in the next section.

Once this burnout barrier is passed, an additional effect is encountered, also caused by the I^2R heating. As the steady state current is raised, a point is reached above which the heat produced cannot be lost through radiation and conduction and a rapid rise in surface temperature occurs. There is an associated rise in the gage resistance which alters the ratio between R_0 and R and produces a slow rise in the voltage applied to the gage. Since the total circuit resistance is increasing, however, the current through the gage decreases slowly, reducing I^2R until a new equilibrium is reached. Because of this downward creep of the gage current, the gage response is less than ideal. There is a critical point above which attempts to pass more current through the gage will actually produce a lower response.

An effective current I_{eff} can be defined as that gage current which would be required to produce a measured gage response in the absence of these non-ideal effects. Figure B.3 is a plot of effective current vs. actual applied initial current for a thin film gage of $R = 220\Omega$. It can be seen that the effective current is a maximum for an applied current of 120 ma. This corresponds to a gage voltage of $E = 26V$. This, then, is the greatest voltage which should be applied across that gage, regardless of what E_0 is available. If E_0 is fixed, then this $E(\text{max})$ fixes R_0 , usually at a higher value than that given in equation B.3.

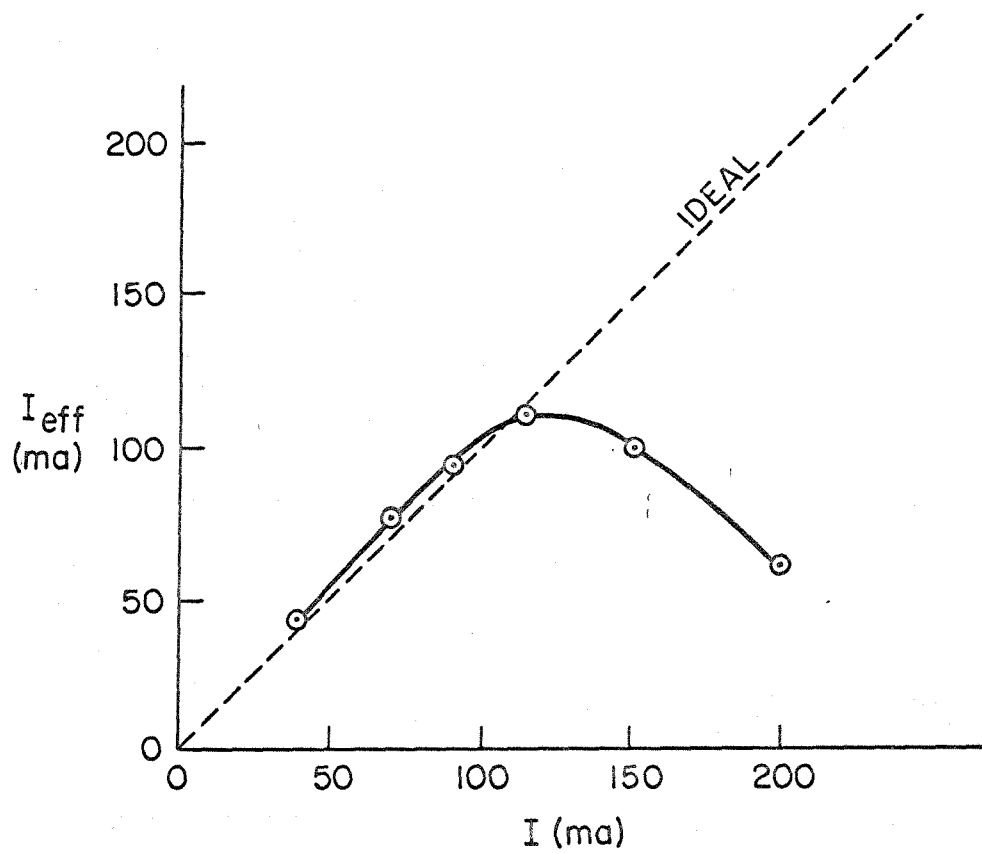


FIG. B.3
EFFECTIVE vs APPLIED CURRENT
FOR TYPICAL THIN-FILM GAGE
($R = 220 \Omega$)

B.3 Prevention of Gage Burnout

It has been found that gage burnout can be eliminated by making the evaporated film and the low-resistance painted leads of the same metal, platinum. This eliminates the metal-to-metal mismatch which occurs between platinum films and silver leads.

The leads are painted on first, in several layers, each layer baked on before painting the next. After the leads have been built up to the point where their resistance is acceptably low (around 5 ohms) the film itself may be evaporated onto the cleaned surface of the gage and baked on. Experience shows that the film is usually damaged by subsequent application of the leads if it is applied first.

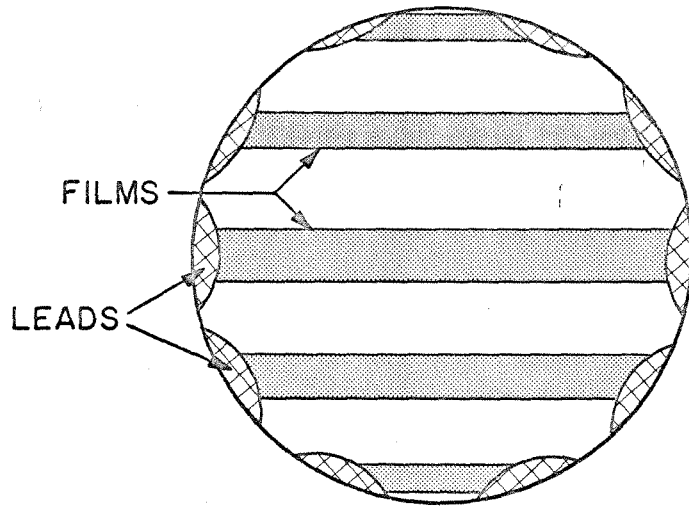
All-platinum gages of approximately 200 ohms resistance have been successfully produced in this way which are capable of withstanding impressed voltages of up to 50V and gage currents of 200ma. The surface areas of the films varied between .004 and .1 in². The films survived over 400 runs in the shock tube, at Mach numbers up to 12, without failure.

B.4 The Multiple-film Gage

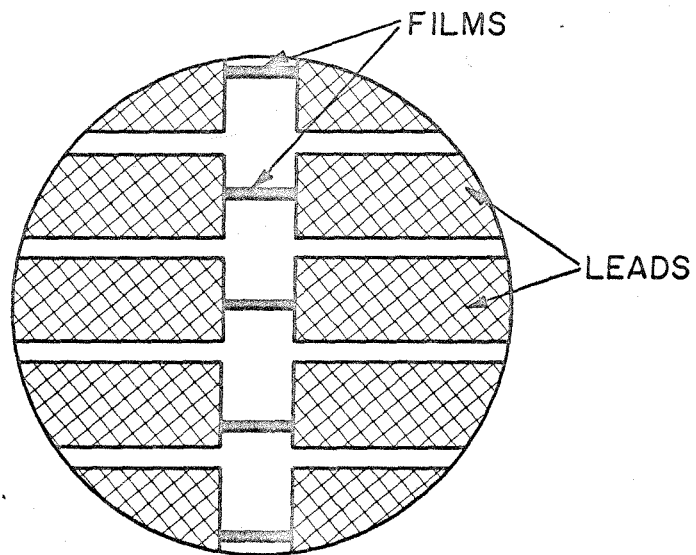
The standard instrumentation ports in the GALCIT 17" shock tube accept gages on cylindrical rods of one inch diameter only. The mounting pads are nearly 3" in diameter, thus requiring the same (3") minimum distance between gages.

Because of the complex shape of the shocks studied in this investigation and because of the lack of axisymmetry in many cases, it was necessary to have as many data points as possible located along a single radius of the endwall. This was accomplished by putting several parallel films on each gage cylinder, each film being provided with its own set of leads.

Each film actually integrates information received over its entire surface area. Thus to be considered a data "point", the film must have dimensions which are small compared with its radial location. The film at the center of the tube must have dimensions small in comparison with the radial distance over which a significant change in the measured quantity is expected to occur. Figure B.4 shows two types of multiple-film gages, the first for general use and the second for use at the center of the tube. The improved gage could also be used in smaller tubes.



(a) TYPICAL 5-FILM GAGE



(b) IMPROVED-GEOMETRY GAGE

FIG. B. 4
MULTIPLE-FILM GAGES
(ENLARGED END VIEW)

APPENDIX C: RE-FORMULATION AND EXTENSION OF
DE BOER'S TWO-DIMENSIONAL SHOCK SHAPE THEORY

C.1 Formulation of the Problem

The same assumptions are employed here as were used by deBoer:
(1) the region behind the shock and outside the boundary layer is a potential flow and (2) the shock makes a small angle with the vertical.

The "wavy wall" approach will be used, solving first for a sinusoidal wall as in figure C.1 and then integrating over all possible frequencies to obtain the actual wall shape as a Fourier integral.

Since the boundary conditions are expressed in terms of the vertical velocity v it seems more direct to use this as the unknown, rather than the velocity potential.

The potential equation in the applicable region is

$$\phi_{xx} + \frac{1}{m^2} \phi_{yy} = 0 \quad (\text{Eqn. C.1})$$

where

$$m^2 = (1 - M_\infty^2) \quad (\text{Eqn. C.2})$$

Differentiating equation C.1 with respect to y ,

$$\phi_{yxx} + \frac{1}{m^2} \phi_{yyy} = 0$$

$$v_{xx} + \frac{1}{m^2} v_{yy} = 0 \quad (\text{Eqn. C.3})$$

Now let $\delta = \frac{x}{m}$. Then

$$\boxed{v_{\delta\delta} + v_{yy} = 0} \quad (\text{Eqn. C.4})$$

which is Laplace's Equation.

The boundary conditions will now be formulated. By symmetry, along the plane midway between the two walls,

$$\boxed{v(\delta, h) = 0} \quad (\text{Eqn. C.5})$$

From the small shock angle assumption it follows that just behind the shock,

$$\boxed{v(o, y) = \left(\frac{dx}{dy}\right)_{sh} (U_1 - U_2)} \quad (\text{Eqn. C.6})$$

which will be used to give the shock shape, once v is found, as follows:

$$x_{sh}(y) = \frac{1}{U_1 - U_2} \int_0^y v(o, y) dy \quad (\text{Eqn. C.7})$$

The boundary condition along the wall is simply that

$$v(\delta, o) = U_{\infty} f'(\delta) \quad (\text{Eqn. C.8})$$

where $f(\delta)$, the shape of the wall, for the wavy wall is just

$$f(\delta) = A \sin \frac{2\pi\delta}{\lambda} \quad (\text{Eqn. C.9})$$

Then equation C.8 becomes

$$v(\delta, 0) = \frac{2\pi AU_{\infty}}{\lambda} \cos \frac{2\pi\delta}{\lambda}$$

(Eqn. C.10)

and the formulation of the problem is complete.

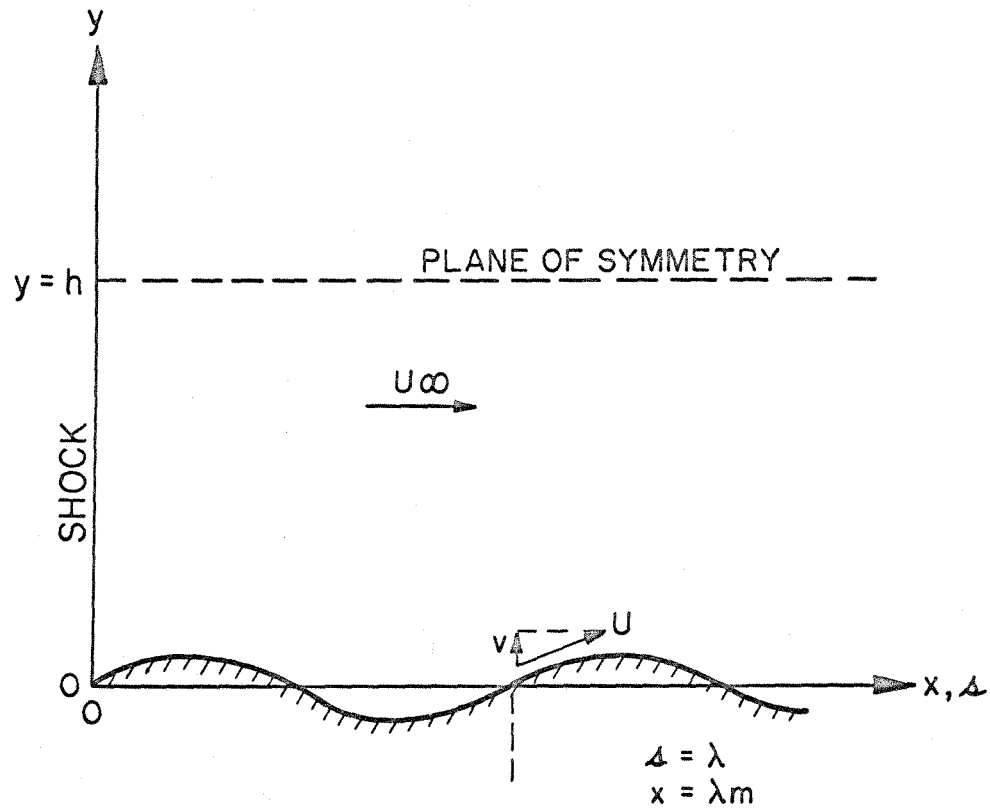


FIG. C.1
 WAVY-WALL GEOMETRY
 2 DIMENSIONAL CASE
 (TWO PARALLEL WALLS)

C.2 Solution of the Problem

The general solution to equation C.4 is

$$v = [A' \cos p\delta + B' \sin p\delta] [C'e^{py} + D'e^{-py}] \quad (\text{Eqn. C.11})$$

Applying equation C.5,

$$D' = -C'e^{2py} \quad (\text{Eqn. C.12})$$

and thus

$$v(\delta, y) = [A'' \cos p\delta + B'' \sin p\delta] [e^{py} - e^{(2h-y)p}] \quad (\text{Eqn. C.13})$$

Now applying equation C.10,

$$B'' = 0$$

$$p = \frac{2\pi}{\lambda} \quad (\text{Eqns. C.14})$$

$$A'' = \frac{2\pi AU_\infty}{\lambda(1 - e^{2hp})}$$

When these are substituted into equation C.13 and the definition of the sinh is employed, the result is

$$v(\delta, y) = \frac{2\pi}{\lambda} AU_\infty \cos \frac{2\pi\delta}{\lambda} \frac{\sinh \frac{2\pi}{\lambda} (h-y)}{\sinh \frac{2\pi h}{\lambda}} \quad (\text{Eqn. C.15})$$

At this point the wavy wall is replaced by a fictitious wall located at the edge of the displacement thickness boundary layer. The equation of this wall is

$$f(x) = - A^* x^{1/2} \quad (\text{Eqn. C.16})$$

Thus

$$v(x,0) = - \frac{A^* U_\infty}{2\sqrt{x}} \quad (\text{Eqn. C.17})$$

Returning to x variables and integrating over all $\frac{2\pi}{\lambda}$, equation C.15 becomes

$$v(x,y) = \int_0^\infty \frac{2\pi}{\lambda} A_\lambda U_\infty \cos \frac{2\pi x}{\lambda m} \frac{\sinh \frac{2\pi}{\lambda} (h-y)}{\sinh \frac{2\pi h}{\lambda}} d\left(\frac{2\pi}{\lambda}\right)$$

Now introducing the quantity $k = \frac{2\pi}{\lambda m}$ and lumping all the constants into a new set of coefficients $A_k = \frac{\pi}{2} m^2 k A_\lambda U_\infty$, this can be written

$$v(x,y) = \frac{2}{\pi} \int_0^\infty A_k \cos kx \frac{\sinh mk(h-y)}{\sinh mkh} dk \quad (\text{Eqn. C.18})$$

The coefficients A_k are evaluated from the boundary condition along the fictitious wall and the definition of the Fourier cosine integral. From equation C.18,

$$v(x,0) = \frac{2}{\pi} \int_0^\infty A_k \cos kx dk \quad (\text{Eqn. C.19})$$

where

$$A_k = \int_0^\infty v(x,0) \cos kx dk \quad (\text{Eqn. C.20})$$

Substituting equation C.17 into this, one obtains

$$A_k = \int_0^\infty - \frac{A^* U_\infty}{2\sqrt{x}} \cos kx dk$$

$$A_k = - \frac{A^* U_\infty}{2} \sqrt{\frac{\pi}{2k}} \quad (\text{Eqn. C.21})$$

and the complete solution for the v field is obtained when this is put into equation C.18 giving

$$v(x,y) = - \frac{A^* U_\infty}{\sqrt{2\pi}} \int_0^\infty \frac{\cos kx}{\sqrt{k}} \frac{\sinh mk(h-y)}{\sinh mkh} dk \quad (\text{Eqn. C.22})$$

Evaluating this at $x = 0$ leads to the shock shape as follows:

$$v(0,y) = - \frac{A^* U_\infty}{\sqrt{2\pi}} \int_0^\infty \frac{\sinh mk(h-y)}{\sqrt{k} \sinh mkh} dk \quad (\text{Eqn. C.23})$$

and using 3.524-3 of reference 28,

$$v(0,y) = - \frac{A^* U_\infty}{\sqrt{2\pi m}} \Gamma\left(\frac{1}{2}\right) \sum_{k=0}^{\infty} \left[\frac{1}{\sqrt{h(2k+1)-h+y}} - \frac{1}{\sqrt{h(2k+1)+h-y}} \right] \quad (\text{Eqn. C.24})$$

then substituting this into equation C.7 and noting that $U_\infty = U_2$,

$$\begin{aligned} x_{sh}(y) &= - \frac{A^* U_2}{\sqrt{2m} (U_1 - U_2)} \sum_{k=0}^{\infty} \left[\int_0^y \frac{dy}{\sqrt{h(2k+1)-h+y}} - \int_0^y \frac{dy}{\sqrt{h(2k+1)+h-y}} \right] \quad (\text{Eqn. C.25}) \\ &= - \frac{A^* U_2}{\sqrt{2m} (U_1 - U_2)} \sum_{k=0}^{\infty} \left\{ 2\sqrt{k(2k+1)-h+y} - 2\sqrt{g} - \right. \\ &\quad \left. [- 2\sqrt{k(2k+1)+h-y} + 2\sqrt{g}] \right\} \end{aligned}$$

where $f = h(2k+1)-h$ and $g = h(2k+1)+k$

$$x_{sh}(y) = - \sqrt{\frac{2}{m}} \frac{A^*U_2}{U_1-U_2} \sum_{k=0}^{\infty} [\sqrt{2hk+y} + \sqrt{2hk+2h-y} - \sqrt{2hk} - \sqrt{2hk+2h}]$$

(Eqn. C.26)

Introducing the dimensionless variable $\bar{\eta} = \frac{y}{h}$, this becomes

$$x_{sh}(\bar{\eta}) = - \sqrt{\frac{2h}{m}} \frac{A^*U_2}{U_1-U_2} \sum_{k=0}^{\infty} [\sqrt{2k+\bar{\eta}} + \sqrt{2k+2-\bar{\eta}} - \sqrt{2k} - \sqrt{2k+2}]$$

(Eqn. C.27)

$$x_{sh}(\bar{\eta}) = - \sqrt{\frac{2h}{m}} \frac{A^*U_2}{U_1-U_2} [\sqrt{\bar{\eta}} + \sqrt{2-\bar{\eta}} - \sqrt{2} + \sqrt{2+\bar{\eta}} + \sqrt{4-\bar{\eta}} - \sqrt{2} - \sqrt{4} + \sqrt{4+\bar{\eta}} + \sqrt{6-\bar{\eta}} - \sqrt{4} - \sqrt{6} + \dots]$$

(Eqn. C.28)

C.3 Evaluation of the Shape

The shock shape has been determined by numerically evaluating equation C.28 at various values of $\eta = 1 - \bar{\eta}$. The series has the value .761 for $\eta = 0$. Shifting the origin of x to the plane through the shock position at the centerline (for consistency with the experiments), and defining $x_{sh}(\eta=1) = \theta$ (the "apparent thickness" or "axial extent"), it is found that

$$\theta = .761 \sqrt{\frac{2h}{m}} \frac{A^* U_2}{U_1 - U_2} \quad (\text{Eqn. C.29})$$

and that the shock shape is as shown in figure C.2.

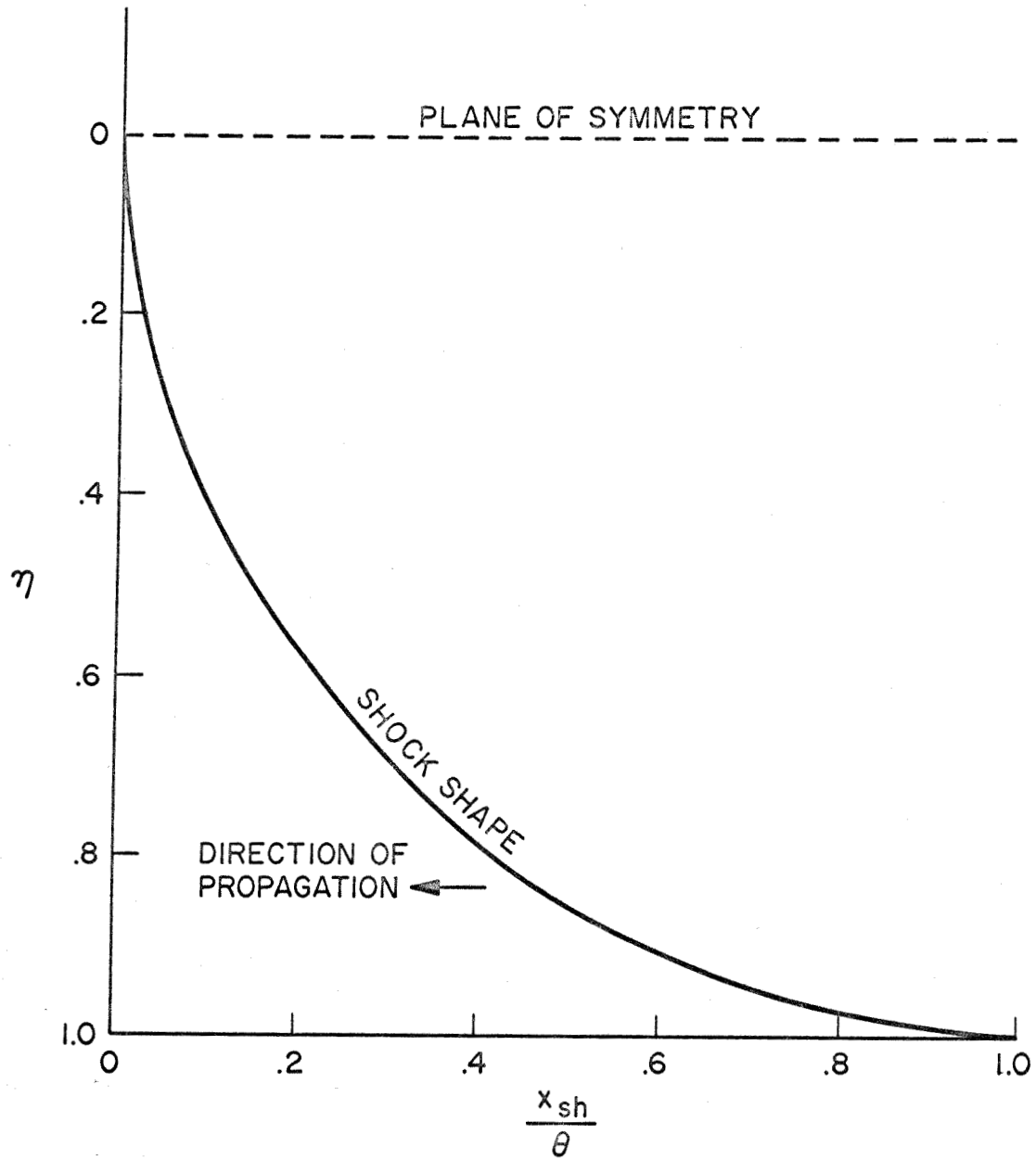


FIG. C.2
THEORETICAL SHOCK SHAPE
2 DIMENSIONAL CASE
(TWO PARALLEL WALLS)

APPENDIX D: RE-FORMULATION AND EXTENSION OF
DE BOER'S AXISYMMETRIC SHOCK SHAPE THEORY

D.1 Formulation of the Problem

As in the two-dimensional case, the sink velocity v will be used as the dependent variable. The procedure is analogous, with the Fourier Bessel integral converting wavy wall results to the desired solution. Since the analogy is obvious, the boundary conditions for the displacement thickness wall will be used immediately. The origin is on the centerline of the tube (see Fig. D.1).

The axisymmetric potential equation is

$$m^2 \phi_{xx} + \phi_{rr} + \frac{1}{r} \phi_r = 0 \quad (\text{Eqn. D.1})$$

Differentiating with respect to r ,

$$m^2 \phi_{rxx} + \phi_{rrr} + \frac{1}{r} \phi_{rr} - \frac{1}{r^2} \phi_r = 0$$

$$m^2 v_{xx} + v_{rr} + \frac{1}{r} v_r - \frac{1}{r^2} v = 0$$

$$r^2 v_{rr} + r v_r - v = -m^2 r^2 v_{xx} \quad (\text{Eqn. D.2})$$

Assuming a product solution, let

$$v(x,r) = F(r) G(x) \quad (\text{Eqn. D.3})$$

then

$$r^2 F_{rr} G + r F_r G - FG = -m^2 r^2 F G_{xx}$$

and

$$\frac{F_{rr}}{F} + \frac{F_r}{rF} - \frac{1}{r^2} = -\frac{m^2 G_{xx}}{G} = p^2 m^2 \quad (\text{Eqn. D.4})$$

The radial equation is then

$$r^2 F_{rr} + r F_r - (p^2 m^2 r^2 + 1) F = 0 \quad (\text{Eqn. D.5})$$

This is the modified Bessel equation.

The axial equation is

$$G_{xx} + p^2 G = 0 \quad (\text{Eqn. D.6})$$

and the boundary conditions are similar to those for the two-dimensional case:

$$v(x, 0) = 0 \quad (\text{Eqn. D.7})$$

by symmetry, and along the wall, whose equation is

$$f(x) = R + A^* \sqrt{x} \quad (\text{Eqn. D.8})$$

the condition is

$$v(x, R) = U_2 f'(x) = \frac{U_2 A^*}{2\sqrt{x}} \quad (\text{Eqn. D.9})$$

As before, the shock shape comes from the boundary condition at the shock, and gives

$$x_{sh} = \frac{1}{U_1 - U_2} \int_0^r v(o, r) dr$$

(Eqn. D.10)

This completes the formulation of the problem.

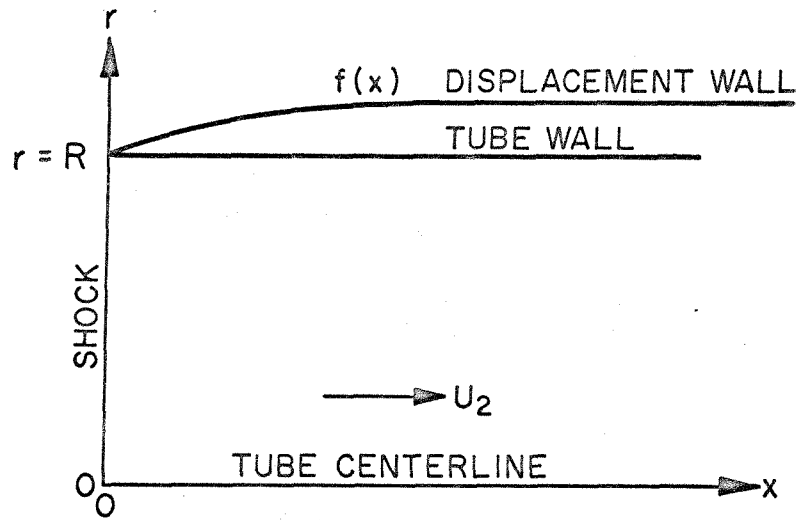


FIG. D.1
AXISYMMETRIC GEOMETRY

D.2 Solution of the Problem

The solution to equation D.5 is

$$F = AI_1(mpr) + BK_1(mpr) \quad (\text{Eqn. D.11})$$

and that to equation D.6 is

$$G = C' \cos px + D' \sin px \quad (\text{Eqn. D.12})$$

so that the general solution for the velocity v is

$$v(x,r) = \left. \begin{array}{l} I_1(mpr) \\ K_1(mpr) \end{array} \right\} \left. \begin{array}{l} \cos \\ \sin \end{array} \right\} px \quad (\text{Eqn. D.13})$$

The symmetry boundary condition yields $B = 0$ and if $v(x,r)$ is to be an even function of x , then $D' = 0$ also. Thus the above solution integrated for arbitrary wall shape reduces to

$$v(x,r) = \frac{2}{\pi} \int_0^{\infty} A_p I_1(mpr) \cos px \, dp \quad (\text{Eqn. D.14})$$

The wall shape is introduced into the Fourier integral relation to solve for the coefficients A_p as follows:

$$v(x,R) = \frac{2}{\pi} \int_0^{\infty} A_p I_1(mpr) \cos px \, dp \quad (\text{Eqn. D.15})$$

where

$$\begin{aligned}
 A_p I_1(m\rho R) &= \int_0^{\infty} v(x,R) \cos px \, dx \\
 &= \int_0^{\infty} \frac{U_2 A^*}{2\sqrt{x}} \cos px \, dx \\
 &= \frac{U_2 A^*}{2} \sqrt{\frac{\pi}{2p}}
 \end{aligned}
 \tag{Eqn. D.16}$$

Thus

$$A_p = \frac{U_2 A^*}{2 I_1(m\rho R)} \sqrt{\frac{\pi}{2p}}
 \tag{Eqn. D.17}$$

Substituting this back into equation D.14, one obtains the complete solution for the sink velocity:

$$v(x,r) = \frac{U_2 A^*}{\sqrt{2\pi}} \int_0^{\infty} \frac{I_1(mpr)}{I_1(m\rho R)} \frac{\cos px}{\sqrt{p}} \, dp
 \tag{Eqn. D.18}$$

which is also
(Eqn. 2.5)

Evaluating this at the plane $x = 0$,

$$v(0,r) = \frac{U_2 A^*}{\sqrt{2\pi}} \int_0^{\infty} \frac{I_1(mpr)}{I_1(m\rho R)} \frac{dp}{\sqrt{p}}
 \tag{Eqn. D.19}$$

one can then use equation D.10 to find the shock shape:

$$x_{sh}(r) = \frac{A^*U_2}{\sqrt{2\pi} (U_1-U_2)} \int_0^\infty \frac{\int_0^r I_1(m\rho r) dr}{I_1(m\rho R) \sqrt{\rho}} d\rho \quad (\text{Eqn. D.20})$$

$$= \frac{A^*U_2}{\sqrt{2\pi} (U_1-U_2)} \int_0^\infty \frac{\frac{1}{m\rho} [I_0(m\rho r) - I_0(0)]}{I_1(m\rho R) \sqrt{\rho}} d\rho \quad (\text{Eqn. D.21})$$

$$= \frac{A^*U_2}{\sqrt{2\pi} (U_1-U_2)m} \int_0^\infty \frac{I_0(m\rho r) - 1}{I_1(m\rho R) \rho^{3/2}} d\rho \quad (\text{Eqn. D.22})$$

Now if we introduce new variables $\eta = \frac{r}{R}$ and $t = m\rho R$, this reduces to

$$x_{sh}(r) = \frac{A^*U_2 \sqrt{R}}{\sqrt{2\pi m} (U_1-U_2)} \int_0^\infty \frac{I_0(t\eta) - 1}{I_1(t) t^{3/2}} dt \quad (\text{Eqn. D.23})$$

which is also
(Eqn. 2.6)

D.3 Evaluation of the Shape

The numerical evaluation of the integral in equation D.23 is carried out in appendix E for various values of η . Again defining θ as the axial extent, it turns out that the integral has the value 2.78 for $\eta = 1$ and thus

$$\theta \equiv x_{sh} \Big|_{\eta=1} = \frac{A^* U_2 \sqrt{R}}{\sqrt{2\pi m} (U_1 - U_2)} \quad [2.78] \quad (\text{Eqn. D.24})$$

which leads directly to equation 2.7.

The shock shape calculated in appendix E is shown in figures III.1, III.5, III.6, and IV.1 and is reproduced in figure D.2 in non-dimensional form. When plotted in this way the two-dimensional and axisymmetric shapes are nearly identical and differ little from a quarter circle.

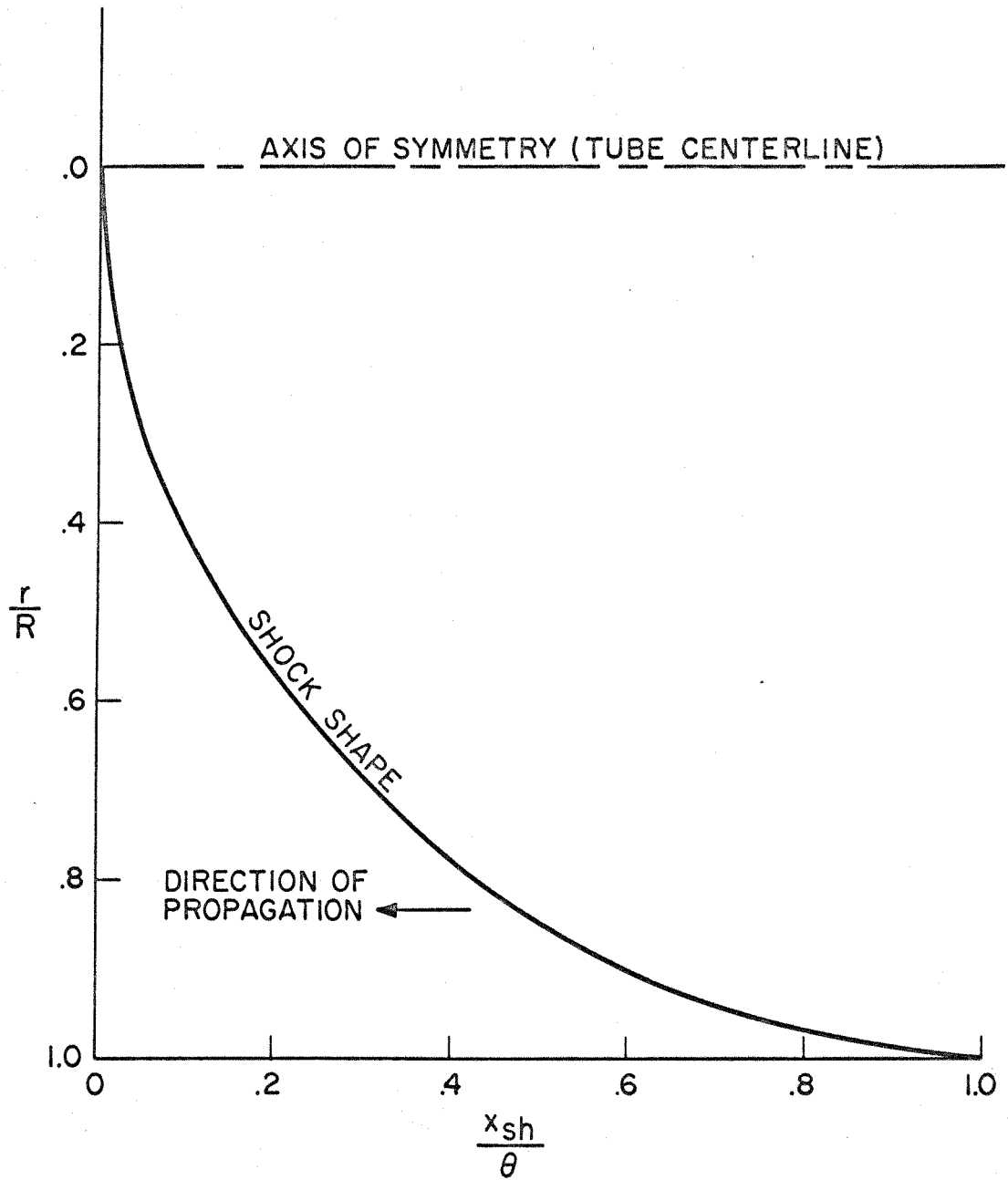


FIG. D.2
THEORETICAL SHOCK SHAPE
AXISYMMETRIC CASE

D.4 Central Radius of Curvature

The slope of the shock at any point is given by

$$\left. \frac{dx}{dr} \right|_{sh} = \frac{v(o,r)}{U_1 - U_2} \quad (\text{Eqn. D.25})$$

and is of course zero at $r = 0$. The curvature at the centerline of the tube, however, is finite and can be calculated by putting the expression for $v(o,r)$ from equation D.19 into the above, differentiating with respect to r and evaluating at $r = 0$. The result is of interest for such applications as optical reflectivity experiments such as those by Linzer & Hornig (Ref. 22) or for short path optical experiments near the center of a tube (electron beam or integrating Schlieren for example).

$$\left. \frac{d^2x}{dr^2} \right|_{sh} = \frac{U_2 A^*}{(U_1 - U_2) \sqrt{2\pi}} \int_0^{\infty} \frac{\frac{d}{dr} [I_1(mpr)] dp}{I_1(mpr) \sqrt{p}} \quad (\text{Eqn. D.26})$$

$$= \frac{U_2 A^*}{(U_1 - U_2) \sqrt{2\pi}} \int_0^{\infty} \frac{\frac{mp}{2} [I_0(mpr) + I_2(mpr)] dp}{I_1(mpr) \sqrt{p}}$$

$$= \frac{U_2 A^* m}{2\sqrt{2\pi} (U_1 - U_2)} \int_0^{\infty} \frac{\sqrt{p} [I_0(mpr) + I_2(mpr)] dp}{I_1(mpr)}$$

(Eqn. D.27)

Although this could be evaluated at any r , its evaluation at $r \neq 0$ is extremely difficult and, fortunately, of little practical use.

At the center of the tube, however,

$$\left. \frac{d^2x}{dr^2} \right|_{r=0}^{\text{sh}} = \frac{U_2 A^* m [I_0(0) + I_2(0)]}{2\sqrt{2\pi} (U_1 - U_2)} \int_0^\infty \frac{\sqrt{p} dp}{I_1(mpR)} \quad (\text{Eqn. D.28})$$

Now $I_0(0) = 1$ and $I_2(0) = 0$. If a new variable $t = mpR$ is introduced, the above reduces to

$$\left. \frac{d^2x}{dr^2} \right|_{r=0}^{\text{sh}} = \frac{U_2 A^*}{2\sqrt{2\pi m} (U_1 - U_2) R^{3/2}} \int_0^\infty \frac{\sqrt{t} dt}{I_1(t)} \quad \begin{array}{l} (\text{Eqn. D.29}) \\ \text{which is also} \\ (\text{Eqn. 2.8}) \end{array}$$

The integral in this expression has the value 6.38 (see section D.5)

and thus

$$\left. \frac{d^2x}{dr^2} \right|_{r=0}^{\text{sh}} = \frac{6.38 U_2 A^*}{2\sqrt{2\pi m} (U_1 - U_2) R^{3/2}} \quad (\text{Eqn. D.30})$$

Since the shock slope can be assumed everywhere small, the radius of curvature is approximately the reciprocal of the curvature (and at $r = 0$ it is exactly so), thus equation 2.9 follows immediately.

$$\frac{R}{R_0} = R \left. \frac{d^2x_{\text{sh}}}{dr^2} \right|_{r=0} = \frac{6.38 U_2 A^*}{2(2\pi m R)^{1/2} (U_1 - U_2)} \quad \begin{array}{l} (\text{Eqn. D.31}) \\ \text{which is also} \\ (\text{Eqn. 2.9}) \end{array}$$

D.5 Numerical Evaluation of P $\equiv \int_0^{\infty} \frac{\sqrt{t} dt}{I_1(t)}$

Let

$$P = \int_0^{\infty} \frac{\sqrt{t} dt}{I_1(t)} = \int_0^{.2} \frac{\sqrt{t} dt}{I_1(t)} + \int_{.2}^{11} \frac{\sqrt{t} dt}{I_1(t)} + \int_{11}^{\infty} \frac{\sqrt{t} dt}{I_1(t)} = P_1 + P_2 + P_3$$

(Eqn. D.32)

respectively. To calculate P_1 one can use the small argument expansion of the Bessel function:

$$I_1(t) = \sum_{r=0}^{\infty} \frac{\left(\frac{t}{2}\right)^{1+2r}}{r! \Gamma(r+2)} = \frac{t}{2} + \frac{t^3}{16} + \frac{t^5}{384} + \frac{t^7}{18432} + \frac{t^9}{1474560} + \dots$$

(Eqn. D.33)

Then

$$P_1 = \int_0^{.2} \frac{\sqrt{t} dt}{t/2} = 2 \int_0^{.2} t^{-1/2} dt = 2 \left. \frac{t^{1/2}}{1/2} \right|_0^{.2}$$

$P_1 = 1.78885$

(Eqn. D.34)

To calculate P_3 , on the other hand, one uses the large argument expansion of the Bessel function:

$$I_1(t) = \frac{e^t}{\sqrt{2\pi t}} \left[1 - \frac{3}{8t} + \frac{3(-5)}{2(8t)^2} - \dots \right] \quad (\text{Eqn. D.35})$$

and

$$\begin{aligned}
 P_3 &= \int_{11}^{\infty} \frac{\sqrt{2\pi t} \sqrt{t} dt}{e^{-t} \left[1 - \frac{3}{8t} - \frac{15}{128t^2} - \dots\right]} & (\text{Eqn. D.36}) \\
 &\approx \sqrt{2\pi} \int_{11}^{\infty} \frac{t \left[1 + \frac{3}{8t}\right] dt}{e^{-t}} \\
 &= \sqrt{2\pi} \int_{11}^{\infty} t e^{-t} dt + \frac{3\sqrt{2\pi}}{8} \int_{11}^{\infty} e^{-t} dt
 \end{aligned}$$

$$P_3 = .000518$$

(Eqn. D.37)

P_2 was evaluated by numerical integration using Gregory's formula (page 157, Ref. 29, for example) carried to the second difference. Intervals of .1 were used from .2 to 2.5, of .5 from 2.5 to 6.0 and of 1 from 6 to 11. The values of the Bessel functions were obtained from pages 218 and 221 of reference 30. The result was

$$P_2 = 4.59036066$$

(Eqn. D.38)

Thus the entire integral has the value

$$P = P_1 + P_2 + P_3 = 6.37973$$

(Eqn. D.39)

APPENDIX E: NUMERICAL EVALUATION OF

$$Q \equiv \int_0^{\infty} \frac{I_0(\tau\eta) - 1}{I_1(\tau) \tau^{3/2}} dt$$

E.1 Expansion for Small τ

Just as with the integral P in section D.5, because of the non-availability of expansions for the Bessel functions uniformly valid for all size arguments, it is necessary to break the integral Q into three integrals. Expansions are available for both small and large arguments, and the intermediate argument integral can be evaluated numerically.

$$Q = \int_0^{\infty} \frac{I_0(\tau\eta) - 1}{I_1(\tau) \tau^{3/2}} dt = \int_0^{.1} (\) dt + \int_{.1}^{11} (\) dt + \int_{11}^{\infty} (\) dt = Q_1 + Q_2 + Q_3$$

(Eqn. E.1)

respectively.

For small arguments,

$$I_1(\tau) = \frac{\tau}{2} + \frac{\tau^3}{16} + \frac{\tau^5}{384} + \dots$$

(Eqn. E.)

and

$$I_0(\tau\eta) = 1 + \frac{(\tau\eta)^2}{4} + \frac{(\tau\eta)^4}{64} + \frac{(\tau\eta)^6}{2304} + \dots$$

(Eqn. E.)

Then

$$Q_1 = \int_0^{.1} \frac{I_0(t\eta) - 1}{I_1(t) t^{3/2}} dt \quad (\text{Eqn. E.4})$$

$$\approx \int_0^{.1} \frac{\frac{(t\eta)^2}{4} + \frac{(t\eta)^4}{64} + \frac{(t\eta)^6}{2304}}{\left[\frac{t}{2} + \frac{t^3}{16} + \frac{t^5}{384}\right] t^{3/2}} dt \quad (\text{Eqn. E.5})$$

$$\approx \int_0^{.1} \left[\frac{\eta^2}{2} t^{-1/2} + \frac{\eta^4}{32} t^{3/2} + \frac{\eta^6}{1152} t^{7/2} \right] \left[1 - \frac{t^2}{8} - \frac{t^4}{192} \right] dt$$

$$\approx \int_0^{.1} \left[\frac{\eta^2}{2} t^{-1/2} - \left(\frac{\eta^2}{16} - \frac{\eta^4}{32} \right) t^{3/2} - \left(\frac{\eta^2}{384} + \frac{\eta^4}{256} - \frac{\eta^6}{1152} \right) t^{7/2} - \dots \right] dt$$

$$= .31614872 \eta^2 + .00003950 \eta^4 + .00000000610 \eta^6 + \dots$$

$Q_1 \approx .31614872 \eta^2 + .00003950 \eta^4$

(Eqn. E.6)

E.2 Computation of Q_2

In this intermediate range where neither of the Bessel function expansions is valid it is necessary to numerically integrate by brute force at each value of η .

This was accomplished first at $\eta = .2, .5, .8,$ and 1.0 by hand calculation using Gregory's formula carried to the second difference. As in the computation of P , intervals of $.1$ from $.1$ to 2.5 , of $.5$ from 2.5 to 6.0 , and of 1.0 from $t = 6.0$ to 11.0 were used.

Subsequently, with the assistance of Dr. M. Chahine of the Jet Propulsion Laboratory, Q_2 was evaluated at $\eta = .1, .2, \dots, 1.0$ using machine computation and much smaller intervals of t . The computer results showed the hand calculations to have overestimated the value of Q_2 by typically $.1\%$.

The computer values for Q_2 are included in figure E.2 at the end of the appendix.

E.3 Expansion for Large $t\eta$

Since Q_3 has been defined such that $t > 10$ and the large-argument expansion is good for values of $t\eta \geq 2$ the results of this section can only be applied for calculating Q at $\eta \geq .2$. Since the value of $Q(0)$ is known to be zero and the first and second derivatives of the shock shape are also known at $\eta = 0$, the inability to calculate Q_3 for $0 < \eta < .2$ by this procedure does not noticeably hamper our ability to construct the shock shape. Moreover we can show that Q_3 in this range is of the order of 10^{-7} and thus does not prevent determination of Q for $0 < \eta < .2$ to several figure accuracy.

For large arguments (see page 143, Ref. 31, for example),

$$I_1(t) = \frac{e^t}{\sqrt{2\pi t}} \left[1 - \frac{3}{8t} - \frac{15}{128t^2} - \dots \right] \quad (\text{Eqn. E.7})$$

and

$$I_0(t\eta) = \frac{e^{t\eta}}{\sqrt{2\pi t\eta}} \left[1 - \frac{-1}{8t\eta} + \frac{(-1)(-9)}{2(8t\eta)^2} - \dots \right] \quad (\text{Eqn. E.8})$$

Then

$$Q_3 = \int_{11}^{\infty} \frac{I_0(t\eta) - 1}{I_1(t) t^{3/2}} dt \quad (\text{Eqn. E.9})$$

$$Q_3 = \int_{11}^{\infty} \frac{\frac{e^{t\eta}}{\sqrt{2\pi t\eta}} \left[1 + \frac{1}{8t\eta} + \frac{9}{128t^2\eta^2} \right] - 1}{\frac{te^t}{\sqrt{2\pi}} \left[1 - \frac{3}{8t} - \frac{15}{128t^2} \right]} dt \quad (\text{Eqn. E.10})$$

$$Q_3 \approx \int_{11}^{\infty} \frac{e^{t\eta-t}}{\sqrt{\eta}} t^{-3/2} \left[1 + \frac{1}{8\eta t} + \frac{9}{128t^2\eta^2} \right] \left[1 + \frac{3}{8t} + \frac{15}{128t^2} \right] dt -$$

$$\int_{11}^{\infty} \frac{\sqrt{2\pi} e^{-t}}{t} \left[1 + \frac{3}{8t} + \frac{15}{128t^2} \right] dt \quad (\text{Eqn. E.11})$$

$$Q_3 = Q_{3a} + Q_{3b} \quad (\text{Eqn. E.12})$$

where Q_{3b} is not a function of η and thus can be evaluated numerically.

$$Q_{3b} = -\sqrt{2\pi} \int_{11}^{\infty} [e^{-t}t^{-1} + \frac{3}{8} e^{-t}t^{-2} + \frac{15}{128} e^{-t}t^{-3}] dt \quad (\text{Eqn. E.13})$$

$$= -\sqrt{2\pi} \left\{ -\text{Ei}(-11) + \frac{3}{8} \left[\frac{e^{-11}}{11} + \text{Ei}(-11) \right] + \right.$$

$$\left. \frac{15}{128} \left[e^{-11} \left(-\frac{1}{22} + \frac{1}{242} \right) - \frac{1}{2} \text{Ei}(-11) \right] \right\} \quad (\text{Eqn. E.14})$$

$$Q_{3b} = 1.71351542 \text{Ei}(-11) - 1.2244979 \times 10^{-6} \quad (\text{Eqn. E.15})$$

where (see page 116, Ref. 32)

$$\text{Ei}(-11) \approx -e^{-11} \left(\frac{1}{11} - \frac{1}{11^2} + \frac{2}{11^3} - \frac{6}{11^4} + \frac{24}{11^5} - \frac{120}{11^6} + \dots \right)$$

$$= -1.4003 \times 10^{-6} \quad (\text{Eqn. E.16})$$

Thus

$$Q_{3_b} = - 3.6239 \times 10^{-6} \quad (\text{Eqn. E.17})$$

Now Q_{3_a} is a function of η and thus must be evaluated at each η individually.

$$Q_{3_a} = \frac{1}{\sqrt{\eta}} \int_{11}^{\infty} \left\{ t^{-3/2} e^{-t(1-\eta)} + \frac{1}{8} \frac{1}{\eta} + 3 t^{-5/2} e^{-t(1-\eta)} + \right. \\ \left. \frac{3}{64} \frac{3}{2\eta^2} + \frac{1}{\eta} + \frac{5}{2} t^{-7/2} e^{-t(1-\eta)} + \frac{3}{1024\eta} \frac{9}{\eta} + 5 t^{-9/2} e^{-t(1-\eta)} + \right. \\ \left. \frac{135}{16384\eta^2} t^{-11/2} e^{-t(1-\eta)} \right\} dt \quad (\text{Eqn. E.18})$$

The integration of equation E.18 at each value of η involves the use of the following relation (see page 331, Ref. 28):

$$\int_{11}^{\infty} t^{\nu-1} e^{-\mu t} dt = \mu^{-\nu} \Gamma(\nu, \mu u) \quad (\text{Eqn. E.19})$$

where (see page 954, Ref. 28):

$$\Gamma(\nu, \mu u) \equiv \int_{\mu u}^{\infty} e^{-t} t^{\nu-1} dt \quad (\text{Eqn. E.20})$$

and in turn is evaluated according to

$$\Gamma(v, \mu u) = \Gamma(v) - \sum_{n=0}^{\infty} \frac{(-1)^n (\mu u)^{v+n}}{n! (v+n)} \quad (\text{Eqn. E.21})$$

where $v \neq 0, -1, -2, \dots$

Now for use in integrating equation E.18, the parameters introduced in equation E.19 have the following values:

$$\mu = 1 - \eta$$

$$\mu u = 11(1-\eta) \quad (\text{Eqn. E.22})$$

$$v = -\frac{1}{2}, -\frac{3}{2}, -\frac{5}{2}, -\frac{7}{2}, -\frac{9}{2}$$

each term in equation E.18 having a different value of v .

It is also necessary to use the relation (see page 260, Ref. 33)

$$\Gamma(n+1) = n\Gamma(n) \quad (\text{Eqn. E.23})$$

and (see page 117, Ref. 32)

$$\Gamma(-x) = -\frac{\pi}{\Gamma(x+1) \sin \pi x} \quad (\text{Eqn. E.24})$$

When all these relations are combined it is possible to derive a general expression for Q_{3a} in which the infinite series are in suitable form for evaluation by digital computer. This equation is given in figure E.1.

The infinite series in this equation are

$$\sum_{n=1}^{\infty} (-1)^n \frac{2}{2n+1} \frac{(11\mu)^n}{(n+j)!} \equiv \sum_{n=1}^{\infty} T_n \quad (\text{Eqn. E.25})$$

where j takes on the values 1, 2, 3, and 4. The ratio R_n of two successive terms is always of order one and thus the computer can easily generate each succeeding term from the one preceding it by the recursion formula

$$R_n \equiv \frac{T_n}{T_{n-1}} = -1 \frac{2n-1}{2n+1} \frac{11\mu}{n+j} \quad (\text{Eqn. E.26})$$

At the larger values of μ up to 33 terms were required to obtain the desired accuracy.

The calculations were performed for $\eta = .2, .3, .4, \dots, .9$ ($\mu = .8, .7, .6, \dots, .1$) and the results substituted in the general equation for Q_{3a} (Fig. E.1). The resulting values for Q_{3a} were added to Q_{3b} to obtain Q_3 which is tabulated in figure E.2.

Note that $\frac{x_{sh}}{\theta} (\eta=.8) = .432$ has been used in plotting the theoretical values of $\Delta x(.8)$ in several figures in the body of the report (figures III.4, IV.2, V.1, and IX.2).

$$\begin{aligned}
 Q_{3a} = & \sqrt{\frac{\mu}{n}} \left\{ -2\sqrt{\pi} + \sqrt{11\mu} \left[\frac{.18181818}{\mu} + 2 + \sum_{n=1}^{\infty} (-1)^n \left(\frac{2}{2n+1} \right) \frac{(11\mu)^n}{(n+1)!} \right] \right\} + \\
 & \frac{1}{8} \left(\frac{1}{n} + 3 \right) \mu^{3/2} \left\{ \frac{4\sqrt{\pi}}{3} - \sqrt{11\mu} \left[\frac{.005509642}{\mu^2} + \frac{.18181818}{\mu} + 1 + \sum_{n=1}^{\infty} (-1)^n \left(\frac{2}{2n+1} \right) \frac{(11\mu)^n}{(n+2)!} \right] \right\} + \\
 & \frac{3}{64} \left(\frac{3}{2n^2} + \frac{1}{n} + \frac{5}{2} \right) \mu^{5/2} \left\{ \frac{-8\sqrt{\pi}}{15} + \sqrt{11\mu} \left[\frac{.0003005259}{\mu^3} - \frac{.005509642}{\mu^2} + \frac{.09090909}{\mu} \right. \right. \\
 & \quad \left. \left. + .3333333 + \sum_{n=1}^{\infty} (-1)^n \left(\frac{2}{2n+1} \right) \frac{(11\mu)^n}{(n+3)!} \right] \right\} + \\
 & \frac{3}{1024n} \left(\frac{9}{n} + 5 \right) \mu^{7/2} \left\{ \frac{16\sqrt{\pi}}{105} - \sqrt{11\mu} \left[-\frac{.00001951467}{\mu^4} + \frac{.0003005259}{\mu^3} - \frac{.002754821}{\mu^2} + \right. \right. \\
 & \quad \left. \left. \frac{.0303030303}{\mu} + \frac{1}{12} + \sum_{n=1}^{\infty} (-1)^n \left(\frac{2}{2n+1} \right) \frac{(11\mu)^n}{(n+4)!} \right] \right\}
 \end{aligned}$$

FIG. E.1 GENERAL EQUATION FOR Q_{3a}

η	Q_1	Q_2	Q_3	Q	$\frac{x_{sh}}{\theta} = \frac{Q(\eta)}{Q(1)}$
0	.000000000	.000000000	.000000000	.000000000	.000000000
.1	.003161491	.01280639	(0)10 ⁻⁷	.015968	.00574357
.2	.012646011	.05157252	.000007784	.06422632	.02310172
.3	.028453703	.11739007	.000040108	.14588388	.05247333
.4	.050584806	.21227657	.000081239	.26294262	.09457848
.5	.079039648	.33954832	.000261498	.41884947	.15065699
.6	.113818658	.50453609	.000866893	.61922164	.22272936
.7	.154922355	.71597695	.003021586	.87392089	.31434276
.8	.202351359	.98881041	.011393820	1.20255559	.43255018
.9	.256106378	1.35004154	.050108781	1.65625670	.59574305
1.0	.31618822	1.85157275	.6123918	2.78015277	1.00000000

FIG. E.2 RESULTS OF NUMERICAL EVALUATION OF Q
 $\left(\frac{x_{sh}}{\theta}\right)$ vs. η plotted in Fig. D.2)

APPENDIX F: DISCUSSION OF ACCURACY

F.1 General Considerations

Possible sources of errors may be conveniently broken down into two categories:

- (1) signal errors, where the time difference between the signals put out by the gages does not accurately reflect the shock shape, and
- (2) post-signal errors, where the time differences are not accurately recorded or read.

Possible causes of signal errors are:

- (1) the gages not being located such that their surfaces lie in a plane normal to the end wall, due either to bowing of the end wall or protrusion of the gage from the wall.
- (2) radial variation of local shock speed.
- (3) variations of gage rise-times.

Possible causes of post-signal errors are:

- (1) lack of synchronization of scope sweeps.
- (2) variation of scope sweep speeds.
- (3) variation in length of BNC cables from gages to scopes.
- (4) variation of scope rise-times.
- (5) optical distortion of oscilloscope grid and trace.
- (6) variation in picture scribing technique.
- (7) errors in reading scribed pictures.

F.2 Discussion of Signal Errors

The gages were mounted flush with the inside surface of a 3/4" stainless steel end plate. The plate surface was machined flat, polished, and checked with an optical flat. Even with the instrumentation holes, the rigidity of the plate was sufficient to prevent detectable strain when subjected to the pressure difference caused by evacuation of the test section.

Whenever gage protrusion occurred it was measured and the data corrected accordingly.

When shock shape oscillations are occurring, there must be radial variations in the local shock speed. These variations depend on the amplitude of the shock perturbation and their effect, in turn, on the determination of the shock shape is a higher order quantity which can be ignored when ξ/R is small.

The response characteristics of the film gages were very uniform. Their rise-time was small compared with the shock reflection time at initial pressures below 10 mm Hg.

It is felt that the total possible shock shape error due to these causes could be no more than a few hundredths of a millimeter, this being due mainly to gage protrusion.

This could be checked if one had access to a perfectly plane shock. Indeed the apparent shock perturbations do uniformly approach zero as $L/p_1 R^2$ approaches infinity.

F.3 Discussion of Post-Signal Errors

All the individual possible causes for errors of this type were carefully considered and eliminated as far as possible. All oscilloscopes were triggered from a single source. Sweep speeds were periodically checked. All scopes were Tektronix type 555 with type L amplifiers, operating on the same sweep speed. It was found that under these conditions timing errors were on the order of 2 to 5 nanoseconds, whereas if different scopes were employed or even different sweep speeds on identical scopes, the timing errors could be ten times as great.

Fortunately a simple means for checking on all the post-signal errors at once exists. The equipment is set up just as in an actual shock shape experiment and a signal is applied to all the gages at once, simulating a perfectly plane shock with zero signal error. Oscilloscope pictures are taken, scribed, and read and a "shape" for this electronic shock wave determined. This procedure was accomplished periodically and errors were of the order of a few hundredths of a millimeter. An abbreviated form of this procedure, wherein the scope synchronization and sweep could be checked, was performed before and after each day's experiments.

Considering both signal and post-signal errors, the data seem to be reliable easily to a tenth of a millimeter.

F.4 Sample Adjusted Shock Shape Determination

Figure F.1 contains the oscilloscope pictures for the eight data points for run 1401. This run was a part of the axisymmetric rooftop disturbance experiment and yielded the point $\xi/R = -.111$ at $\zeta/R = 2.51$ on figure VII.1. It can be seen that the data is carried to the nearest hundredth of a millimeter, which leads to four decimal places in ξ/R . This is then rounded off to three places, all of which can be considered significant. Note that two decimal places would have been sufficient for use in plotting figure VII.1.

Figure F.2 is a true scale plot of the shock shape determined by the data of run 1401. By comparing figures F.1 and F.2 one can see how the shock shape can be visualized qualitatively even before reducing the data.

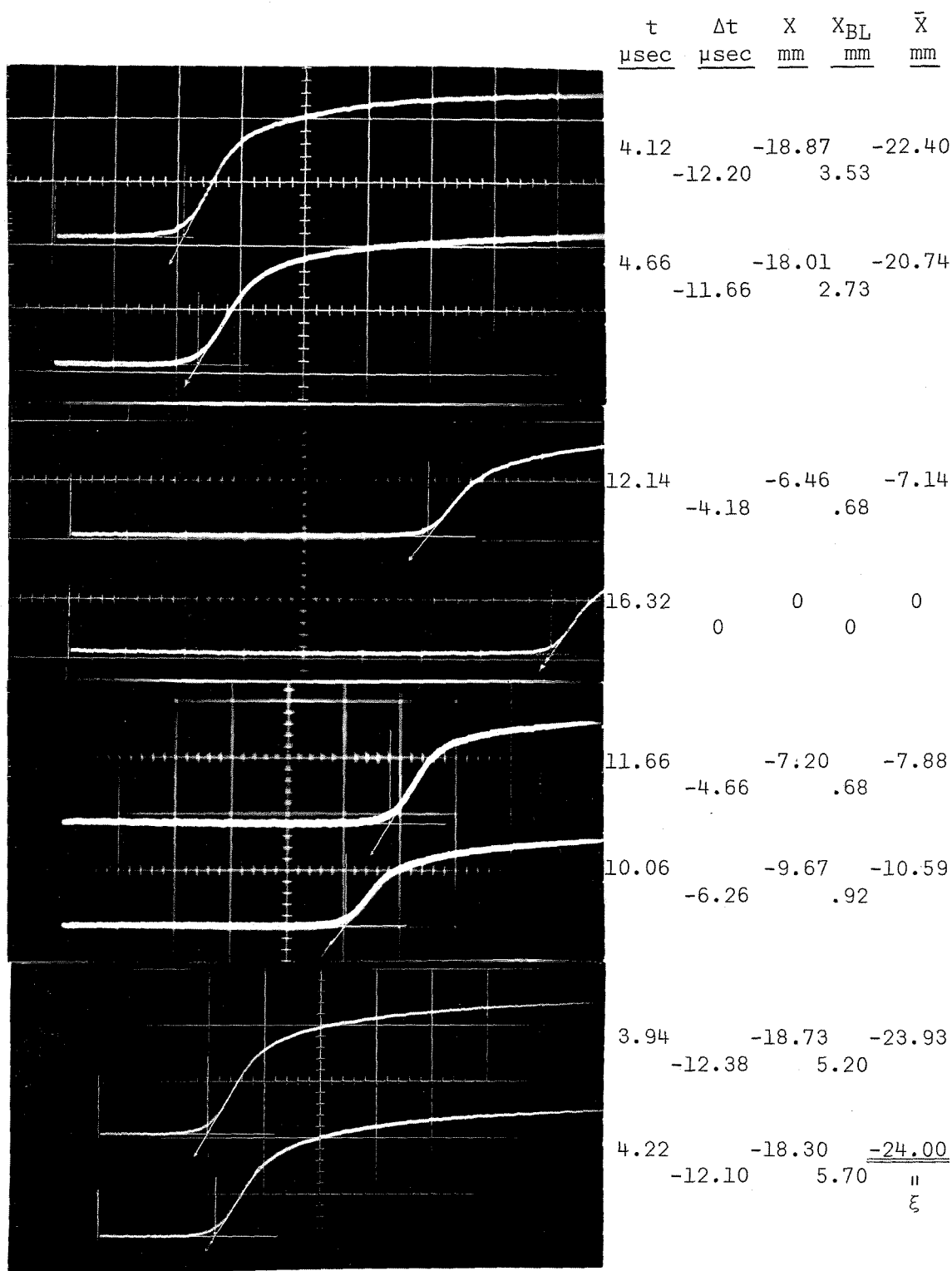


FIG. F.1 DATA FROM RUN 1401

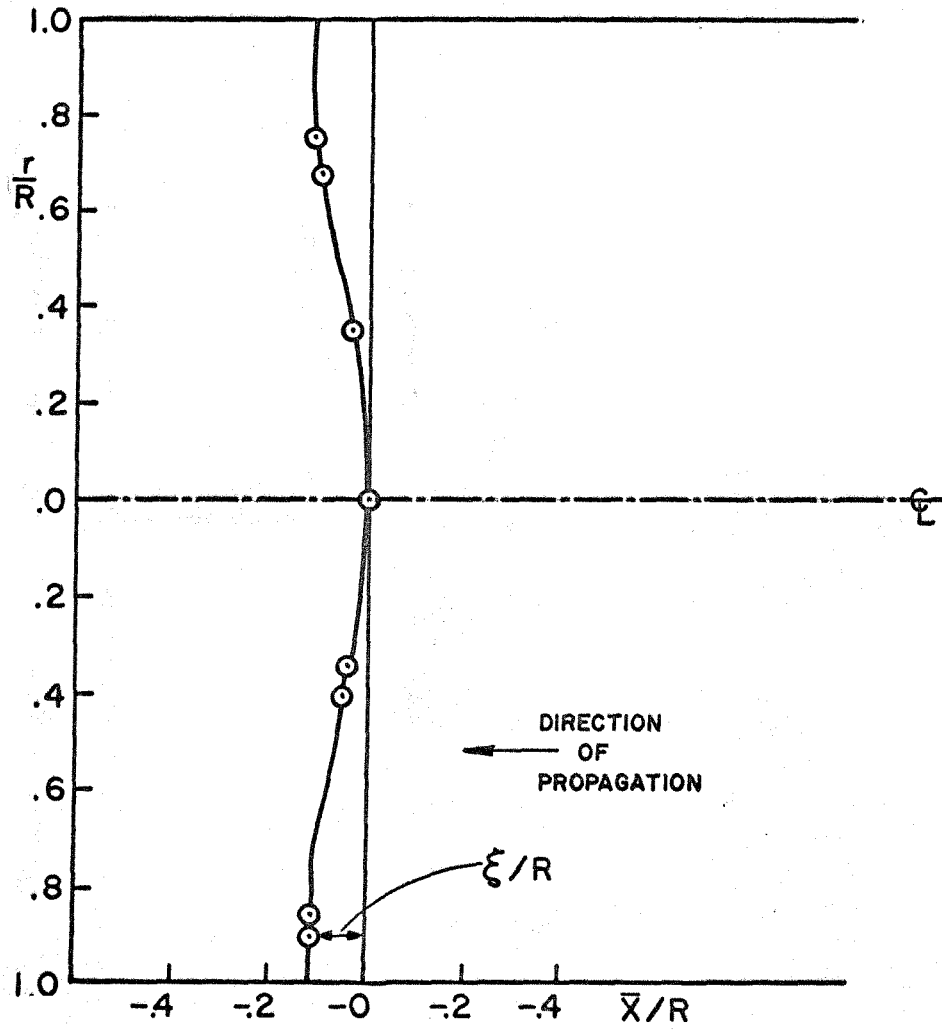


FIG. F. 2
TRUE SCALE ADJUSTED SHOCK SHAPE
RUN 1401